AN IC DESIGN FOR WIRELESS BATTERYLESS MULTI-SENSING PLATFORM FOR BIOMEDICAL APPLICATIONS

by

YOUNG-SIK SEO

Presented to the Faculty of the Graduate School of

The University of Texas at Arlington in Partial Fulfillment

of the Requirements

for the Degree of

DOCTOR OF PHILOSOPHY

THE UNIVERSITY OF TEXAS AT ARLINGTON

May 2012

ProQuest LLC.
789 East Eisenhower Parkway
P.O. Box 1346
Ann Arbor, MI 48106 - 1346

ACKNOWLEDGEMENTS

My true appreciation goes to Professor Dr. J.-C. Chiao who has motivated and supervised my research work. It is an honor for me to work with him throughout my degree period. Without his brilliant ideas of how my VLSI skill could be utilized in biomedical field, my academic career would have been harder. I have really enjoyed being an iMEMS member. I have enjoyed sharing ideas and words with the members. All the members are my great friends, tutors, and mentors.

My thanks also go to Dr Gu, one of the most generous persons I have ever met. He has always been an excellent helper for any questions I asked him. His suggestions were simple, smart and very effective. Another great help was from Dr. Butler. Having a MOSIS account and all materials I need could not have been done without his effort and support.

I would like to thank to Dr. Carter, Dr. Davis, Dr Zhou and Dr. Dillon. The issues and suggestions they pointed out were very sharp and clever. With their help, I have been able to improve my research quality. Thank you all for gladly joining the committees.

Finally, I would like to express my appreciation to my families. My parents who I respect more than anybody else in the world always have given me endless love. My lovely wife, Lek, and my cute son, Bryce (He always wants to be called “big boy”. At the age he can understand this dissertation, he will have been a real big boy. I am telling him of future. Yes, you are a big boy). I am here because of my family, and I will be there because of my family. I love ya’all.

April 12, 2012

ABSTRACT

AN IC DESIGN FOR WIRELESS BATTERYLESS MULTI-SENSING PLATFORM FOR BIOMEDICAL APPLICATIONS

Young-Sik Seo, PhD

The University of Texas at Arlington, 2012

Supervising Professor: Jung-Chih Chiao

This work proposed an integrated circuit (IC) design that provides the required functionality for a wireless, batteryless implant. For biomedical applications, the physiological signals can be detected if the parameter of interest can be converted to a change in electrical parameters such as capacitance, resistance or an amperometric signal. The implantable transponder is suitable for sensors that generate one of the aforementioned analog signals. In the proposed universal platform, a voltage-controlled oscillator (VCO) was used to detect variations of voltage or current. Similarly, a relaxation oscillator (RO) was used to detect changes in capacitance or resistance. Thus, the VCO and the RO were integrated in a single chip, thereby providing the capability to transduce all of the possible analog signals into frequencies. To minimize mutual interferences that can occur when multiple sensors are in operation, a multiplexer (MUX) was employed to isolate the operation of the oscillators. The MUX was switched by a local clock (CLK) to alternate the power between the two oscillators. As a result, at any given time, only one of the oscillators was in operation. The outputs of the oscillators were fed to the demultiplexer (DEMUX) sequentially to modulate the signals into a single signal. The C5N (0.5-μm) technology by On Semiconductor was used to design the

proposed platform. The chip was fabricated through MOSIS. The dimension of the die was 1.95 × 1.95 mm^2. The design also took into account all considerations for electrostatic discharge (ESD) protection of the chips. Benchtop tests were performed to measure the performance of the fabricated chip. The modulated signals from both the VCO and the RO were measured successfully without any overlap.

The miniaturization of implantable devices is limited by the size of the battery. Thus, for further reduction of size, a batteryless and wireless operation for the implant has been proposed. Inductive coupling and load modulation methods have been proposed to achieve wireless power transfer and wireless communications respectively. The batteryless solution was implemented by wireless power transfer at a carrier frequency of 1.3 MHz. This frequency was carefully chosen for its relatively high power transfer and low attenuation in tissues. The wireless communication was achieved via load modulation using a switched MOSFET in the implant circuitry. The wireless reader was composed of an envelope detector and frequency counter to demodulate the received signals from the implant. Furthermore, antenna optimization was investigated. Various size and number of coil turns in reader antennas were used to obtain power transfer and efficiency while the size of the implant antenna was fixed. The changes in power transfer and efficiency was also measured for various antenna separations between the two antennas. Antennas of 5-cm radius were determined as optimum in terms of power transfer, efficiency, current consumption, and size. Among the 5-cm antennas, the 17- and 18-turns of coil yielded relatively higher power transfer and efficiencies than other turns of coil did. The misalignment of the reader and the implant antenna due to motion artifacts was considered for practical biomedical applications. The changes in power transfer and efficiency due to mis-alignments were measured by changing the position of the the implant antenna around the reader antenna. Divergence, intensity, and 3 dB (half power) of transferred power and efficiency were also obtained and analyzed.

Using the fabricated chip and the optimum reader antenna, a wireless implantable device was fabricated on a printed circuit board (PCB). A 2-stage charge pump and an implant antenna (1 × 1.7 cm^2) were integrated on the PCB with the chip. Wireless communication was successfully tested by analyzing the signals obtained by the reader. The two oscillators were operated with capacitive, resistance, and voltage inputs. To demonstrate the feasibility of the wireless, batteryless multi-sensing platform, the implantable device on PCB was integrated with an impedance sensor, and a pH sensor. The aforementioned dual sensor platform has applications in GERD detection. The impedance and pH sensors were connected as input sources to the relaxation oscillator and VCO, respectively. The universal platform was able to deliver distinguishable signals from the two oscillators when various fluids of different pH levels were brought into contact with the sensors. The frequency ranges and the operating conditions closely matched the design considerations. Thus, the wireless batteryless implant using the IC-based multi-sensing platform for biomedical applications has been successfully demonstrated.

TABLE OF CONTENTS

LIST OF ILLUSTRATIONS

Figure Page

LIST OF TABLES

Table Page

CHAPTER 1

INTRODUCTION

1.1 Need for Multi-Sensing Platform for Implants

A single-channel sensing system is composed of a sensor and sensing circuitry. The sensor transduces the input signal into an analog output signal. The output signal can take the form of one of four electrical parameters i.e., voltage, current, capacitance, or resistance. The transduced signal may then be fed into the sensing circuitry, amplified, and converted to another parameter. In general, transduction of one type of signal requires one dedicated sensing circuitry. In case of multiple signals, additional circuitry to pre-convert the transduced signal to a proper analog parameter will be required. These systems will require more space and power consumption than single sensing systems do due to the additional components in the circuitry [1].

For biomedical applications, additional challenges are posed by the need for miniaturized implantable sensing systems. Thus, the key motivating factor for this work stems from the need for a multi-sensing system platform that can be operated with multi-type of sensors that will be beneficial to patients

1.2 Integrated Circuit Design for Sensing Circuitry

The sensing circuitry interfaces with multi-type sensors and converts their signals. The variations in the transduced signals should correspond with the parameters being sensed. If there is a lack of the correspondence between inputs and outputs, or minimal correspondence, the outputs will be hard to interpret. For example, if the variation is too small, it leads to very low resolution between neighboring values. The sensing circuitry therefore has to be designed taking into account the limitations of the entire system. To satisfy all the required functions such as transduction, amplification, and conversion of the signals, multiple discrete components may

have to be assembled, resulting in a larger size device [2]. Using market-available components on a printed circuit board (PCB) limits its use for implantable applications. An application-specific integrated circuit (ASIC) allows integration of several components on a single wafer. It is a single-chip technology and suits desired requirements. This work proposes the use of an ASIC to implement the circuitry. The proposed universal platform has been fabricated using 0.5-μm standard CMOS technology by On Semiconductor. The fabrication service has been through MOSIS.

1.3 Batteryless and Wireless Operation

The IC design significantly reduces the size of the system. However, another serious obstacle is the battery [3]. A battery limits an operation time for an implant. In addition, a battery significantly increases the size of the system. Often times, surgery is required to replace the battery of an implanted device [4, 5]. The current progress in the formulations of batteries has led to smaller sizes. However, the small size batteries do not meet the power requirements and lifetimes demanded by implantable devices. Thus, to reduce the size of an implantable device, a batteryless system and hence an energy harvesting method are required. Among the different energy harvesting methods available [6-9], inductive coupling requires low frequencies (from a few hundreds of kHz to 13.56 MHz) [10, 11] and can penetrate the human body better than higher frequencies can due to lower tissue attenuation [12] . Another benefit of using inductive coupling is that it delivers more power. The transmitting power can be adjusted as needed on the order of watts. For biomedical applications, the power requirement is of the order of milliwatts to prevent damage to the tissues [13]. To reduce tissue heating and damage from electromagnetic radiation, low power should be injected from the external reader. However, the power delivered to the implant may not be sufficient. Also, the distance from outside the body to a particular organ differs from person to person. The power delivered from a reader antenna to the implant antenna depends on the position and efficiency of coupling between the two antennas. In addition, mis-alignments causing power loss may be introduced between the two

antennas due to motion artifacts. Hence, a detailed study to increase power transfer and efficiency was carried out (Chapter 6).

Wireless communications deliver the data back to the reader. This work proposes using the same antennas for power transfer and communications. A load modulation method has been used to achieve the wireless communications. Further size reduction for the implant was accomplished using both the inductive coupling and load modulation methods

1.4 Feasibility Test with GERD

Gastro Esophageal Reflux Disease (GERD) is characterized by frequent heartburn (at least twice a week) [14]. It can cause erosive esophagitis that damages the delicate lining of the esophagus [15-18]. It can lead to Barrett's esophagus or even cancer. An estimated 10% of Americans suffer from GERD. Currently, Bravo™ from Medtronics (Figure 1.1) is the only available wireless GERD detector.

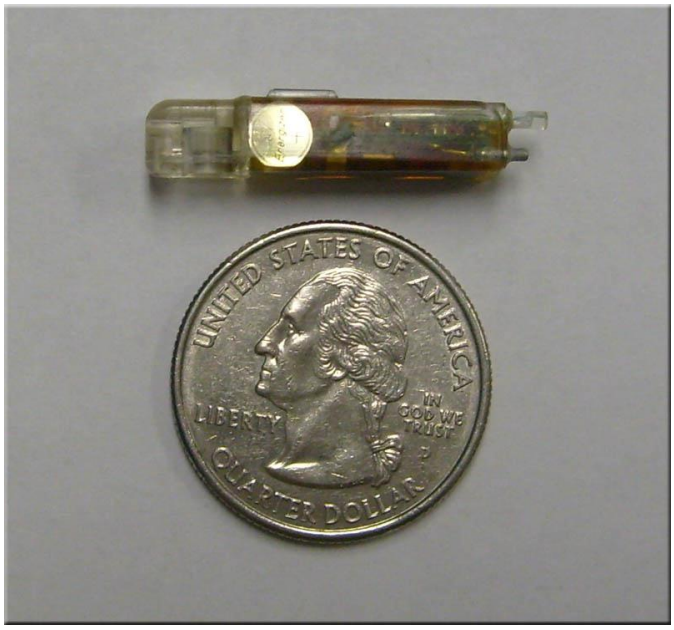

Figure 1.1 The Bravo from Medtronics. It is a battery operated pH level detector for GERD. The battery lasts upto 48 hours. This is the only wireless pH detection device available in the market.

This standalone device can perform pH level detection and wireless data transfer. However, a battery that lasts up to 48 hours operates the module. Additionally, Bravo cannot distinguish between consecutive episodes of reflux having the same pH levevl. In this case, the data that the reader obtains from the device will be the same for all events. Multiple events are considered as a single event due to the episodes being at the same analog level leading to inaccurate measurements.

In order to improve the sensing capability and to detect all reflux episodes, iMEMS research group from University of Texas at Arlington has designed wireless and batteryless pH level detectors for GERD application. The 2nd generation GERD detector (2nd from the top in Figure 1.2) is comparable in size with the Bravo [19]. It is batteryless with only a pH sensor. The 3rd generation sensor (third from the top) was equipped with two sensors; impedance and pH [20]. The pH sensor detects pH level of reflux while the impedance sensor measures the number of reflux episodes. This dual sensor system has been shown to perform well and be reliable in *in vivo* tests in animals. However, the size of the device has increased due to the additional discrete components required to implement the dual channels. The proposed IC-based dual system can be integrated with the two sensors and used for GERD detection. The size and power consumption will be significantly reduced.

Figure 1.2 The 2nd generation of the GERD sensor that is a single sensor detector (second from the top) is in a very compatible size with the Bravo (Top), The 3rd generation (second from the bottom) equipped with the two sensors. Both are batteryless operated.

CHAPTER 2

SYSTEM OVERVIEW

2.1 IC Design Tools

The, cost effective, C5N process has been chosen for the project fabrication. This 0.5-µm technology is provided by On Semiconductor (formerly known as AMI Semiconductor). Followings are some descriptions of the process [21].

- Non-Silicided CMOS process
- Three metal layers, two poly layers, and a high resistance layer
- Five volt applications
- PiP (poly2 to poly) capacitors (950 aF/µm2) available

For sensing purposes, dual physical sensors will be attached. For wireless battery solution, an inductive coil antenna will be wrapped around the system PCB. In addition some passive components will be used along with the chip. All of those that will be externally attached to the chip take the majority of the space in the complete system module. After all components are included in the package, a millimeter that might be saved in the chip dimension by using a new technology is not a critical issue.

The design package was chosen NCSU TechLib (AMI06). The schematic design, layout, and simulations were done by Cadence using Spectre and Virtuoso for the stimulator and layout design tool respectively.

2.2 Block Diagram of the Transponder Module

The Figure 2.1 shows the block diagram of the complete system on the transponder side. RF power of the carrier frequency at 1.3 MHz can be transferred through the inductive coil coupling that is externally attached. The wireless power transfer and power efficiency by different types of antenna are discussed in Chapter 6.

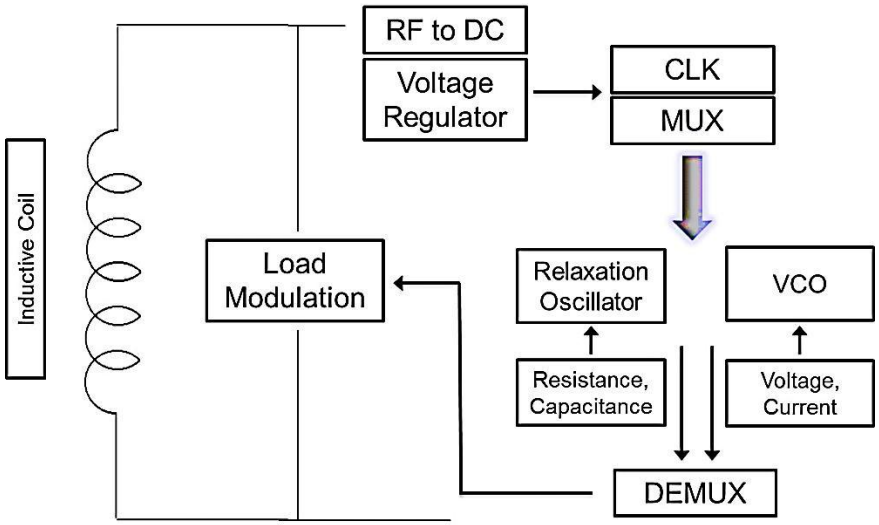

Figure 2.1 The block diagram of the complete system. A dual sensor system is illustrated for the chip design. The RF to DC (charge pump), two sensors, inductive coil antenna, and load modulation are external components.

Power from the carrier frequency is harvested through inductive coupling. The RF to DC (charge pump) and voltage regulator provide rectified output voltage nominally at 2.25 DCV as VDD supporting all other modules in the chip including ESD (electrostatic discharge). The CLK (local clock) generates a square wave at a nominal period of 200 ms. The MUX switches the VDD power rail every half period between two oscillators. When one oscillator is in operation for a half period, the other oscillator is off, and vice versa. This prevents the both oscillators from simultaneous operation at the same time in order to avoid the mutual interference. The DEMUX combines the two sets of the signals; each from each oscillator. Then the final output switches on and off the load modulator to achieve load modulation for wireless data communications.

2.3 The Reader of the System

The reader for the system is illustrated in Figure 2.2. It consists of a primary coil antenna that transmits the carrier frequency and power to the tag. At the same time, this antenna functions as a receiver for the load modulated signals from the tag antenna. The received signals are demodulated through the envelope detector and band pass filter. The design of the reader was done in previous research [22][23] . The data acquisition was achieved through a USB-6210 (National Instruments), data acquisition module. A LabVIEW (National Instruments) program was developed for the user interface. For the modulated signals, the sampling rate was set at 250 kS/s. When acquiring individual signals from the oscillators, the sampling rate was down-set at 125 kS/s due to the maximum sampling rate of 250 kS/s for the SB-6210. The program code is enclosed in Appendix C.

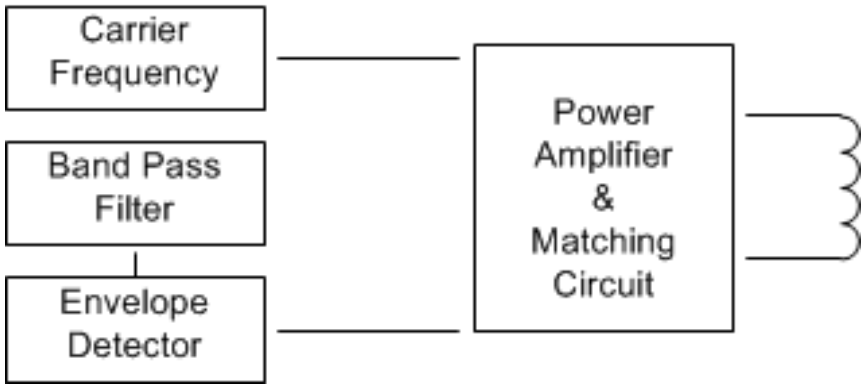

Figure 2.2 Simplified block diagram of the reader.

2.4 Feasibility Test

Multi-type sensors were selected for the feasibility test in order to achieve a capability of multi-type parameter readings. Among the four types of analog parameters mentioned in the introduction, voltage and current can be converted back and forth without a complicated circuit. Therefore, voltage, capacitance, and resistance were considered as input parameters to the circuit from the sensors.

A pH sensor and impedance sensor were chosen for the demonstration. A pH sensor generates a voltage as it reacts with a pH buffer solution. This sensor can be a good voltage source that is fed into the system. An impedance sensor generates a combination of resistance and capacitance. It provides the two analog parameters at the same time. Thus, two sensors can represent all three parameters.

2.4.1 Impedance Sensor

The impedance sensor consisting of interdigitated finger structure changes impedance when placed in solutions (Figure 2.3). The resistive change from 0 to 10 MΩ (short to open) and the capacitive change in 0 to 2 pF are varied from a PCB based sensor [20]. However, the ranges of the parameters can be differed depending on sensor design and material.

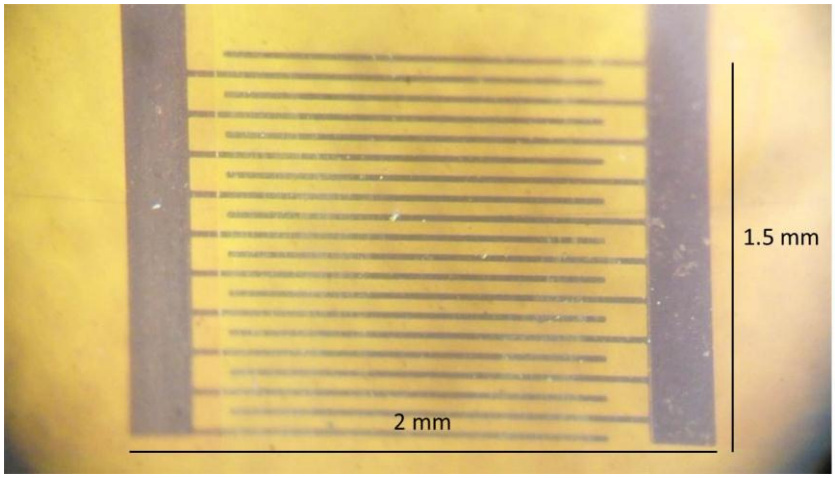

Figure 2.3 Flexible substrate based impedance sensor.

An impedance sensor that had been previously designed was used in this research. It had 200 Å of Cr (chromium) and 1500 Å of Au (gold). They were ebeam evaporated on a flexible polyimide substrate 125 μm I thickness. The total dimensions were 2 × 2 mm^2, and the sensing area was 1.5 × 2 mm^2.

2.4.2 pH Sensor

The pH sensor designed previously as in Figure 2.4 was used as voltage signal source. One electrode of the pH sensor was coated with IrOx (Iridium Oxide), and the other electrode was coated with AgCl (Silver Chloride). The IrOx as working electrode and AgCl as reference electrode together generated a potential change [24]. The voltage generated from this sensor was within the range of -0.3 to 0.6 DCV for the pH solution of pH2 to pH12 respectively.

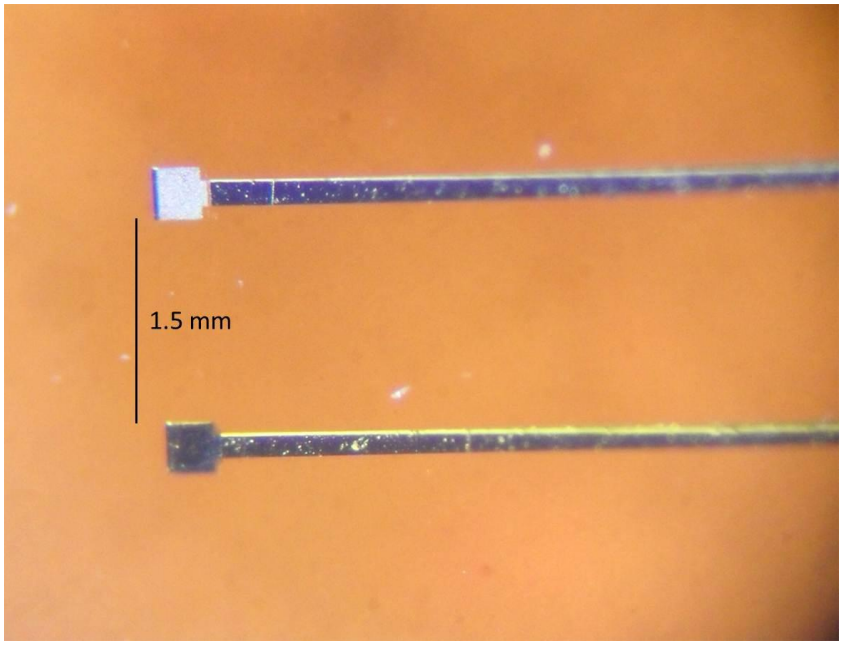

Figure 2.4 Flexible substrate based pH sensor. IrOx (gold colored) is working electrode. AgCl (silver colored) is reference electrode. Two electrodes in a solution generate a voltage variation by reacting to hydrogen ions.

CHAPTER 3

THE INTEGRATED CIRCUIT DESIGN

3.1 RF to DC (Charge Pump)

Inductive coupling has been chosen for the energy harvesting method for this research as it provides relatively higher power transfer than other energy harvesting methods. Inductive coupling is known as near-field electromagnetic coupling. A reader antenna can transfer power to a tag (receiving) antenna when both are inductively coupled. The coupling distance can be varied depending on the antenna size, shapes, material, etc. The investigation for changes in power transfer and efficiency among different antennas was performed. The results for the investigation can be found in Chapter 6. An IMS (Industry, Medical, and Scientific) frequency band of 1.3 MHz was chosen for the carrier frequency for this research due to a good immunity against tissue attenuation. An implant coil antenna using a charge pump that multiplies and rectifies the receiving AC voltage harvests the carrier frquency. The charge pump can be categorized into two ways; full wave and half wave.

3.1.1 Full Wave Charge Pump

An improved full wave charge pump from Kim [25] is shown in Figure 3.1. It requires three capacitors and four diodes per unit stage. In a negative cycle, $C_{p(+)}$ and C_s are charged. Similarly, in a positive cycle, $C_{p(-)}$ and C_s are charged. The voltage output after all stages can be calculated as

$$V_{out} = (2N - 1)(V_{IN} - 2V_{fwd}) \quad (3\text{-}1)$$

where N=number of stages and V_{fwd}=forward voltage drop on a diode. The higher number of stages increases output voltage. However, there is power loss on every diode by V_{fwd}.

The number of stages should be considered for the tradeoff between the output voltage and power loss [26][27].

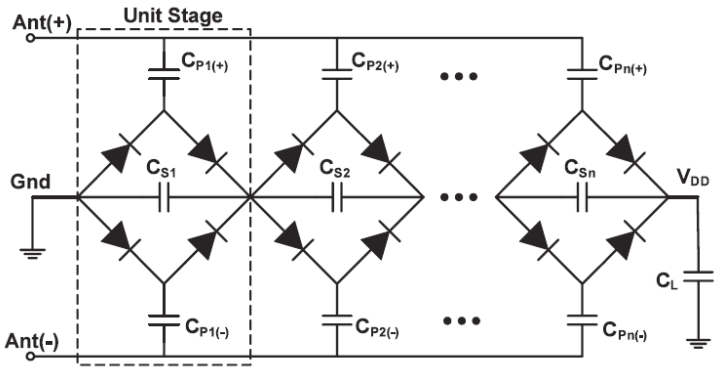

Figure 3.1 A modified full wave charge pump [25].

3.1.2 Half Wave Charge Pump

A half wave charge pump is widely used in RF harvesting fields such as passive RFID. It theoretically requires a half number of capacitors and diodes than a full wave charge pump does. Those two components occupy the majority of the space of the total chip dimensions. Reducing the number of those components will reduce the chip size significantly. In the Dickson's charge pump as illustrated in Figure 3.2, two capacitors and diodes are used in one stage [28-30].

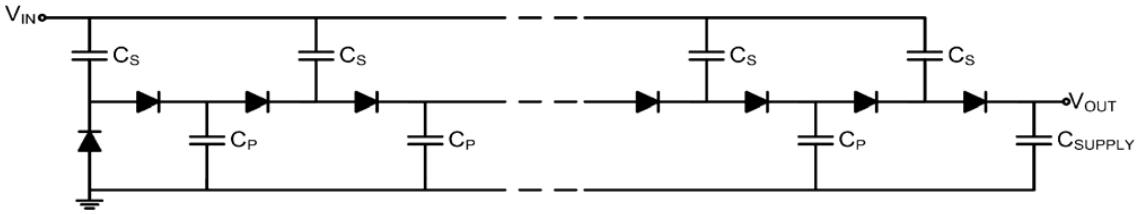

Figure 3.2 Dickson's half wave charge pump. Each stage requires two diodes and two capacitors [31].

The output voltage after stages can be expressed as

$$V_{OUT} = N\ (V_{IN}-V_{fwr}) \qquad (3\text{-}2)$$

As discussed in the full wave, the forward voltage drop made on each diode decreases the linear increment of output at each stage. To reduce the power loss at each stage, diodes that have low forward voltage drop are widely used; they are popularly known as Schottky diodes.

3.1.3 MOSFET Diode

A NMOS transistor as seen in Figure 3.3 can replace a diode. A MOSFET diode can be easily implemented and is available in any technology [32-34]. The output voltage expression can be obtained and is the same as equation (3-2). As seen in the Figure 3.3, the gate of a NMOS transistor is connected to the drain for the operation in deep saturation region. In this configuration, the voltage drops made across the MOSFET diodes are their threshold voltage (V_{th}).

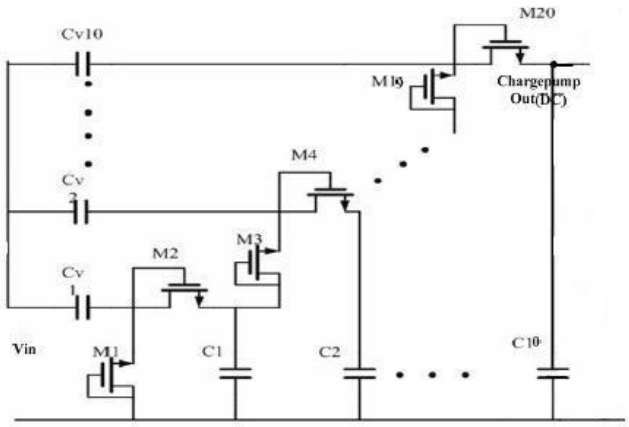

Figure 3.3 An example of half wave charge pump implemented by MOSFET diodes. It eliminates the diode fabrication process and reduces space [35].

3.1.4 Design Considerations for the Charge Pump in C5N Technology

There will be low transferred power when the two antennas are coupled at a long distance. In this case, more stages of a charge pump are needed to meet the required operating voltage for the transponder. However, it will undergo more power loss during the voltage multiplication. As previously discussed for all three charge pump cases, the critical consideration from the design point of view is how to decrease the voltage drop either from typical diodes or MOSFET diodes. The followings are possible solutions in general cases.

- Using a new technology

  A typical threshold voltage in 90-nm technology is around 0.25 V. Compared to 0.7 V of threshold voltage from the chosen C5N (0.5 μm) technology, the voltage drop is significantly smaller [36, 37].

- Native MOS transistor

  This can be done by undergoing the channel doping process. A channel is formed directly on the surface of the doped region without ion implantation. Therefore, it has a threshold voltage as low as 70 mV [33].

- Zero threshold voltage process

  This is a special fabrication process that eliminates the threshold voltage [38, 39].

- Fabricating Schottky diode

  Schottky diode can be laid during fabrication process [40][41].

The C5N technology does not officially provide any of the possible solutions mentioned above. Schottky diodes were fabricated and tested successfully with C5N in another research [42]. However, the forward voltage drop was measured over 400 mV. Even though the MOSFET diode is another solution for a charge pump, it is not practically applicable for biomedical applications. It will add to the significant power loss already seen through tissue attenuation causing unacceptable overall power loss. Thus, the external charge pump was considered. An off-chip charge pump was designed in two stages. It consisted of four low-voltage-drop Schottky diodes in one SOT26 package and four capacitors in 0603 package. As mentioned earlier, the overall size of the tag module is decided by the coil antenna. Therefore, an external charge pump is not a significant demerit for this case.

3.1.5 Corner Analysis

Active and passive electrical devices such as MOSFETS, diodes, capacitors, resistors, etc. can be fabricated and integrated on a single chip after undergoing a complex fabrication procedure. The fabrication procedure typically includes deposition, etching, patterning, and doping. Methods of each step vary depending on technology, purpose, material, time, quality, and so forth. During these procedures, variations occur. For example, masks can be slightly misaligned, etching can affect more on some areas than others, or doping can be injected less than others. These complicated processes and procedures cannot be applied identically even on the same devices, and they result differences in electrical characteristics (parameters) for device to device. This is widely known as the “fabrication process variation” [43, 44].

The fabrication process variation has always been a serious issue because it sometimes becomes the most significant factor that alters performance of chips, especially for high precision circuits. In many cases, fabricated chips behave differently with simulation results, and it causes faulty or non- operation. In statistically, mathematically, or design point of view, there have been attempts and some solutions to minimize the effects [45-47]. However, there always is a limitation to completely illuminate the hard-controllable phenomena. Instead, designers use a different method.

Corner analysis is an analysis method that simulates a circuit with possible maximum and minimum variations on each device. Instead of approaching a fabrication point of view, it is a method in circuit point of view. A circuit is versatility designed so that it operates within some tolerance for the variation of device parameters. The corner analysis is mostly performed with using model files that fabrication foundries provide. The model files are categorized in five different corners: TT, FF, FS, SF, SS. The TT means typical (nominal) values on the parameters. The rest of the corners represent Fast for the “F”, and Slow for the “S”. The first letter implies NMOS, and the second letter corresponds to a PMOS. For example, FS is fast NMOS’s and slow PMOS’s. Slow and fast are interpreted for minimum and maximum drain

currents respectively. The maximum and minimum values on devices for a particular fabrication technology were pre-determined by fabrication foundries after intensive simulations and experiments. These extreme values represent possible maximum variations in fabrication process, voltage, and temperature.

The corner analysis is, therefore, a simulation for worst scenario. Using this method, designers can predict the performance of their chips in varied parameters after fabrication. In conclusion, a circuit that passes and operates in all corners will be tolerated from non-operation against the variety of variation during or after fabrication.

Our circuit design also has been undergone massive corner analysis to make sure that the fabricate chip avoids a possible non-operation status in real life. The model files for all five corners used in this research are attached in Appendix A. These files have been provided by the MOSIS, and originally generated by the former foundry, AMI.

The corner analysis was not applied for all individual modules in our circuit. Some circuits such as MUX and DEMUX whose output results were not affected by those variations were not subject to be analyzed by this method. However, the regulator, CLK, two oscillators, and post-layout for the complete chip whose behaviors of performance could be changed have undergone the corner analysis. The results for each corner were provided in plots and table for convenient comparison.

3.2 Voltage Regulator

The level of unregulated output voltage at the charge pump varies depending on the separation between two antennas. The voltage can go more than 14 V if the antennas are center-aligned and placed at a close distance. In this case, the high voltage either will alter the oscillators' behaviors or damage the chip due to exceeding the gate breakdown voltage. To prevent these undesired results, the output voltage of the regulator should be fixed [27, 48].

Figure 3.4 shows the schematic (a) and layout (b) of the regulator. The nominal regulated voltage was set at 2.25 V. However, due to the variation mentioned in *3.1.5*, the voltage could fall or rise from the nominal voltage. As the system was for implantable purposes, a high operating voltage was not desired due to a risk for insufficient power to the implant. In contrast, a low operating voltage was not suitable either due to an insufficient span of input voltage for the two oscillators. Therefore, the desired operating voltage was pre-determined in between 2 V to 2.5 V. The regulator output was targeting middle point in the range. In this way, any voltage varied by different corners still could be within the range.

The regulator consists of three components: the voltage reference, the differential amplifier, and the voltage divider [30, 33, 35, 49]. The voltage reference provides a steady voltage by being biased by the resistor. This voltage is fed into one of the inputs of the differential amplifier. The other input to the amplifier is from the voltage divider. Three PMOS's are in deep saturation mode by having their gate and drain shorted. In this configuration, a PMOS transistor functions as a diode. The series connection of the PMOS's support another steady input to the amplifier.

As the CP_in varies from zero to 14 V, the two inputs of the differential amplifier vary as well. When the CP_in reaches at 2.25 V, the difference between the two values begins to remain the same or similar despite the varying CP_in. As a result, the differential amplifier provides a stable output.

The post-layout was simulated. The CP_in was swept from 2 V to 10 V. The variation of the output was plotted and compared among all corners in Figure 3.5 and Table 3.1 respectivley. The total variation of the output for the applied inputs was measured from 145 mV to 437 mV for FF and SS corners respectively.

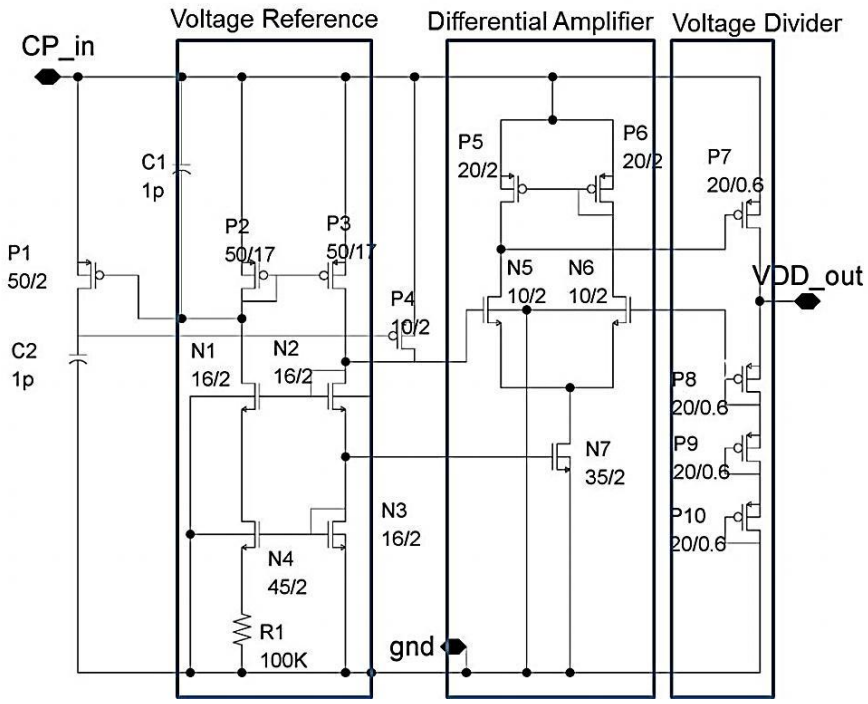

(a)

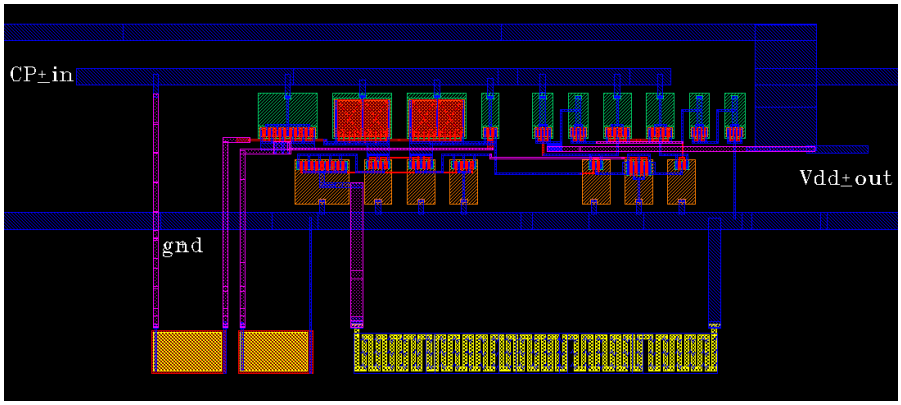

(b)

Figure 3.4 The regulator in schematic (a) and layout (b)

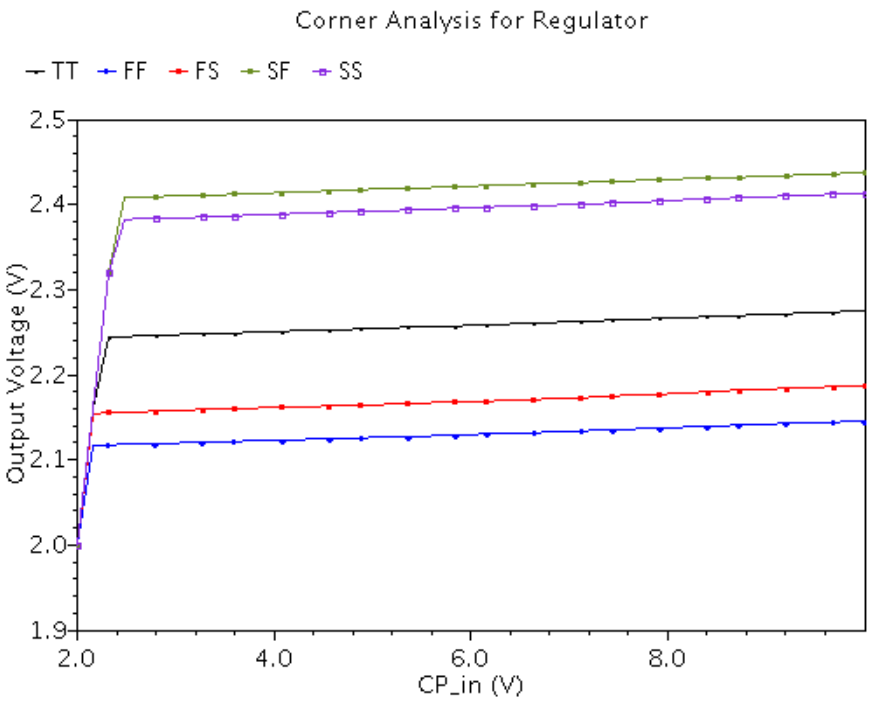

Figure 3.5 The results for the corner analysis. The input voltage was swept from 2 V to 10 V.

Table 3.1 The corner analyis for the regulator for the input sweep.

Corner	**CP_in (V)**		**ΔV (V)**	**CP_in (V)**		**ΔV (V)**
	2 V	10 V		Steady	10 V	
TT	2	2.275	0.275	2.245	2.275	0.030
FF	2	2.145	0.145	2.117	2.145	0.028
FS	2	2.187	0.187	2.155	2.187	0.032
SF	2	2.437	0.437	2.408	2.437	0.029
SS	2	2.413	0.413	2.382	2.413	0.031

However, the outputs for all corners began to settle with an input of below 2.5 V. Once the inputs reached this level, the outputs became very steady as the maximum variation was less than 32 mV for up to 10V of input. Hereby, we have verified that the outputs of the regulator were in the range between 2 V and 2.5 V regardless of different corners.

3.3 CLK Design

Different types of sensors can be mutually interfered when in the same fluid under simultaneous operations. To avoid the interference, sequential operations can be applied to the sensing circuitries. The sequential operation can be implemented using an isolation method by alternately switching the supplied voltage to the sensing circuitries. The path of the voltage supply is dictated by the MUX, and the CLK controls the MUX. Therefore, the clock period determines the operation period of each sensing circuit.

As the clock speed increases, the power consumption increases as well. The kinetic or liquid changes in the human body that sensors target to measure do not happen at a rapid pace. These two conditions drove a conclusion of 200 ms for the nominal oscillation period of the clock. However, the nominal clock period is not necessarily accurate. A difference of ±100 ms does not alter significant power consumption nor the sensing resolution. A period of 200 ms is a relatively very slow oscillation compared to other RF applications. This is hard for one single oscillation module to satisfy this requirement because such an oscillator would require very large capacitors to slow down the oscillation period. The large capacitors will increase the size of the total chip significantly. Additional design considerations are needed to decrease the CLK oscillation. The Figure 3.6 shows a block diagram of the CLK.

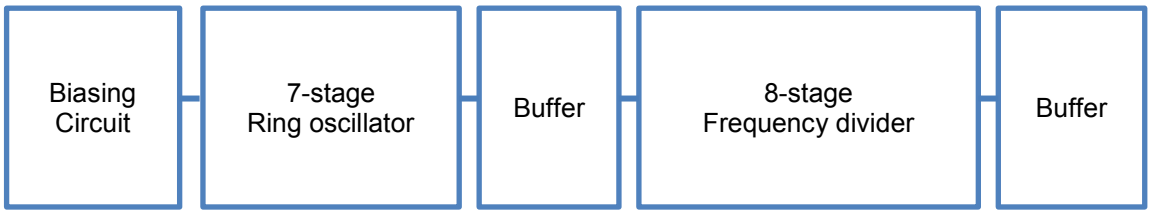

Figure 3.6 The block diagram of the CLK. An 8-stage frequency divider increases periods of the output of the 7-stage ring oscillator by 256 times.

In this CLK circuit, three modules slow the clock frequency to meet the specification. The first module is the biasing circuit. It limits the drain current of an inverter at all stages of the ring oscillator to slow down the oscillation frequency. The second module is the multiple stages

in the oscillator. Each stage experiences a gate propagation delay that is the main characteristic of a ring oscillator. The last module is a frequency divider. This module provides the major increment of periods. The frequency divider was implemented by using D-flip-flops in this design.

Figure 3.7 depicts the simple diagram of connections (a) and output (b) of a D-flip-flop. If the Q_bar is connected to D input, it generates the bi-stable toggle once every two clock cycles due to the closed loop by the feedback connection. It results a frequency divider as the output frequency of a D-flip-flop is a half of the input frequency (CLK).

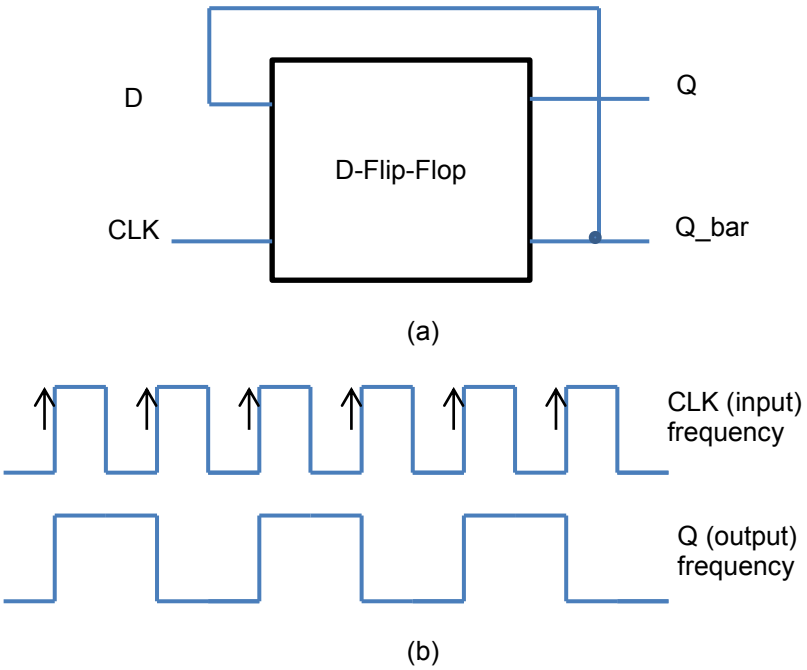

Figure 3.7 A D-flip-flop as a function of a frequency divider (a). The connection of Q_bar to the D input makes a bi-stable latch that generates a half frequency output. The results (b)

Figure 3.8 shows the schematic design of the biasing circuit, 7-stage ring oscillator and a buffer (a) as a single unit [50]. The schematic of a unit frequency divider is illustrated in (b). Each stage of the ring oscillator is biased by the P3, P4, N3 and N4. These four transistors are biased by a biasing circuit located on the left side of the ring oscillators. The biasing circuit provides a low current to the inverter. In this way, the propagation delay between stages will

increase to achieve a slow oscillation. In addition, each stage is connected to a 3 pF capacitor. These capacitors provide extra-long propagation delay.

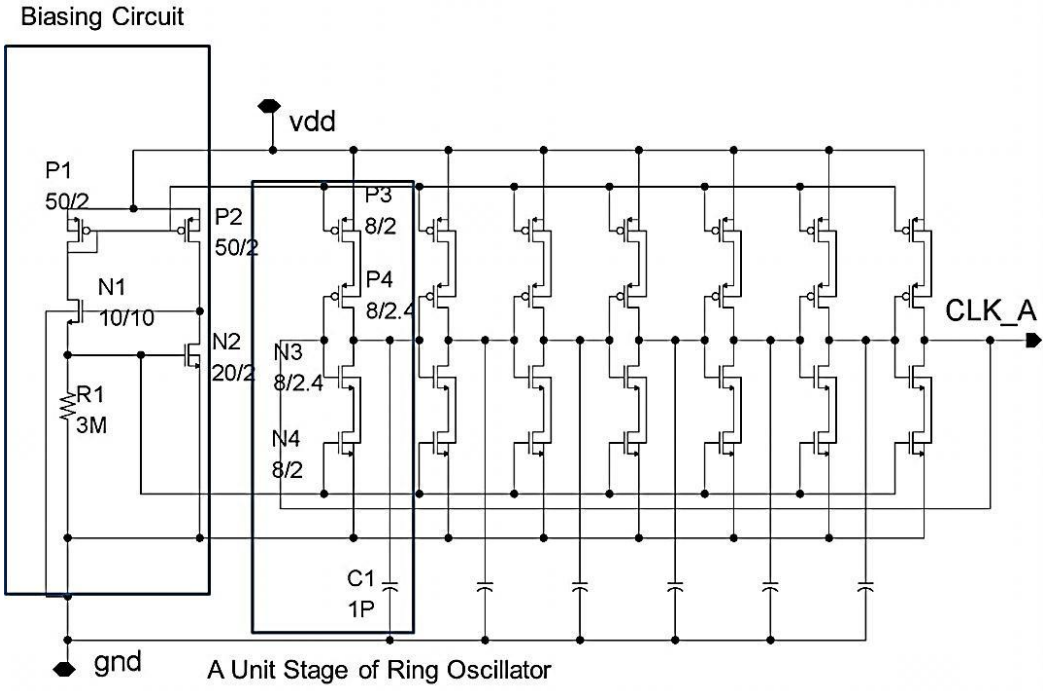

(a)

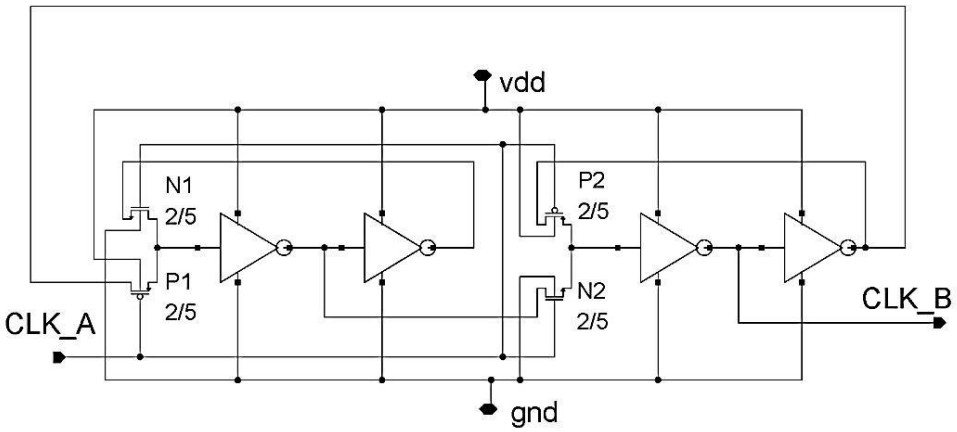

(b)

Figure 3.8 The schematic of the clock with a biasing circuit (a) and the unit frequency divider (b).

The frequency divider can further lower the output frequency of the ring oscillator. The implementation of a D-flip-flop as a unit frequency divider was achieved using two transmission gates and four inverters composing a master and slave latch parts using half of the afore-mentioned gates and inverters for each latch. Eight unit frequency dividers were cascaded in series connections to compose the 8-stage. This 8-stage unit delivers increment of input oscillation period or division of input frequency by 256 [51, 52].

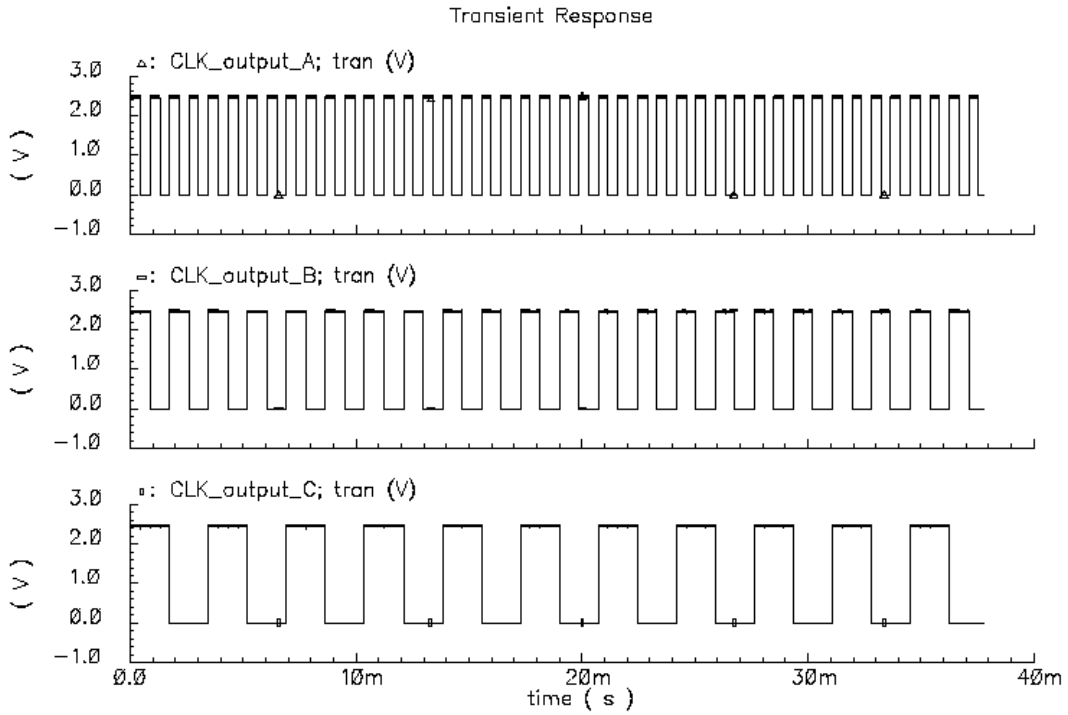

Figure 3.9 The output of the 7-stage ring oscillator (top), after the first frequency divider (middle), and after the second stage frequency divider (bottom).

Some selected outputs from the CLK module are shown in Figure 3.9. The 7-stage ring oscillator provides a period of 715 μs (top). After the CLK_output_A (top) passes the first stage of the frequency divider (middle), the frequency becomes a half of the input. After the second stage of the frequency divider, it becomes one fourth of the original input. When it passes all eight stages, the original input frequency reduces by 256, resulting the period of 183.07 ms.

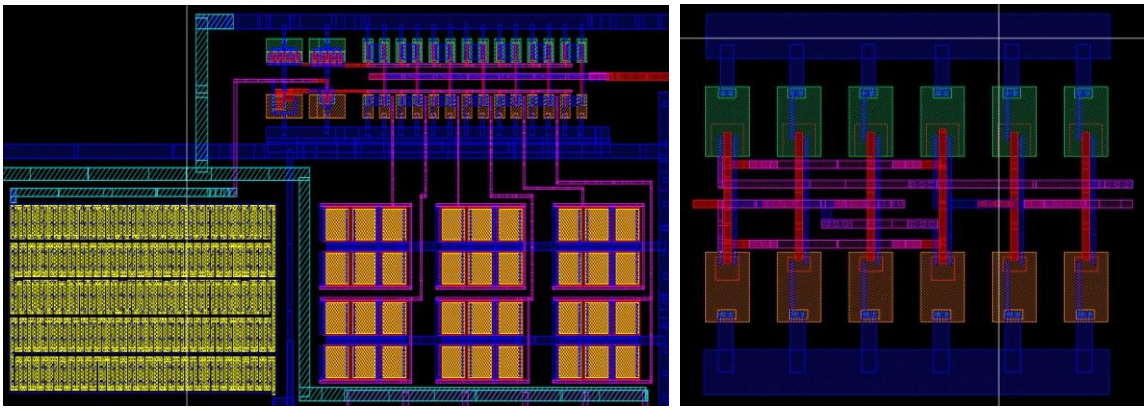

(a) (b)

Figure 10. The layout of the voltage reference and ring oscillator (a) D-flip flop (b)

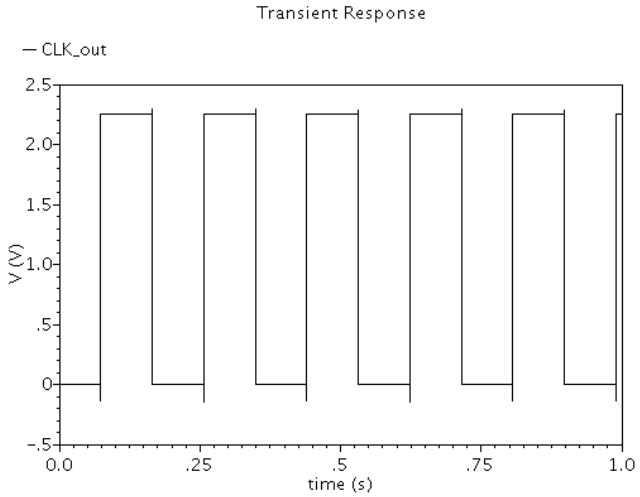

Figure 3.11 A simulation result for the CLK. A period of 183.07 ms was achieved.

Table 3.2 Corner analysis for the CLK.

CLK (at nominal 2.25 V)		
Corner	Period (ms)	Duty Cycle (%)
TT	183.07	50
FF	186.82	50
FS	198.73	50
SF	178.47	50
SS	175.52	50

The layouts of the CLK are shown in Figure 3.10. The biasing circuit, 7-stage ring oscillator, and buffer are shown in (a) and a unit frequency divider is shown in (b). The simulation result is shown in Figure 3.11. The CLK provided the oscillation period of 183.07 ms with duty cycle of 49.8 %. The total current consumption was measured at 3.4 μA. The results for the corner analysis were recorded in Table 3.2. The maximum variation was recorded from FS, and the variation was +24.8 ms.

3.4 Multiplexer (MUX)

As previously discussed in chapter 3.3, the simultaneous operations for the sensing circuitries are not preferred. Otherwise, faulty data can be collected. Thus, a MUX is needed to support the operation for one sensing circuitry at a time. For the dual channel operation, the MUX is a bi-stable path selector that has one input and two outputs. The output of the regulator is connected to the input of the MUX. In other words, the input of the MUX is the power rail that supplies the operating power. Each of the MUX outputs is connected to each sensing circuitry. As the MUX is toggled by the CLK, the connection of the input to the two outputs is alternately switched, providing the operating power for one sensing circuitry at a time.

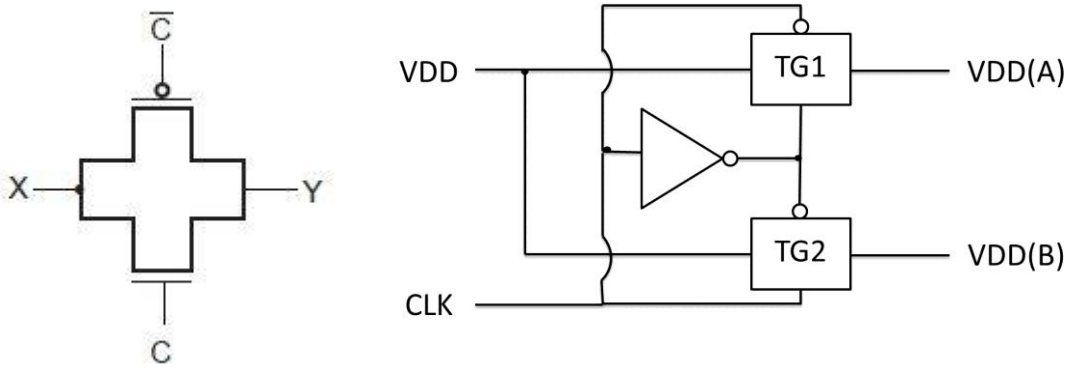

(a) (b)

Figure 3.12 A unit transmission gate (a), and MUX (b) using two transmission gates and one inverter. Every half a cycle of the CLK toggles the VDD line to support the power line to each sensing circuitry [53].

The MUX design is based on transmission gates as in Figure 3.12 (a). When the clock is on, both the NMOS and PMOS transmit the X to Y. Figure 3.12 (b) shows a two-channel MUX. Two transmission gates are connected with the same CLK but in opposite status. When the CLK is HIGH, TG2 will be enabled. Then, VDD will appear on VDD (B), and vice versa. In this way, the VDD rail is toggled for each sensing circuitry at every half a cycle of the CLK. Since the CLK cycle was set for 200 ms, the sensing circuitry alternately changes the operating status at every 100 ms. For this MUX design, only six MOSFET's are required including the inverter. This design requires the least number of MOSFET's compared to other types. It works as a path selector, but here fills the role of a MUX [54, 55].

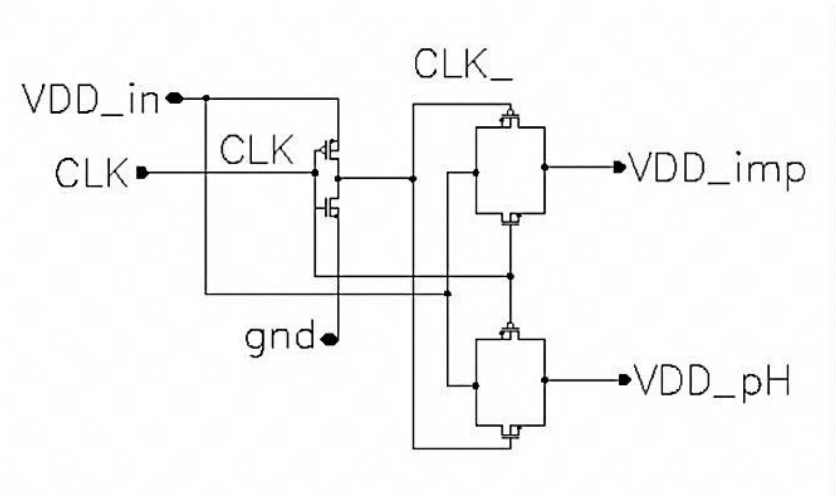

Figure 3.13 The transistor level of the implemented MUX using six MOSFET's.

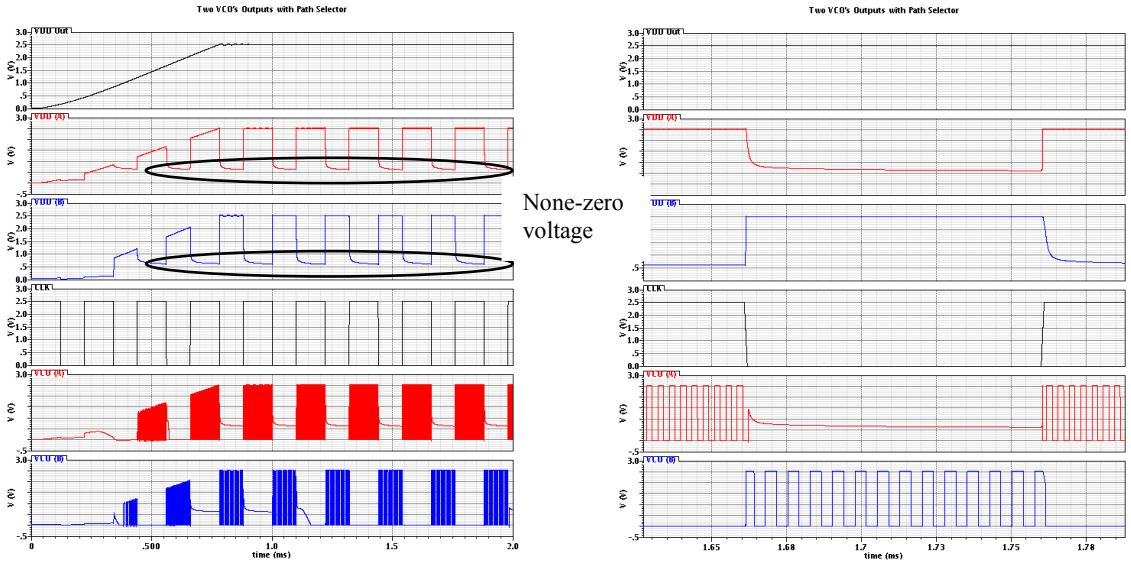

(a) (b)

Figure 3.14 The voltage remainder during the off-stages. The operating voltage for the two oscillators still remains as high as the threshold voltage (a) and a close look (b).

The Figure 3.13 shows the implemented MUX in transistor level. The impedance and pH sensing circuitries (as being used as the feasibility test) receive the VDD at every 100 ms. Even though it faithfully engaged as prescribed by its MUX role, there was an undesired result from the design. As shown in Figure 3.14, the VDD did not remain completely at zero, but the threshold voltage (V_{th}) during the off-stages. This remaining voltage could cause mutual interference between sensors. Therefore, the design in Figure 3.13 was modified as in Figure 3.15.

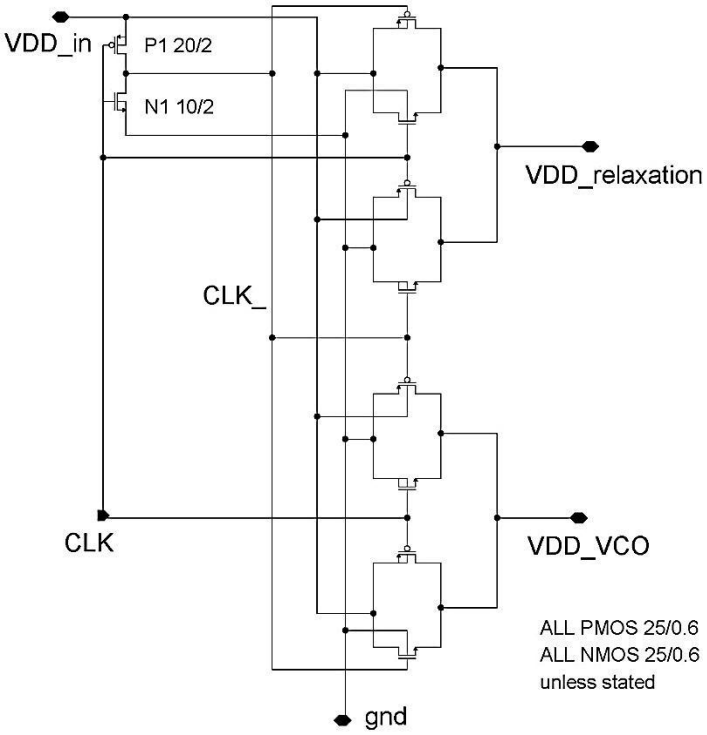

Figure 3.15 The proposed two-channel MUX using ten MOSFET's including the inverter. The voltage remainder during the off-stage is pulled down to zero.

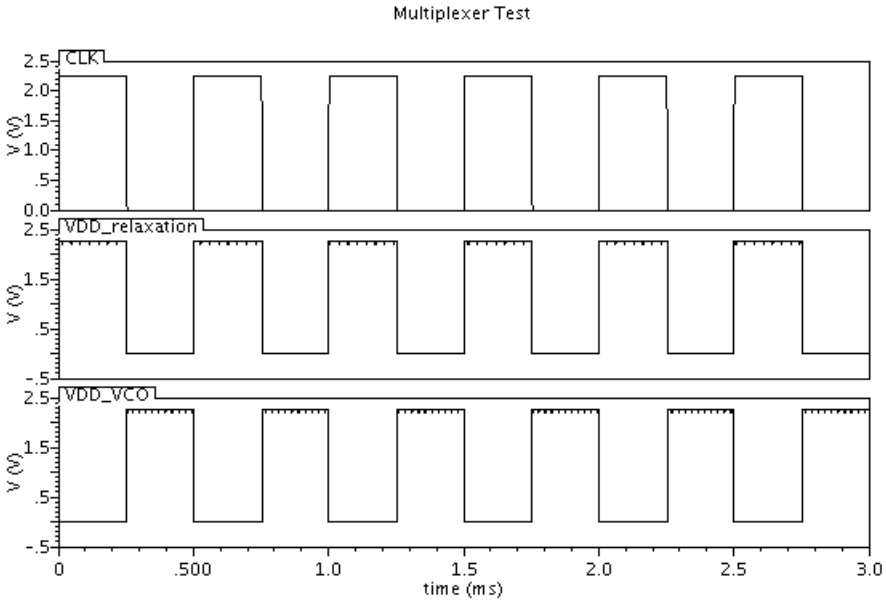

Figure 3.16 The threshold voltage appearing during the off-stages is pulled to zero by the additional transmission gates.

Two more transmission gates were added from the previous design. Each one was engaged to each path and pulled the voltage remainder to zero by being connected to the ground. Figure 3.16 shows the results. The threshold voltage remaining during the off-stages disappeared. There was no more leakage voltage generating to another sensing circuitry while one was in operation.

The layout was completed for the MUX in Figure 3.17. One input that was the output from the regulator was switched by the CLK and fed into the sensing circuitries. Total of five NMOS's and PMOS's each enabled the multiplexing.

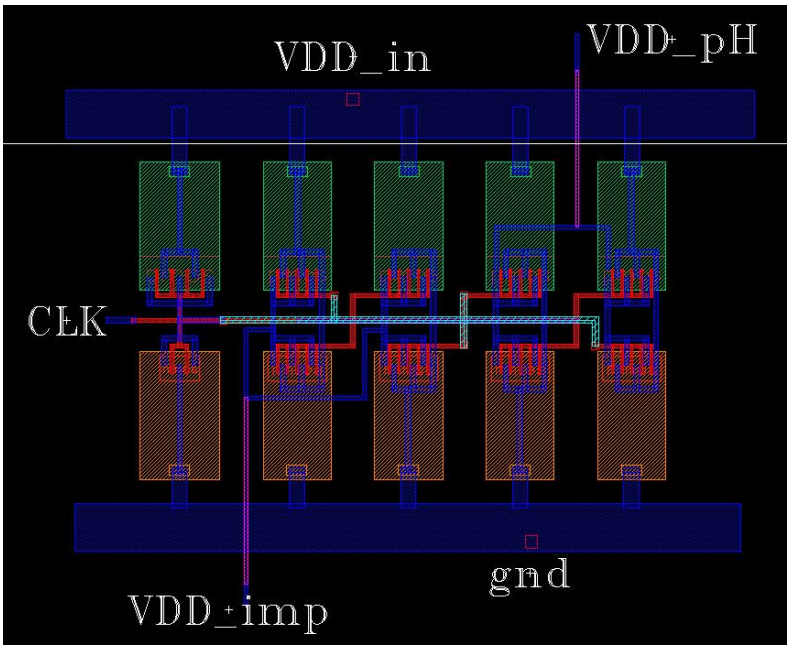

Figure 3.17 The layout for the MUX. Ten MOSFET's are implemented to compose the path selector for carrying the VDD to each sensing circuitry.

3.5 Relaxation Oscillator for Input Parameters of Capacitance and Resistance

3.5.1 Basic Operation of Relaxation Oscillator

From the four previously mentioned parameters, capacitance and resistance are the first inputs considered to the sensing circuit. These inputs are sensed and a corresponding signal is generated by an oscillator. Among different types of oscillators, a relaxation oscillator (RO) has a versatile operation for both capacitive and resistive inputs as the oscillation is dominated by the RC time constant in the negative feedback loop. The RC time constant determines the time function of charging and discharging on the feedback loop. As both resistor and capacitor directly affect the oscillation behavior, a RO is excellent for responding to impedance variations as an input. Thus, a RO has been adapted to engage with both capacitive and resistive inputs. A typical RO is illustrated in Figure 3.18.

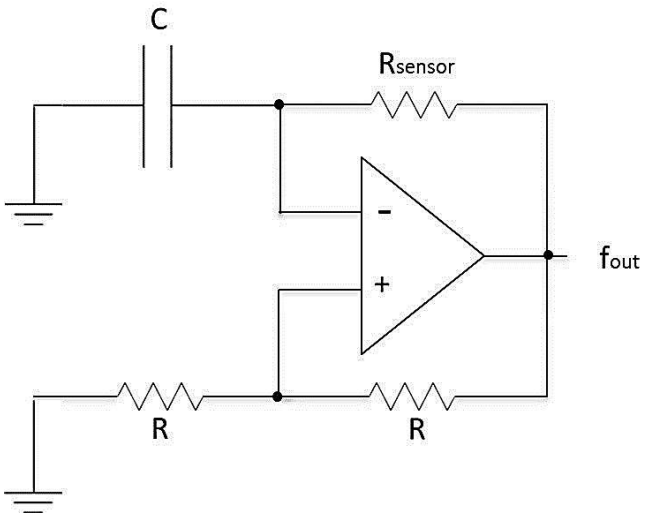

Figure 3.18 A simple circuit diagram of a relaxation oscillator. The resistor and capacitor on the negative feedback affect the oscillation behaviors.

The oscillation frequency will vary with the time constant, $\frac{1}{R_{sensor} \cdot C}$ where the R_{sensor} is the resistance of a sensor. In this case, there will be zero-oscillation when the R_{sensor} is zero. Therefore, a modified RO was proposed as Figure 3.19 [22].

The impedance sensor is subject to be tested in extreme values including short and open. For the case of the Z_{sensor}=0 where the Z_{sensor} is the impedance of a sensor, the R_2 prevents the zero-oscillation. For the case of the Z_{sensor}=∞, the (R1+R_2)·C engages for the oscillation. Therefore, the R_1 and R_2 prevent the zero-oscillation condition for any impedance input.

When R_{sensor} > R_1, the change on the feedback is less than when R_{sensor} < R_1 due to the parallel connection. Since the R_{sensor} is considered from short to open, the optimum choice for R_1 is vague. However,once the R_1 chosen it will determine the range of the output frequency (resolution) from short to R_1. For example with the R_1 = 100 Ω, the change of the output frequency will be varied much better when R_{sensor} < 100 Ω than R_{sensor} > 100 Ω as the 100 Ω will dominate the equivalent R in parallel connection between R_{sensor} and R_1. Therefore, the selected R_1 becomes the decision of the resolution between R_{sensor} = 0 to R_{sensor} = R_1.

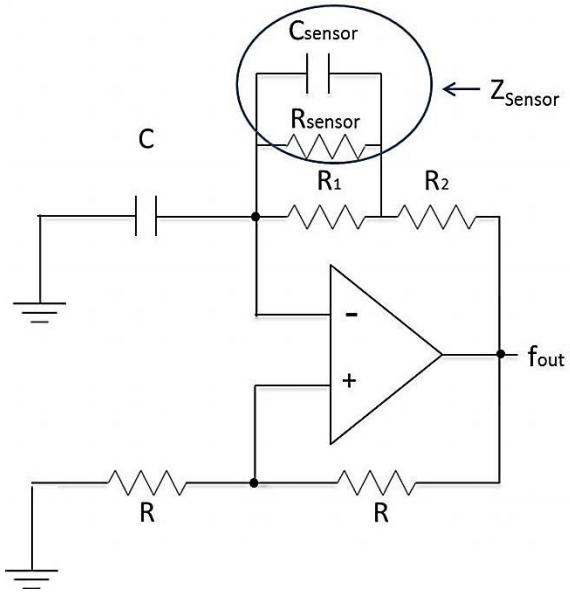

Figure 3.19 The proposed connections on the negative feedback for the system. The R_1 and R_1 are for preventing non-oscillation against short and open scenarios on Z.

The effectiveness of the R_{sensor} and the C_{sensor} for the oscillation can be adjusted by controlling their values. For example, the effectiveness of the C_{sensor} will be diminished for a

large C. Instead, the R_{sensor} will affect majority of the oscillation. The opposite effect would occur for opposite sizes of the components' values. However, if C becomes as small as a few tens of pico-farad, the circuit may become non-oscillation due to off-boundary of the oscillation from the operational amplifier. Depending on the operational amplifier, the C should be carefully chosen. In this system, the non-oscillation behavior was experienced at around 40 pF for the C. For a stable operation, a 50 pF was chosen in the actual circuit. This low capacitance is beneficial to increase the effectiveness of the changes of the C_{sensor}.

3.5.2 Implementation of Relaxation Oscillator

The implemented relaxation oscillator is shown in Figure 3.20 and 3.21 as the schematic and the layout respectively. The R_1 and R_2 are 400 kΩ and 80 kΩ respectively. An amplifier, voltage reference and current mirror are used to compose a self-biased folded cascade differential amplifier [56] [57].

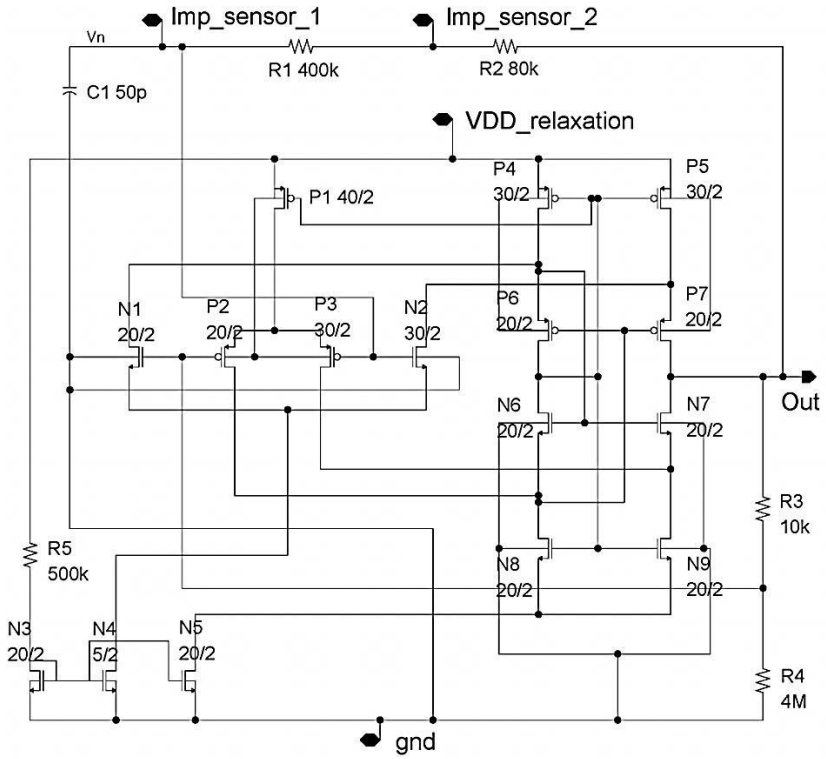

Figure 3.20 The proposed relaxation oscillator in schematic. The voltage reference and current mirror bias the operational amplifier for stable operations and less power consumption.

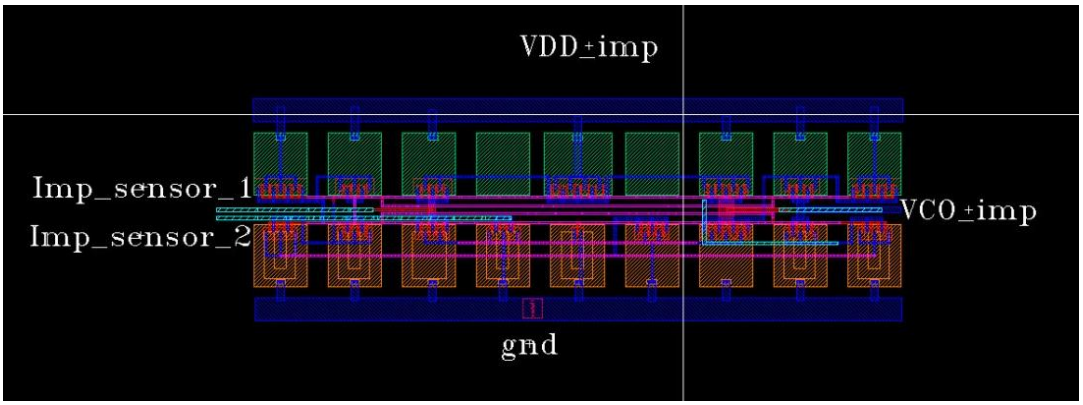

Figure 3.21 The layout for the relaxation oscillator. The capacitors and resistors in the layout are not shown due to relatively large sizes

3.5.3 Simulations and Results

The relaxation oscillator was first checked with three different resistive inputs. Figure 3.22 shows the changes in output frequency from 18.6 kHz, 12.35 kHz, and 9.83 kHz for the input of 1 Ω, 100 kΩ, and 400 kΩ respectively.

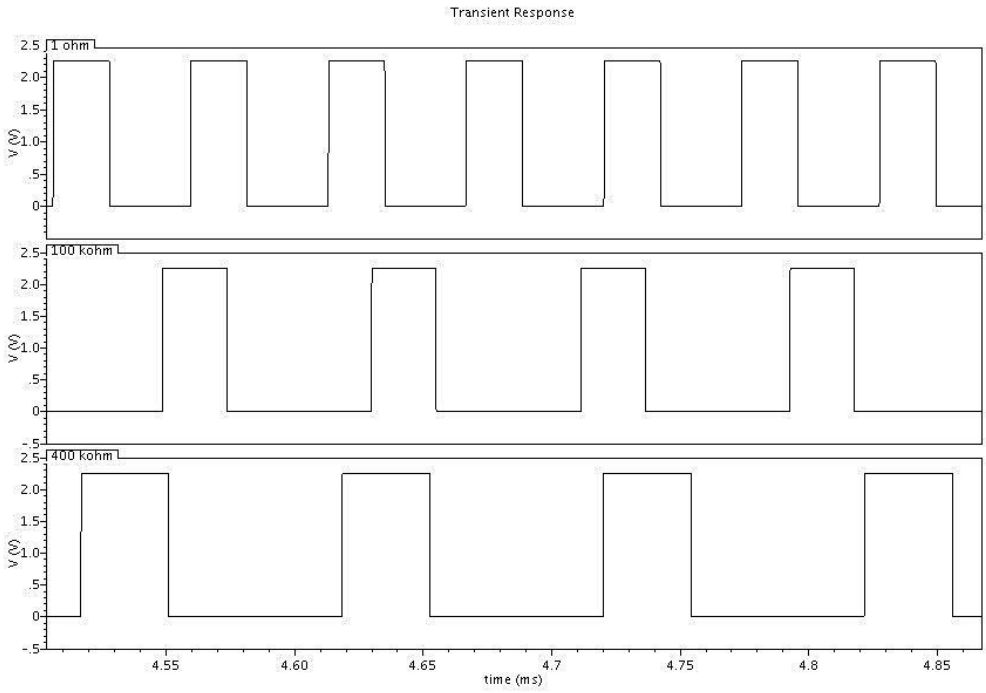

Figure 3.22 The change in output frequency for three different levels of input.

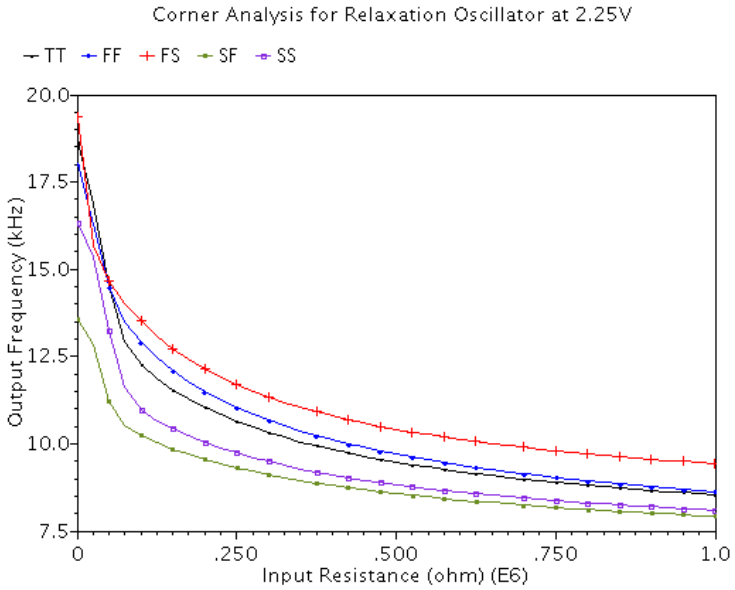

Figure 3.23 The output frequency versus input sweep from zero to 1 MΩ in corner analysis.

Table 3.3 The results of the corner analysis for the relaxation oscillator. The SF drove the least frequency variation as 10.21 kHz from zero to 500 kΩ for input changes.

Relaxation Oscillator (at nominal 2.25 V)			
Corner	0 Ω (kHz)	1 MΩ (kHz)	Δf (kHz)
TT	18.63	8.54	10.09
FF	18.03	8.63	9.40
FS	19.37	9.44	9.93
SF	13.56	7.92	5.64
SS	16.32	8.10	8.22

The relaxation oscillator was simulated for an input sweep. The input resistance was swept from zero to 1 MΩ. The results of the corner analysis are plotted in Figure 3.23 and compared in Table 3.3. The input beyond 500 kΩ tended to saturate the output frequency at a certain value, and this value was not far from the output for an input of 500 kΩ due to the exponential decrement for the frequency versus input sweep. The variations of output frequency were measured at 10.09, 9.40, 13.20, 5.64, and 8.22 kHz for TT, FF, FS, SF and SS cases respectively. The SF corner made the lowest resolution that was 5.64 kHz. However, this

resolution was considered as a quantitatively large enough number for measuring and distinguishing the intended solutions. This resolution is sufficient to preclude the need for amplification that requires the cost of implementing another amplifier in the system.

3.6 Voltage-Controlled Oscillator (VCO) for Input Parameter of Voltage

3.6.1 Basic Operation of VCO

A voltage-controlled oscillator is an oscillator whose output oscillation depends on a voltage input. In other words, a variation of input voltage to an oscillator will correspond to a variation of output frequency. This is a direct method for frequency manipulation. Therefore, a VCO has been adapted for voltage and current inputs. A current can be converted into a voltage by means of a simple parallel connection with a resistor. Therefore, a voltage and a current are unified and treated as one same parameter for this research.

3.6.2 A Current-Starved VCO with Current Linearization

Among variety of VCO types, a ring oscillator has been selected for this research due to a simple operation, implementation, and frequency manipulation. A modified 7-stage ring oscillator is in Figure 3.24 [50]. On each stage, the P5 and N4 are starved for current due to limited current caused by the P4 and N5 (current limiters).

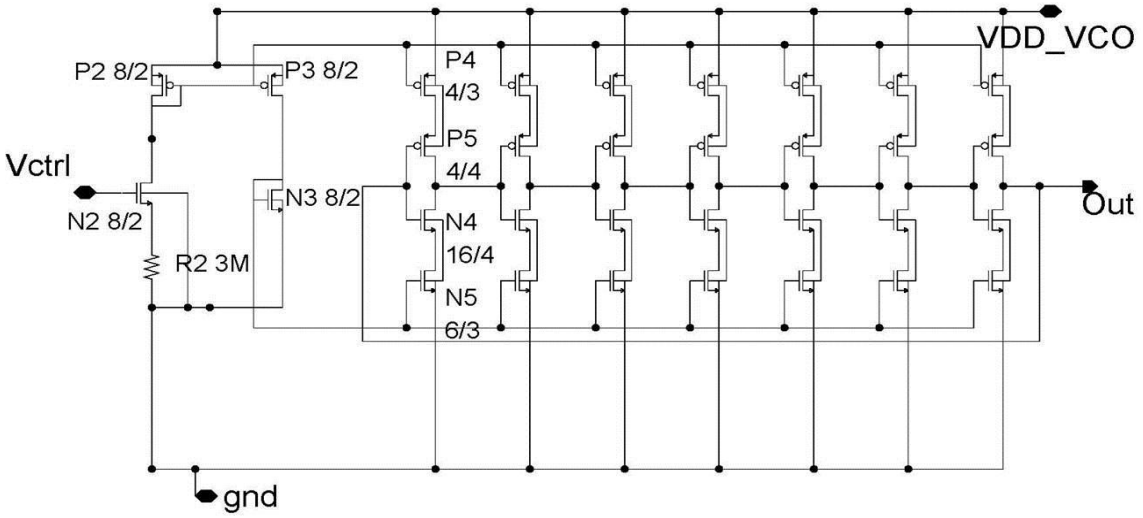

Figure 3.24 A current-starved VCO. The current to the 7-stage ring oscillator is controlled by V_{ctrl}, and it functions as VCO

The current in the current limiters is mirrored from the current control unit composed of P2, P3, and N3, and this current is controlled by the gate voltage (Vctrl). A large width for the N2 with the R2 will cause $V_{gs} \approx V_{th}$ on this transistor, which is independent of V_{ctrl}. It results in a linear current increment by an increment of V_{ctrl}. The result is shown in the Figure 3.25. For the input from 0.75 V to 2.05 V, the output frequency spanned from 7.5 kHz to 42.76 kHz.

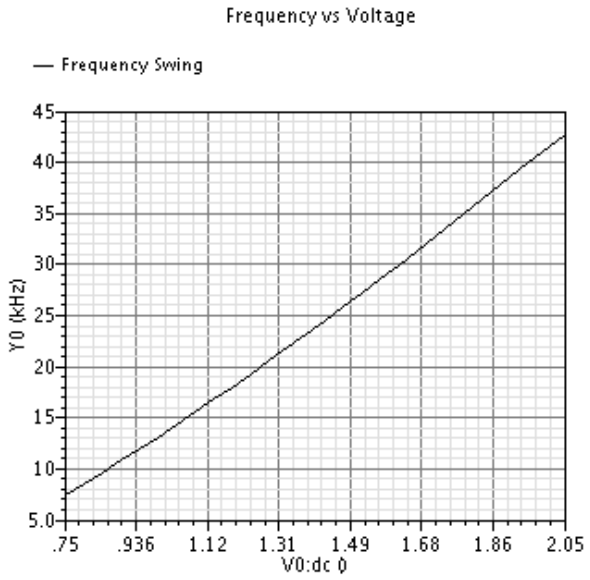

Figure 3.25 The output frequency versus input voltage. Linearizing the gain of the VCO delivers linear relationship between the output frequency and input voltage.

3.6.3 A Current-Starved VCO with Low Gain

Despite of the excellent linearity and the low current consumption of 800 nA, the frequency span from the previous VCO was too large, wasting bandwidth. This was attributed to a large VCO gain. To reduce the gain, the R1 was attached in Figure 3.26 [58]. The R1 limited the gain that was the ratio of the injected current to the ring oscillator over the V_{ctrl}. In results, the slope of the output was lowered. The P1 and N1 were added to form a voltage shifter that provided 1.1 V. This voltage was subject to be added to the sensor-generated voltage in case sensor voltage became negative values. This method avoided any negative inputs to the VCO.

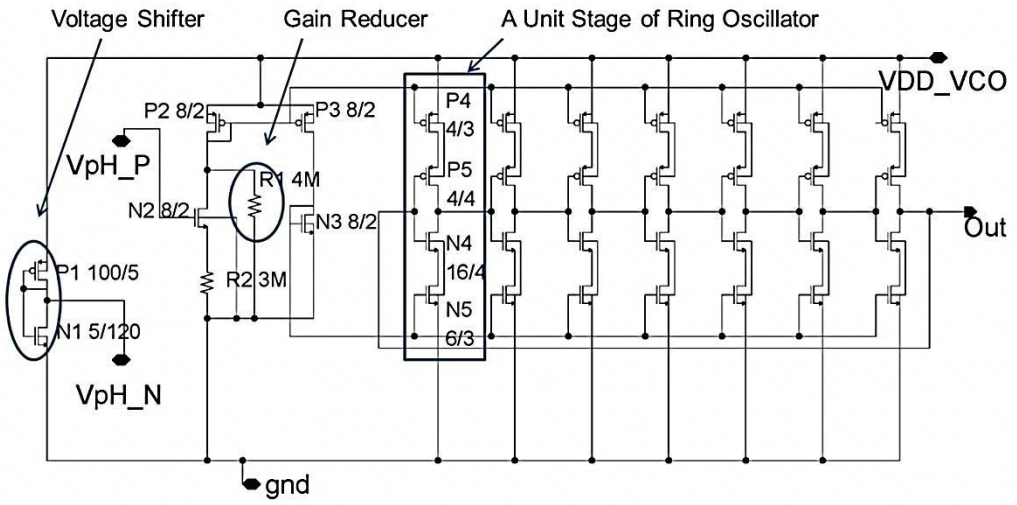

Figure 3.26 A modified VCO with a gain reducer. The additional resistor, R1, reduces the gain to control the frequency span. The voltage divider adds 1.1 V to eliminate negative voltage input to the VCO from a pH sensor.

3.6.4 Simulations and Results

The circuit in Figure 3.26 was laid out in Figure 3.27. In the actual layout for the final chip-out, the rotation and location of the components were modified to optimize the space.

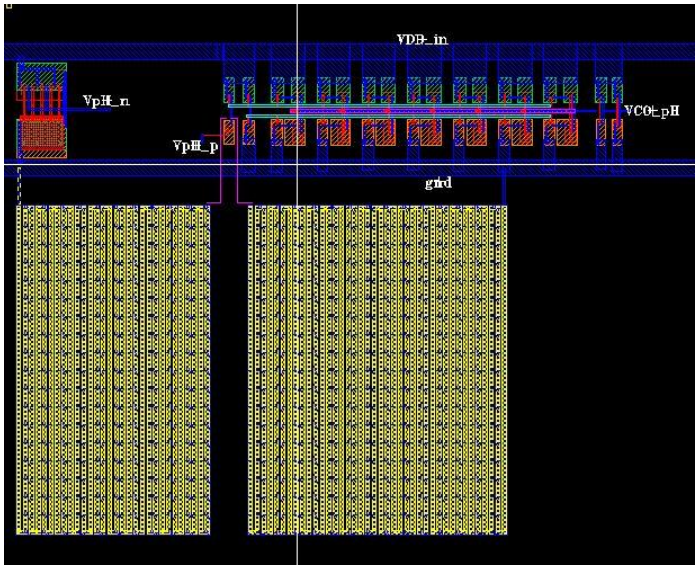

Figure 3.27 The layout of the VCO with a voltage divider. The two resistors linearize and reduce the gain of the VCO.

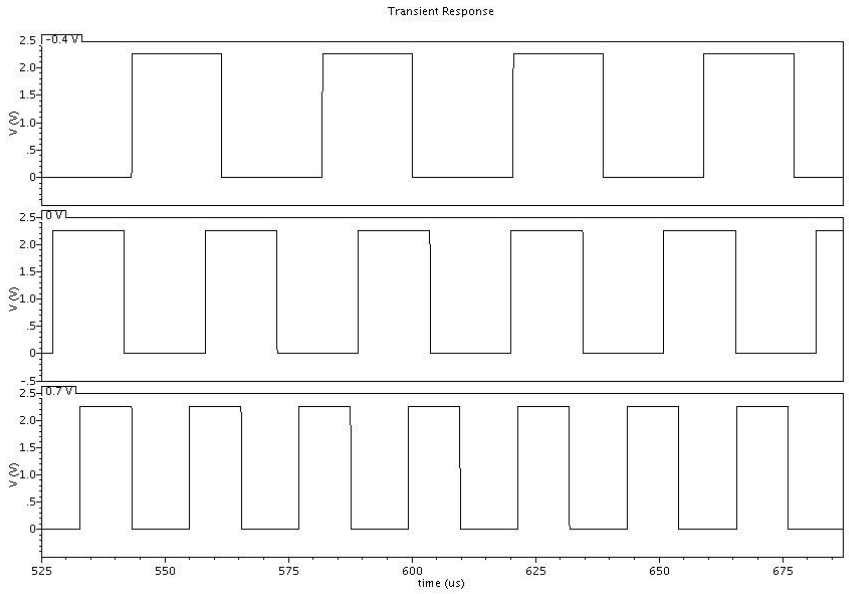

(a)

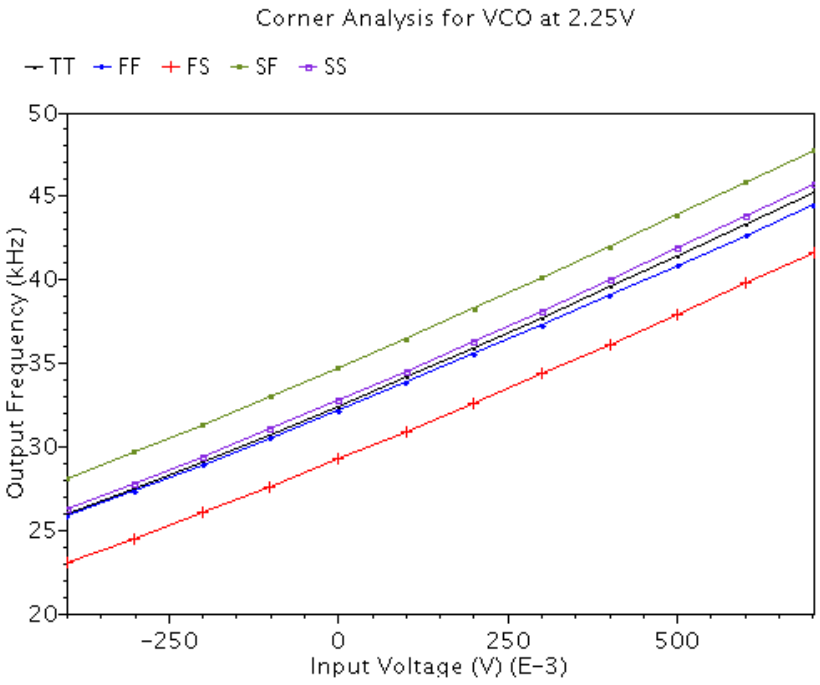

(b)

Figure 3.28 The outputs of the VCO. The output frequencies for three input voltages (a) and for an input sweep from -400 mV to 700 mV in the corner analysis (b). A good linearity and less gain were achieved.

Table 3.4 The results of the corner analysis for the VCO. The frequency spans for all corners are very close each other

VCO (at nominal 2.25 V)			
Corner	-0.4 V(kHz)	0.7 V (kHz)	Δf (kHz)
TT	26.00	45.30	19.30
FF	25.90	44.50	18.60
FS	23.10	41.60	18.50
SF	28.10	47.80	19.70
SS	26.30	45.70	19.40

Three distinguished inputs were applied for the performance verification as shown in Figure 3.28 (a). For the inputs of -0.4 V, 0 V, and 0.7 V, the outputs were obtained at 26 kHz, 32.2 kHz, and 45.3 kHz respectively. In Figure 3.28 (b), the input voltage was swept from -400 mV to 700 mV in a corner analysis. The results are shown in Table 3.4. The frequency span for each corner is less significant since the frequency span can be easily adjusted by tuning the gain reducer. Linearization and identical oscillation behavior for all corners are more significant since it is imperative that be able to predict the output results for particular inputs.

3.7 Demultiplexer (DEMUX)

The output frequencies from the two oscillators need to be modulated, forming a single signal. Unlike typical designs for the other general RF modulators, the modulation method for this system can be simpler as the two signals (frequencies) come sequentially, not simultaneously. Therefore, an OR gate was implemented to combine the two signals in sequence as shown in Figure 3.29 for the schematic (a) and the layout (b).

When the first oscillator is in operation, the other oscillator is in off-status. The output of the DEMUX, the logic OR, will purely be the frequency from the first oscillator as the second oscillator is providing a signal of zero. For the other half of the period, the output from the DEMUX will be switched to the second oscillator. It is a simple implementation of the DEMUX, but it functions properly to perform its duty. Four transistors perform the role of a modulator.

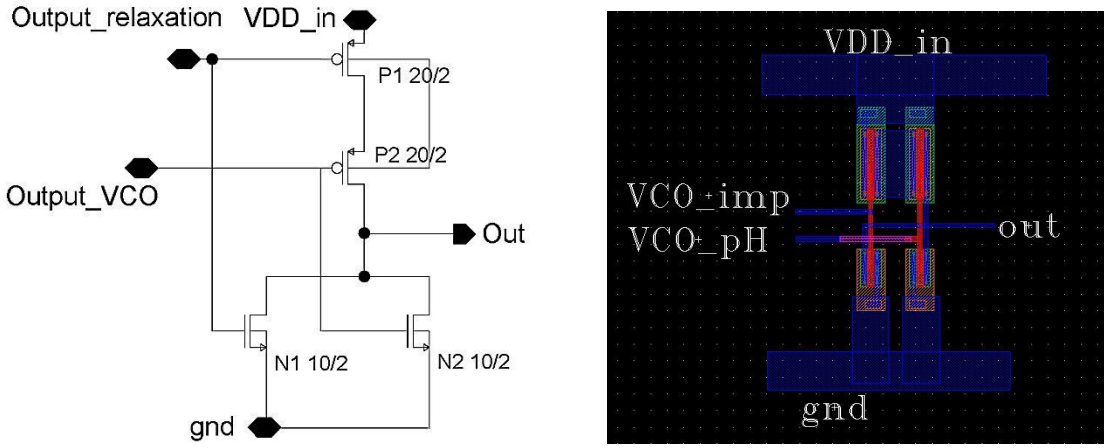

(a) (b)

Figure 3.29 The DEMUX in schematic (a) and layout (b). An OR gate was implemented to modulate the two sets of frequency into a single signal.

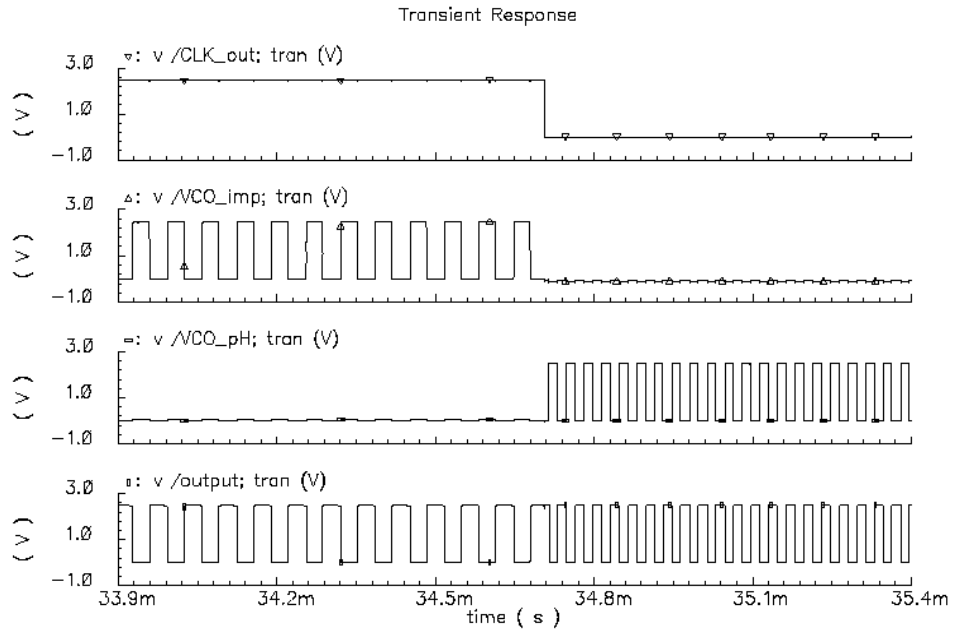

Figure 3.30 The output of the CLK (top), Impedance sensor (second), pH sensor (third), and DEMUX (bottom). The DEMUX modulates the two oscillation signals into one by combining them.

The Figure 3.30 shows the results of how the DEMUX performs along with the CLK. When the CLK (top) is HIGH, the relaxation oscillator (second) receives the power, and becomes operational. Meanwhile, the VCO provides signal of zero due to no power supply.

Since the DEMUX is an implementation of logic OR, the combined (modulated) signal is purely the same as the output of the relaxation oscillator. As soon as the CLK turns to LOW, the result becomes opposite. The output of the DEMUX is solely from the VCO. In result, the final output of the DEMUX carries both signals in a sequential order. The CLK, outputs of the oscillators, and modulated signal are all synchronized in this manner.

The modulated signal is subject to trigger a load modulator that is off-chip in this design. The gate of the load modulator (NMOS) that is connected across the tag antenna is switched by this modulated signal.

3.8 Load Modulation

The voltage amplitude at the reader antenna is sustained at a steady value as long as a resonant circuit remains at the tag antenna. The modulated signal from the DEMUX can be fed into the load modulator that is a single NMOS whose drain and source are connected across both ends of the tag antenna as illustrated in Figure 3.31. As the modulated signal triggers on and off the gate of the load modulator, the impedance of the chip changes the impedance of the resonant circuit. This intentional impedance mismatching will appear at the reader as a voltage drop due to the power loss. In this manner, an amplitude modulation can be performed using an envelope detector. The speed of the amplitude change corresponds to the switching speed on the load modulator. Since the NMOS's on-off speed is done by frequency of the modulated signal, this frequency can be extracted by detecting the reader's amplitude [59, 60].

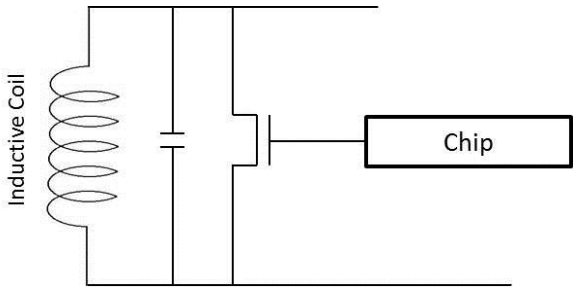

Figure 3.31 Load modulation method. The chip impedance alters the impedance of the resonant circuit. It causes the reader to experience a voltage drop. The amplitude modulation can be achieved to detect the voltage drops.

Among important aspects of designing this first generation chip, the verification of proper operation was the top priority rather than extra features or compactness. Therefore, if there could be any percentage of possibility that a module could fail, it was taken out of the chip and connected externally. These components are the charge pump and load modulator. In the next generation chip, those two components will be considered to be integrated into a single chip.

CHAPTER 4

COMPLETE SCHEMATIC, LAYOUT, AND FABRICATED CHIPS

4.1 Pre-requisites for Complete Design

Prior to completing the chip design in layout level, the method to test the chip after fabrication should be considered. All the steps for the design of modules and the IC for our design constraints are presented here.

4.1.1 PADS

Pads are extensions of pins for inputs, outputs, or input-outputs connections. During tests, data acquisitions can be made through pads probed directly or indirectly. When a bare-die is used internal wire-bonding is required.

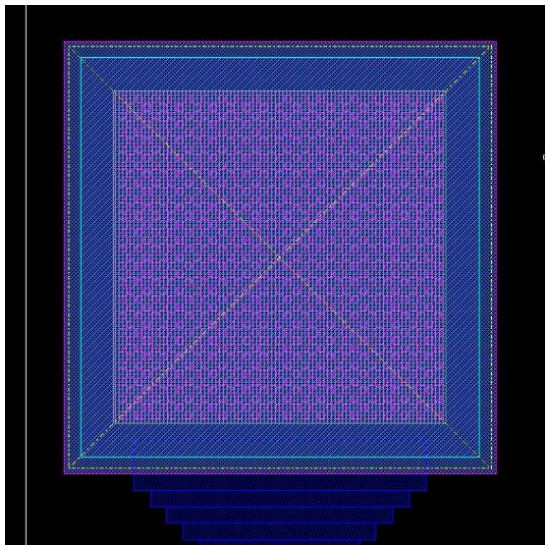

Figure 4.1 An actual image of the pad

The wire-bonds connect the pads of the die to pads of the package. Pad size, location, and space between them should be taken care of, and there are industrial specifications for the minimum and maximum values. In our design, we used pre-laid pads based on designs

obtained from Professor Brunvand [61]. The original pads generated by Tanner evoked design rule check (DRC) errors and would not pass the DRC test. Brunvand further modified these pad designs to make them free of DRC errors. The pad design used for all the pins in our design is shown in Figure 4.1. The pad has a dimension of 78 μm^2. The space between pads was 12 μm, which made the pitch 90 μm. This is in compliance with the industrial standards for pad design and wire-bonding. A total of 60 pads were used in our design.

The pad in the Figure 4.1 has a dimension of 78 μm^2. The space between pads is 12 μm, which makes 90 μm for pitch. This is one of industrial standards, and the minimum size for wire-bonding through a commercial packaging company. A Total of 60 pads were used in our chip design.

4.1.2 Electrostatic Discharge (ESD) Protection

The second consideration is ESD (electrostatic discharge) protection. IC chips are fabricated from silicon, silicon dioxide, metal, etc. These materials can be permanently damaged when they experience a high voltage. Static electricity is the most common cause of high voltage related damage. Often times, this static electricity can be delivered from the human body, testing equipment, and (or) other sources. Mistreats with careless handle can damage chips during experiments. Hence, circuits of ESD protection were considered and laid in the circuit.

The pre-laid ESD circuits implemented also followed the designs obtained from Brunvand [57]. They were designed using the same technology, C5N (0.5 μm). Hence, we were able to directly apply the ESD circuits in our layout design. The ESD circuits were pre-designed for eight different purposes; in, out, bidirectional, in-out, in-out with no resistors, ground, corner, and no-connection. Depending on the data direction, pin type, connection type or connection location, any one of them could be applied. Figure 4.2 shows the actual layout of all ESDs, pads and their connections.

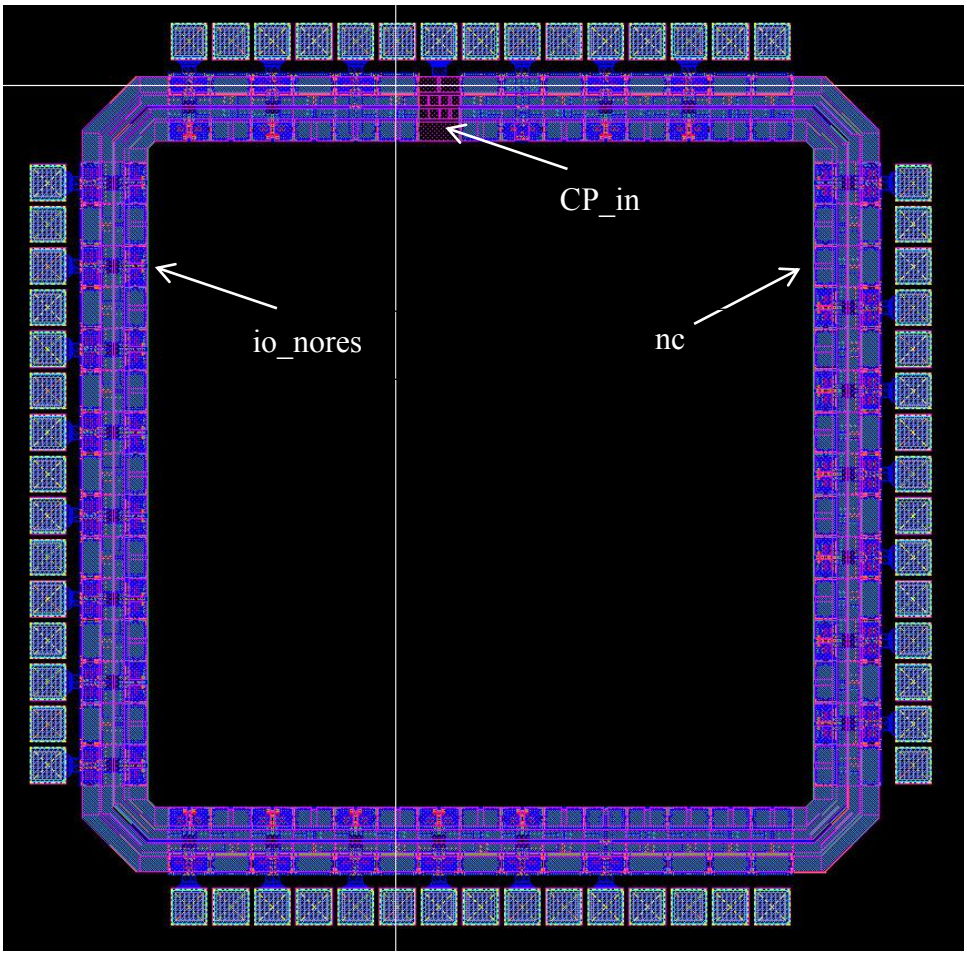

Figure 4.2 The layout for pads and ESD's. Totoal of 60 pads were laid and surrounding the chip. The ESD's of io_nores is with no resistor built in series with the signal path. They were used for all input, output, and in-out pins. The pad of "nc" were used for non-use pads

An ESD requires an operating voltage to function. As the scheme of our power harvesting receives an AC signal and converts it into DC after a regulator that is located inside the core, it is impossible for either the AC or DC from going through the ESD's due to the absence of supplied voltage. Therefore, there is a need for at least one pad that is free from ESD, and it is marked as CP_in in Figure 4.2. The external charge pump rectifies the AC signal to DC. The unregulated DC can then freely pass through CP_in pad to the regulator. Once the voltage is regulated inside the core, it will support all other modules including the ESD's. Thus, other input and output pads are protected against electrostatic charges by the ESD's.

4.2 Complete Schematic and Layout

The pads and leads were assigned for pad names. The Table 4.1 explains the details of each pad and assigned name with brief description. Figure 4.3 through 4.5 shows the final schematic design, layout, and extracted view respectively.

Table 4.1 Pin descriptions

VDD_relax	VDD for the relaxation oscillator
Imp_sensor_1	Probe 1 for the impedance sensor
Imp_sensor_2	Probe 2 for the impedance sensor
VCO_P	Positive terminal for voltage input for the VCO
VCO_N	Negative terminal for voltage input for the VCO
Ouput_VCO	VCO output
VDD_VCO	VDD for the VCO
CLK_out	CLK
VDD_out	VDD output from the regulator
vdd!	VDD input for the ESD's
CP_in	Input for rectified voltage after a charge pump
gnd!	Ground
Output_relax	Output of the relaxation oscillator
Output	The output of the modulated signal

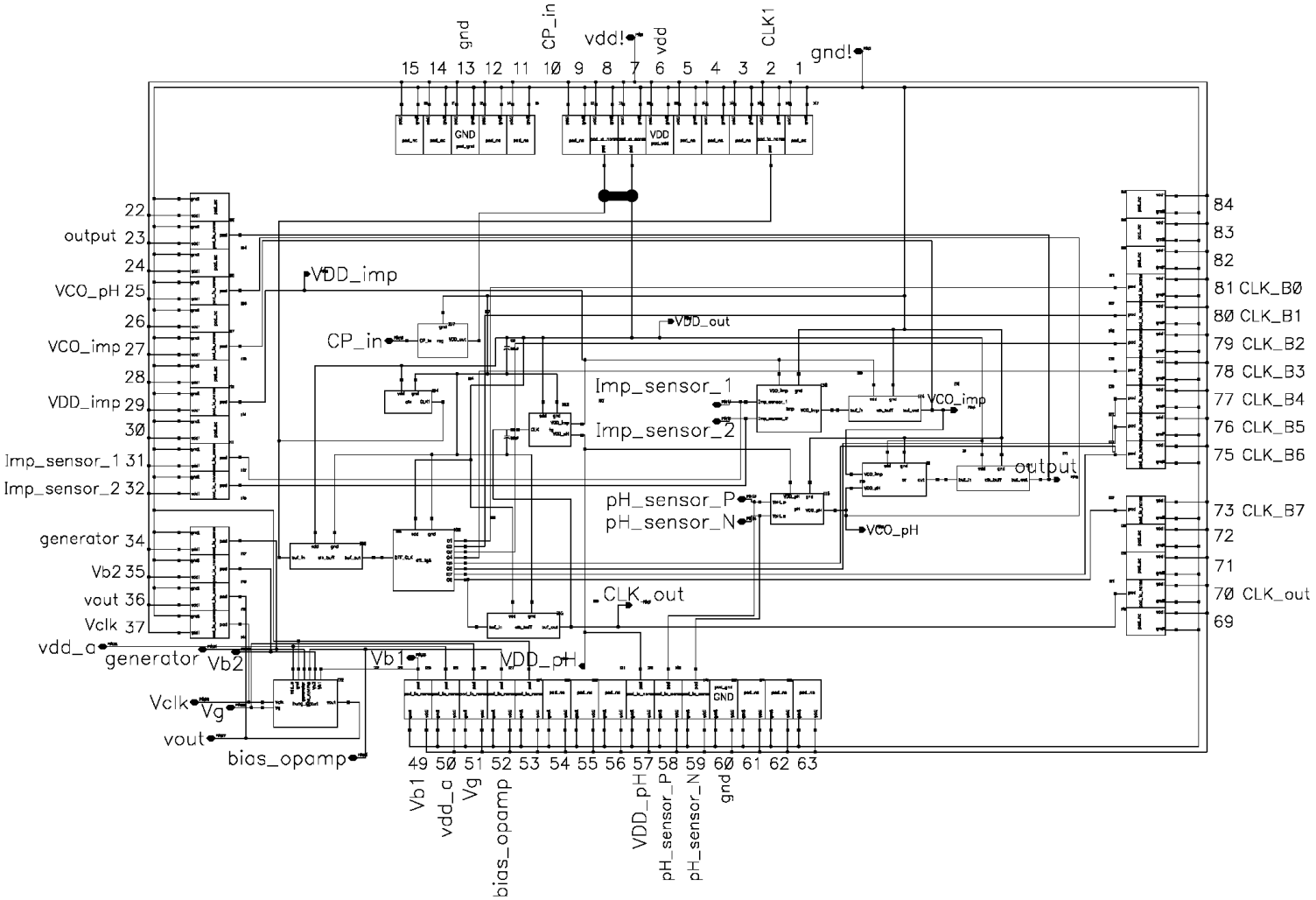

Figure 4.3 The schematic design of the complete chip

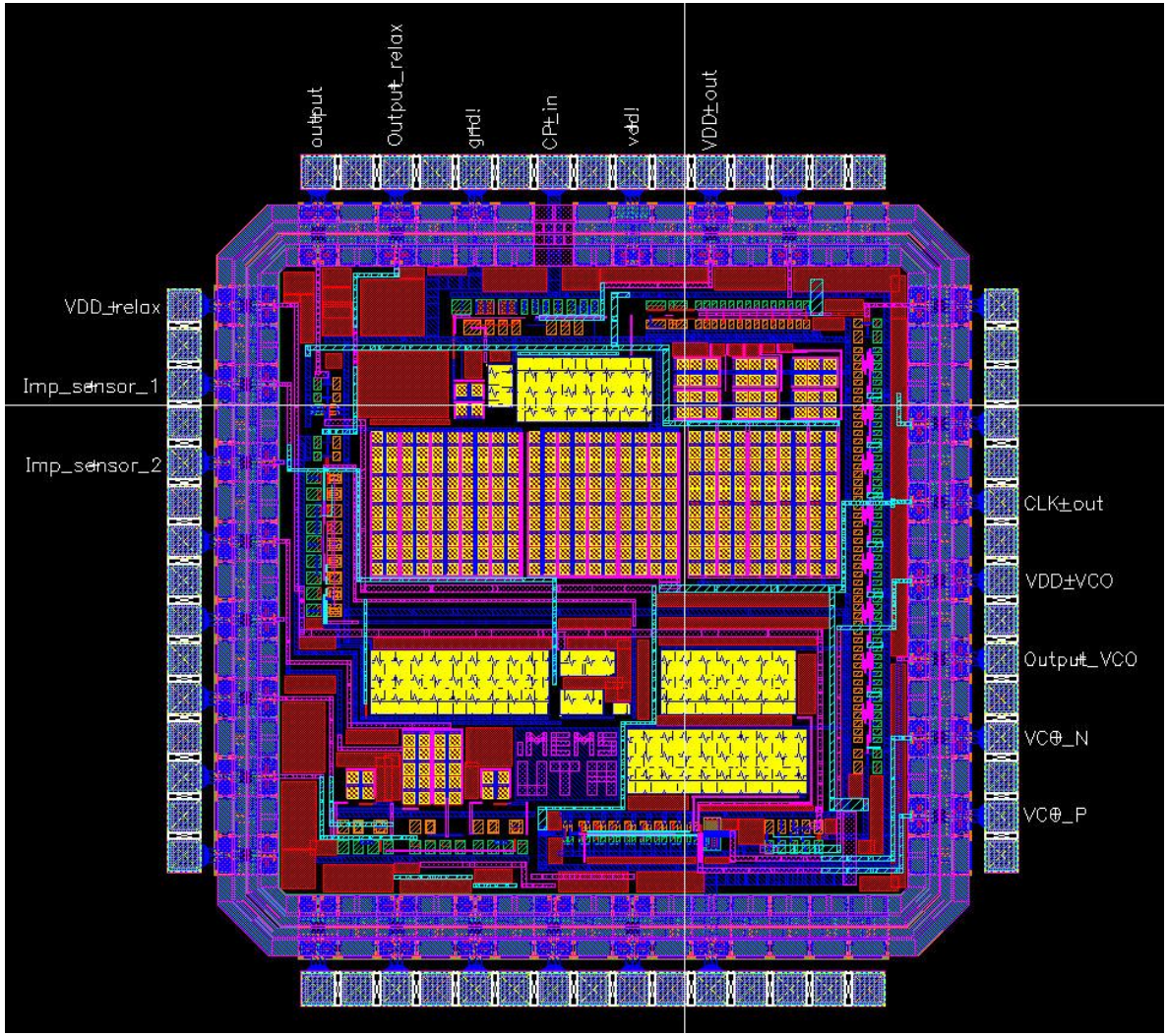

Figure 4.4 Layout of the complete chip

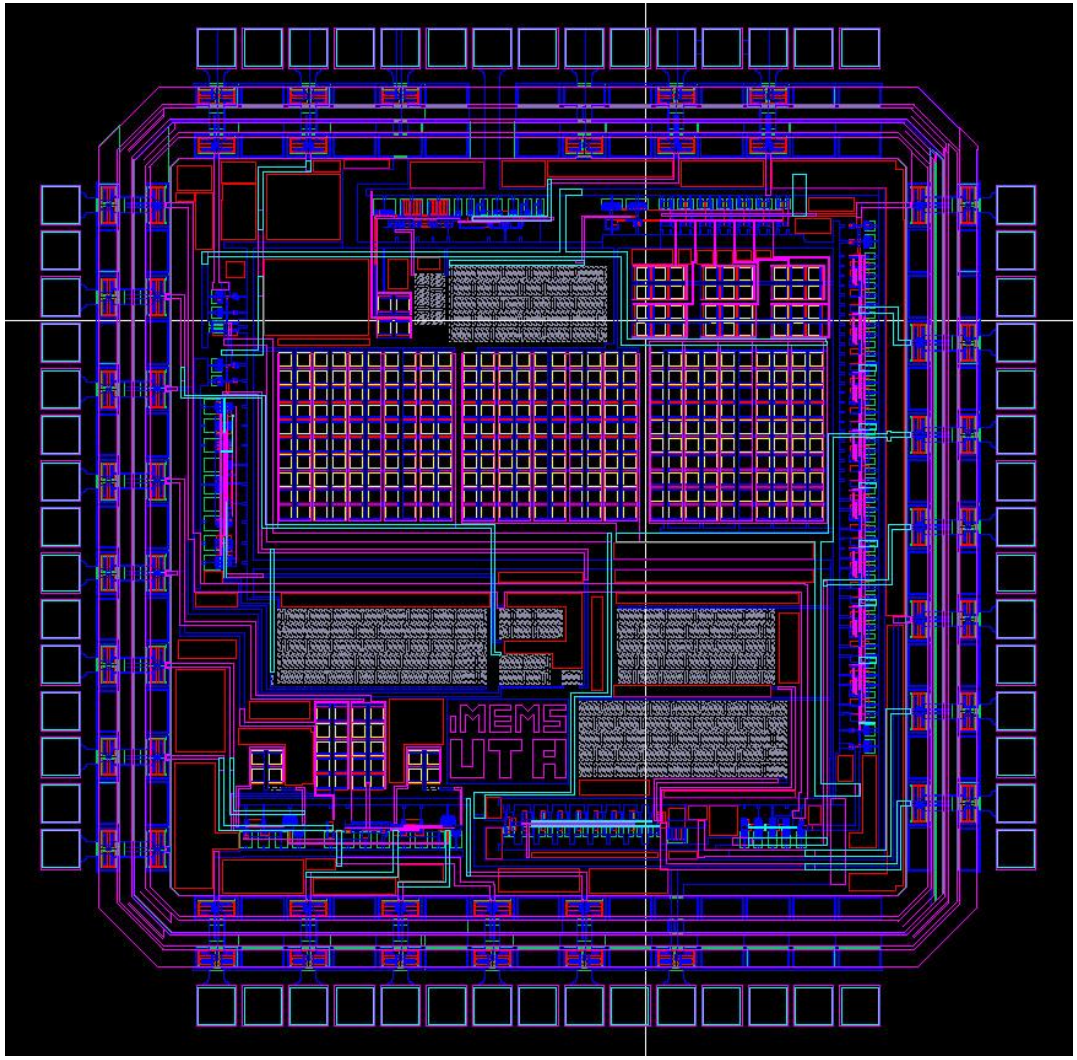

Figure 4.5 The extracted view for the complete chip

4.3 Simulation Results from Post-Layout

The post-layout was simulated. One of its resultss is shown in Figure 4.6-7. The simulation of transient response was carried out for 600 ms to verify at least two or more CLK cycles. Figure 4.6 shows the CLK (top) and modulated signal (bottom).

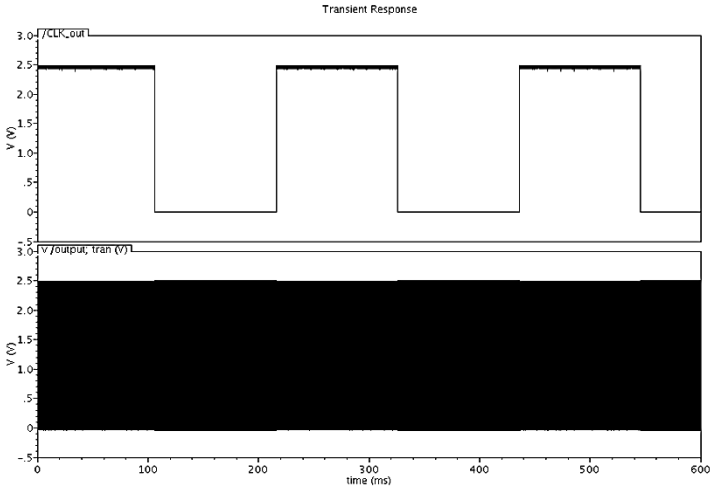

Figure 4.6 The results of the post-layout simulation for the CLK (top) and output (bottom). Due to the significantly different oscillation periods, the modulated signal has a massive output.

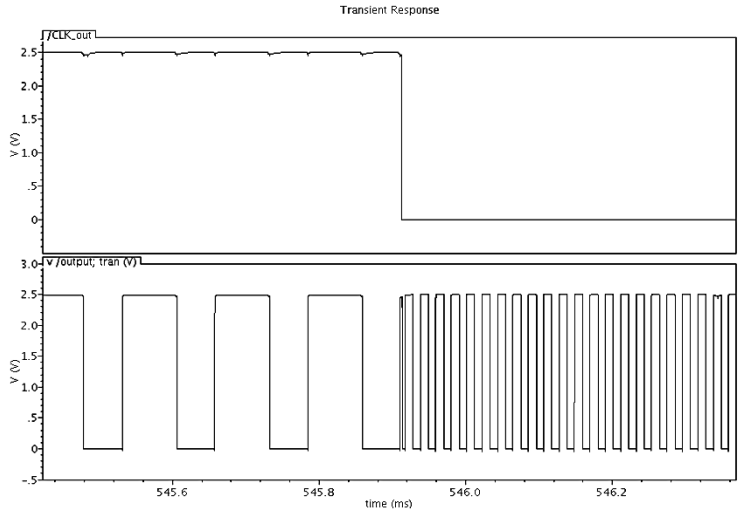

Figure 4.7 The results from Figure 4.6 are pinpointed at 545.9 ms, where a status change on the CLK (top) occurs. The VCO gets the power and engages into sensing as the CLK changes its status from ON to OFF. The modulated signal (bottom) shows the both outputs from the two oscillators.

The oscillating frequencies of the VCO and relaxation oscillators are residing inside the 100 kHz. These frequencies are extremely fast when compared to the 5 Hz of the CLK. When a simulation of transient response is extended as long as 600 ms as shown in the Figure 4.6, the output of the modulated signal is very massive as it appears as a black block. At the CLK of 545.9 ms, the view is pinpointed as shown in Figure 4.7. The two frequencies from the two oscillators are apparently distinguished (bottom). As the CLK (bottom) is ON, the relaxation oscillator is ON and generating an oscillation. When the CLK is OFF, the VCO receives the VDD, and it is in operation. Therefore, the second half of the output, therefore, signal is from the VCO.

The corner analysis was run for the post-layout. The current consumptions were purely from the core excluding the ESD's. The most significant requirement is to prevent overlap between the two outputs, eliminating faulty outputs. The upper boundary of the output from the relaxation oscillator is when the input is short. The lower boundary of the output from the VCO is when the input is -0.4, which is the lowest voltage made from the pH sensor. As long as the two outputs are not overlapping, the modulated signal will be properly interpreted. As the results shown in the Table 4.2 indicate, the frequency gaps between two outputs were 7.37, 7.87, 3.73, 14.54, 9.98 kHz. They were verified to be free of signal overlapping errors.

Table 4.2 The results of the corner analysis for the post-layout simulation

VCO (at nominal 2.25 V)				
Corner	Current (μA)	CLK (ms)	Relax. Osc (kHz)	VCO (kHz)
TT	30.35	183.07	18.63	26.00
FF	18.13	186.82	18.03	25.90
FS	18.32	198.73	19.37	23.10
SF	31.86	178.47	13.56	28.10
SS	29.50	175.52	16.32	26.30

4.4 Fabricated Chips

The layout circuit we designed was submitted through a fabrication service, MOSIS, and the fabrication was carried out by the foundry of C5N process, On Semiconductor. A fabricated chip has been wire-bonded in a package as shown in Figure 4.8. The detailed information about the package is found in Chapter 4.5. The wire-bonded pads were for “output”, “output_relax”, “gnd”, “CP_in”, “VDD”, “VDD_out”, “VDD_in”, “VCO_N”, “VCO_P”, “gnd”, “Imp_sensor_2”, “Imp_sensor_1”, and “VDD_relax” (clockwise starting from top left).

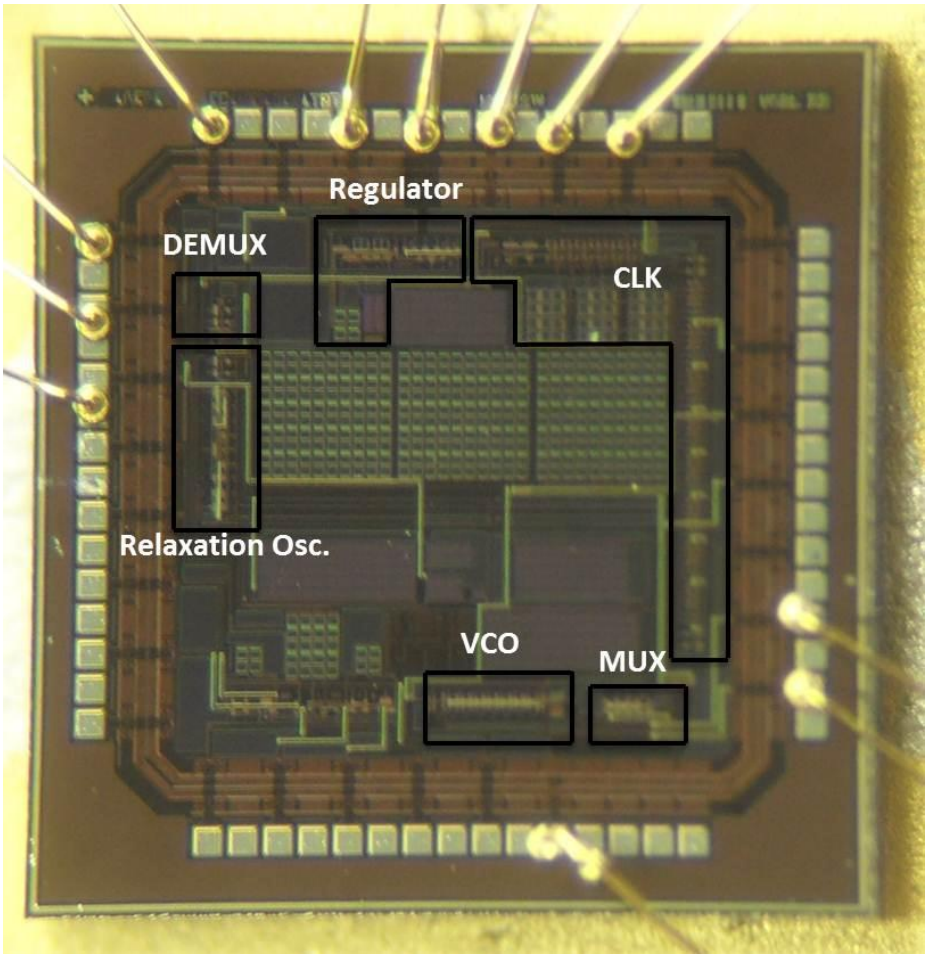

Figure 4.8 Photo of the fabricated chip

For more secure grounding, two grounding pads were prepared and located separated location. The pads of VDD, VDD_out, and VDD_in are for power supply for ESD’s, regulated voltage

from the regulator, and main power rail to all other modules inside the chip, respectively. These three pads are not connected (isolated). By connecting the VDD_out and VDD_in, the regulated voltage is going to support the whole chip excluding the ESD's. For operating the ESD's, all of these three pads can be externally shorted. This design allows us to more easily investigate or troubleshoot the chip when problems occur as an individual block can be separately handled from outside the chip.

4.5 Packaging

Packaging a chip is optional depending on circumstance. The foundry, On Semiconductor, provided forty dies fabricated by C5N technology. Five of them were wire-bonded by a third party packaging company, Sempac, INC.. The package we used is OCP_QFN_5x5_28a (model name from MOSIS) [62]. It is an open cavity plastic package. The package dimension is 5 mm^2 with inner space of 3.1 mm^2. It has 28 leads (pads). The detailed diagram of the package can be found in Appendix B [63]. Figure 4.9 shows the top and bottom view of the package. The package was capsulized by a lid after wire-bonding.

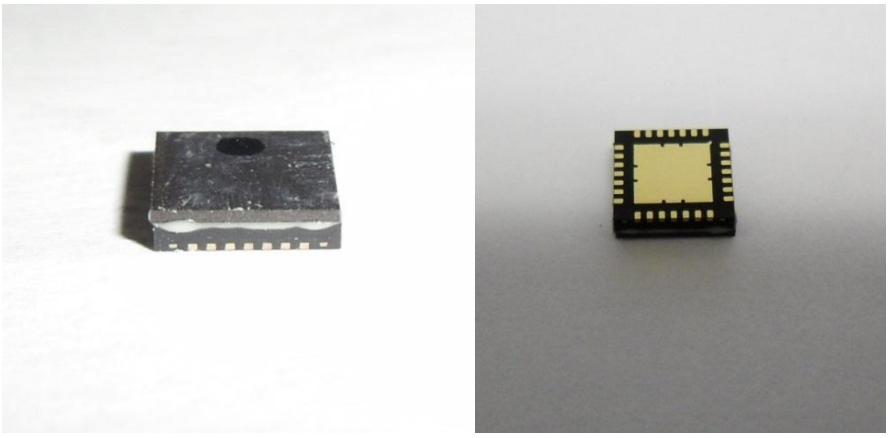

(a) (b)

Figure 4.9 The open cavity package of QFN28 (5×5 mm). Capsulized with a lid (a) and bottom view (b).

CHAPTER 5

BENCHTOP EXPERIMENTS AND RESULTS

5.1 Benchtop Setup and Tests

A packaged chip was soldered on a PCB for benchtop tests using a breadboard. The chip on a PCB is shown in Figure 5.1.

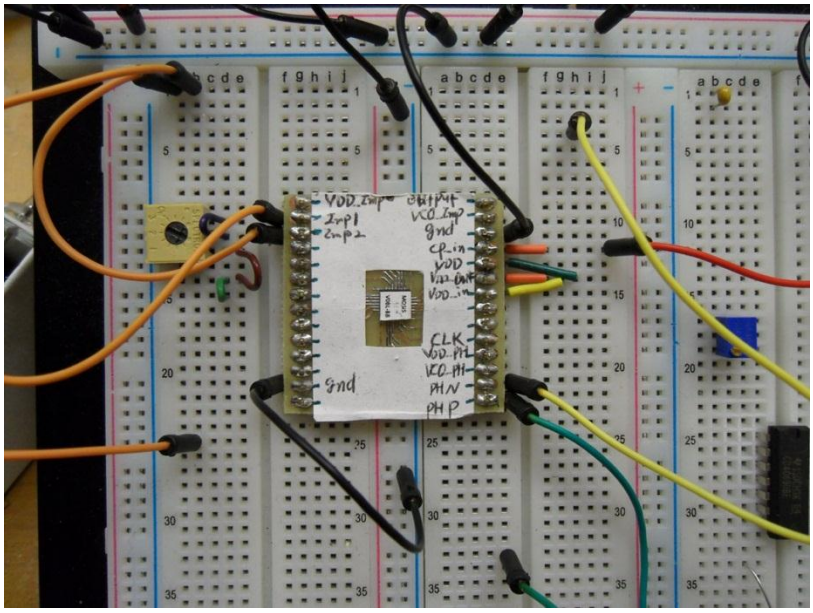

Figure 5.1. A chip on a PCB for benchtop tests.

Another method was carried out using a socket as in Figure 5.2. This socket was specially made for the QFN28 package we used. A packaged chip could directly be seated inside the socket. Each pad (lead) was internally connected to test pins located top of the PCB. A total of 28 pins were individually designated for each pad in the socket.

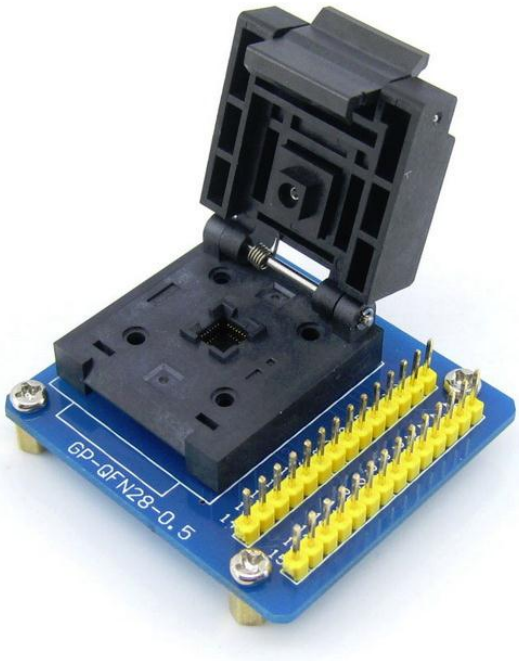

Figure 5.2 A socket for the package of QFN28 (5x5) [64]

5.2 Data Acquisition for the Experiments

A LabVIEW (National Instruments) was developed for data acquisition (Figure 5.3, 5.4). A USB-6210, data acquisition card (National Instruments), was used together. Three channels were programmed for two outputs of each oscillator and modulated signal. A sampling rate of 80 ks/s was assigned for each channel.

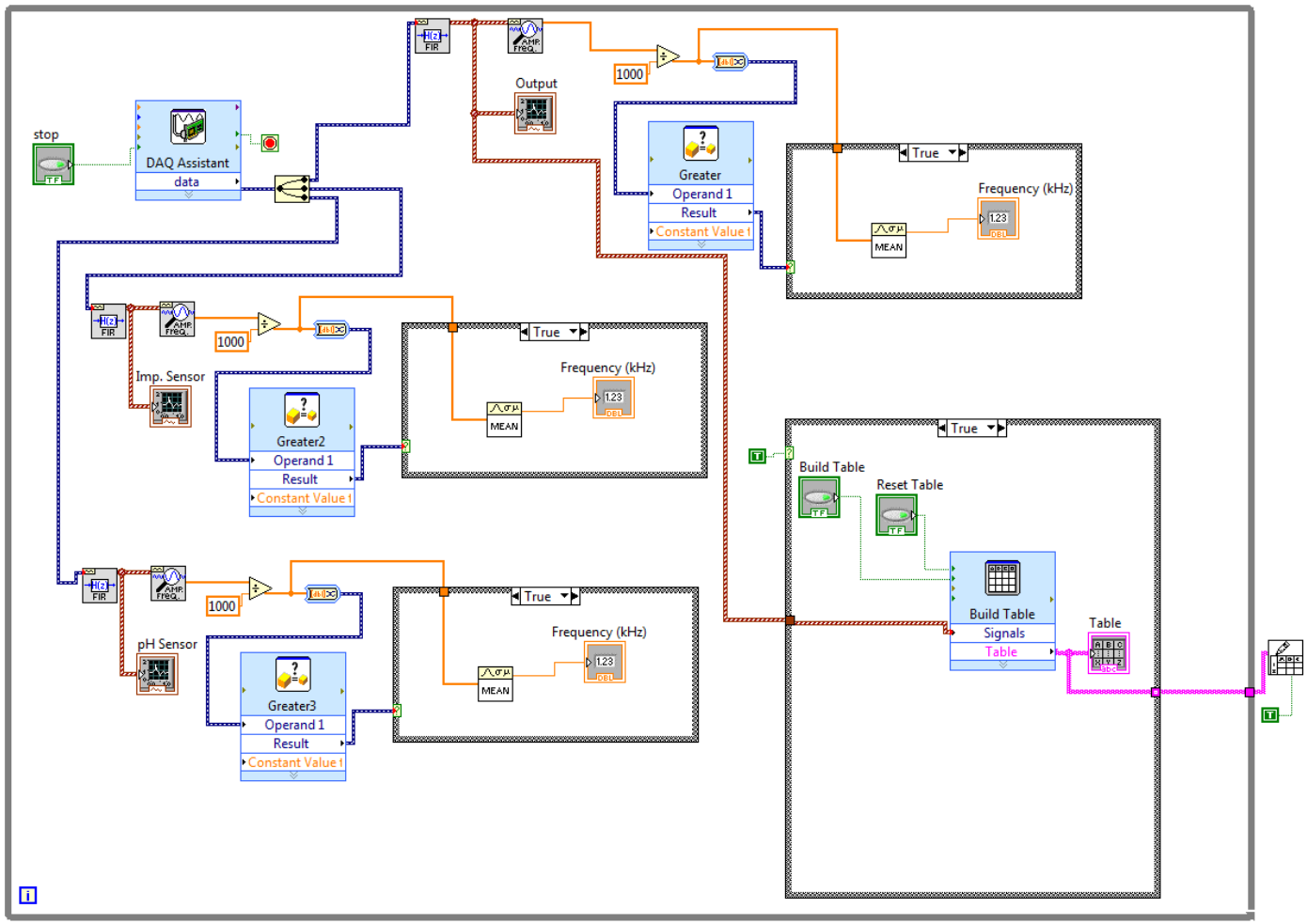

Figure 5.3 LabVIEW code used with USB-6210 for data acquisition

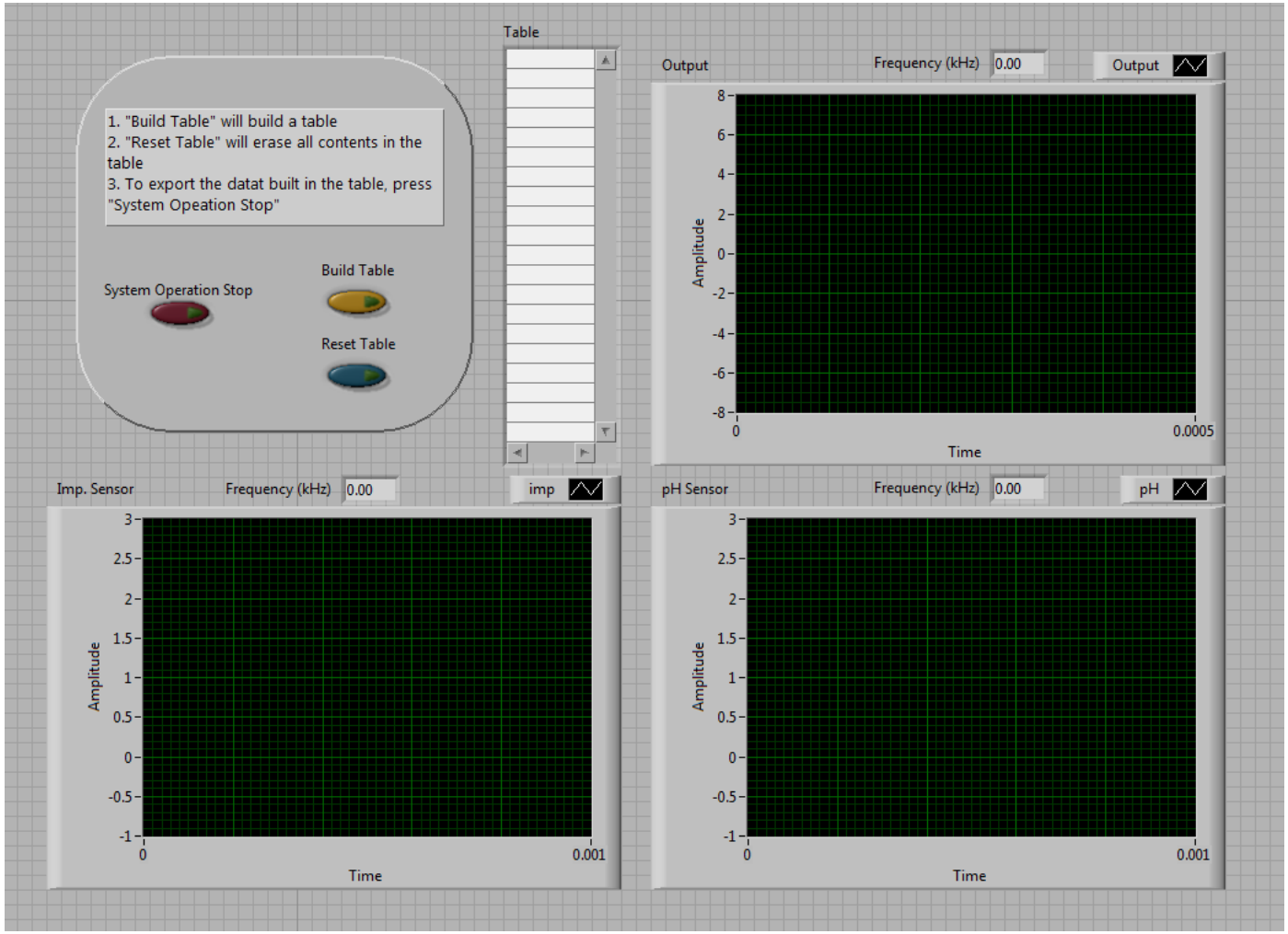

Figure 5.4 Graphical user interface (GUI) programmed from LabVIEW

5.3 Single Chip Test

5.3.1 Regulator Test

The chip on a PCB as shown in Figure 5.1 was tested for its performance including the regulated voltage, CLK, and the frequency spans against variations of input parameters. Firstly, the regulator was tested. For a versatile debugging, the pad of VDD_out form the regulator was not internally connected to other modules in our design. It could be connected from the outside chip. By this design, it was straightforward to test its output on the regulator. An external power supply was fed into the chip through the pad of CP_in. It was swept from 2 V to 10 V. Then, the VDD_out was measured. The output voltage of the regulator varied from 1.95 V to 2.24 V. It differed in 0.29 V. However, the regulator began to settle down at around 2.1 V when the input voltage reached at 2.3 V. The steady regulation continued until the input of 7 V. Despite the little increment beyond the input of 7 V, the total variation range was within the operating boundary (Figure 5.5). Likewise, the function of regulating the voltage was observed working properly.

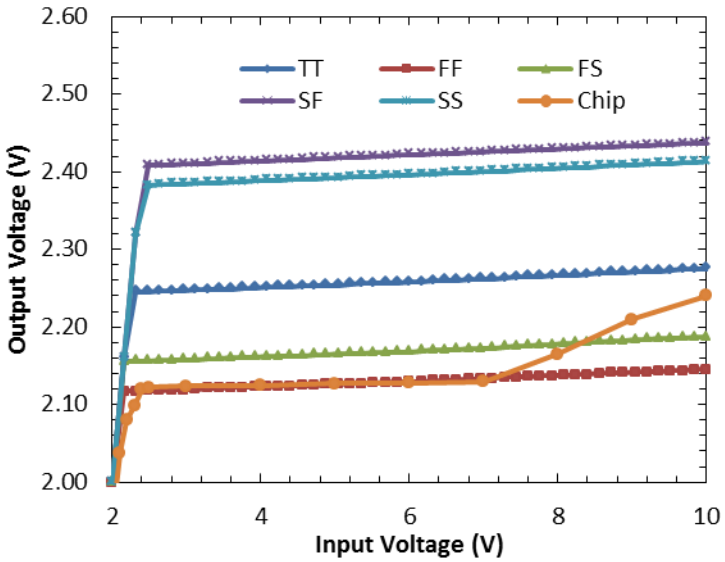

Figure 5.5 The regulator outputs for the input sweep. The CP_in was swept from 2 V to 10 V. The results are compared to corner analysis from post-layout simulation. The output of the tested chip is residing within the corner boundaries.

5.3.2 CLK Test

The regulator output was connected to the rest of the module. The operating voltage for the chip was 2.1 V, the regulated voltage. The CP_in was swept from 2 V to 10 V in the same manner in *5.3.1*. The CLK characteristic is shown in Figure 5.6. As the regulated voltage mostly stayed at 2.1 V, the CLK maintained its period at 180 ms. The corner analysis of the post-layout for the CLK was run with the regulated voltage of 2.1 V. The result was compared in Table 5.1. The CLK performed within the boundaries of the corner analysis.

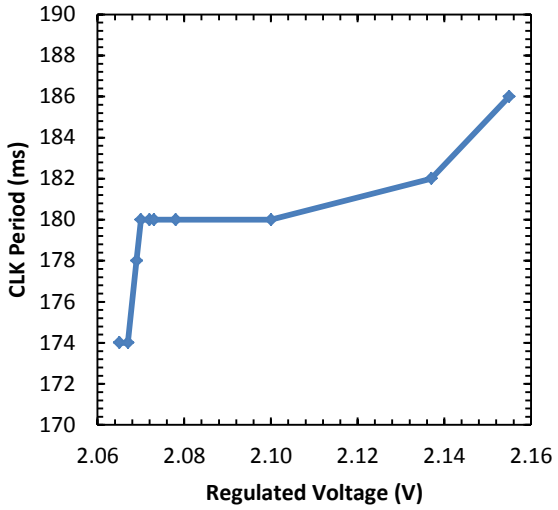

Figure 5.6 The result of the CLK test. The CLK mostly sustained its period at 180 ms for the change of the regulated voltage

Table 5.1 The CLK operated at 2.1 V is compared to all corners.

CLK (at 2.1 V)		
Corner	Period (ms)	Duty Cycle (%)
TT	167.48	50
FF	172.22	50
FS	189.30	50
SF	163.76	50
SS	160.77	50
Chip	180.00	51.1

5.3.3 Tests for the VCO

Similarly to *5.3.2*, the regulator was still supporting the operation voltage to the modules in the chip. Initially, the VCO was tested for its performance. A DC source was connected to the two inputs of the VCO; pH_sensor_N and pH_sensor_P. The DC input was swept from -0.4 V to 0.7 V. The output frequency of the VCO was acquired and measured from the LabVIEW program we introduced in *5.2*. The results shown in Figure 5.7 described the linear increment as shown in Chapter 3.

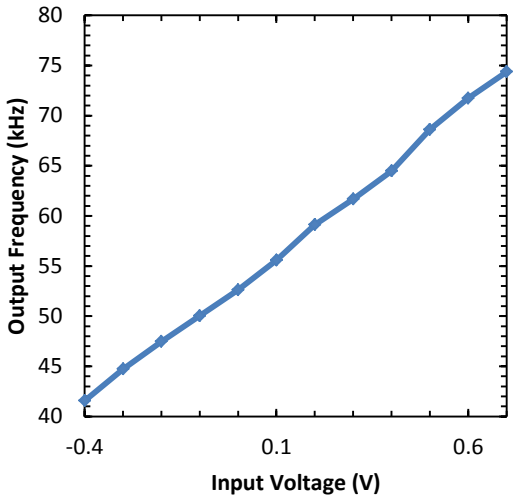

Figure 5.7 The result of the VCO. The output frequency spans from 41.55 kHz to 74.37 kHz for the input variation from -0.4 V to 0.7 V.

Due to the series connection between the pH_sensor_N and the voltage divider, the polarity of the voltage source (the input) was important. The direct proportion was achieved in Figure 5.7. However, indirect proportion could be achieved when the input voltage source was reversed. A sensor that generated potentials should consider its connection (polarity) to the VCO. There should be no difference in the frequency span despite of the polarity change. Nonetheless, users should keep it mind that the change of polarity can alter the change of direct or indirect increments of the output.

5.3.4 Tests for the Relaxation Oscillator

The same setup for *5.3.2* was applied. However, a sweep of resistance was used on the two inputs of the relaxation oscillator. From an open circuit to 1 MΩ was connected to Imp_sensor_1 and Imp_sensor_2. The results are shown in Figure 5.8.

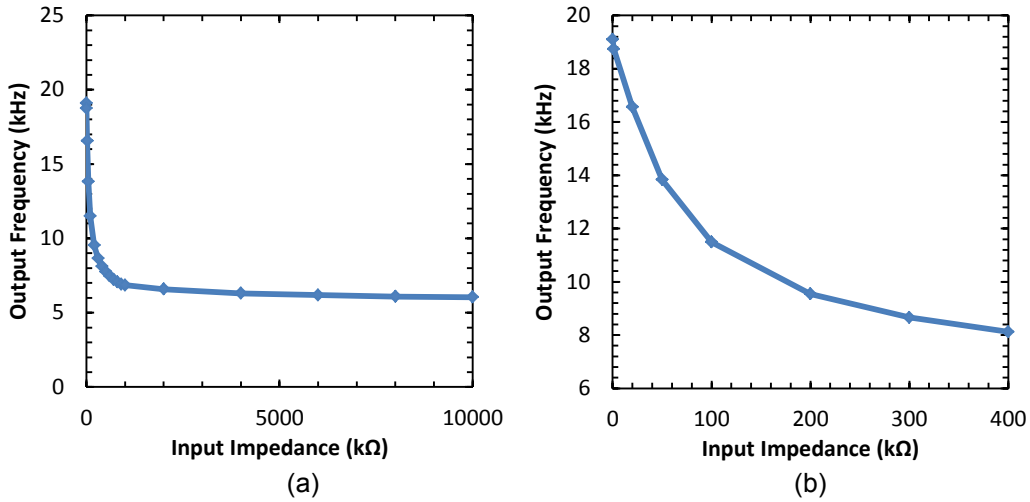

Figure 5.8 The results of the relaxation oscillator. The resistive input was swept from zero to 1-MΩ (a) and a close look (b)

The output frequencies were measure at 19 kHz and 6.0 kHz for the input of zero and 1 MΩ, respectively. The upper boundary was matched with TT and FF corners. On the other hand, the lower boundary was at least 2 kHz below the lowest boundary that was simulated at SF. Despite of the "off-boundary" result, the frequency expansion to the lower number did not interfere with the data acquisition. The resolution became even higher than the simulation results.

5.3.5 1st Chip vs. 2nd Chip

Based on the experiments in *5.3.2,* it was observed that the regulator performed properly even though the operating point was as low as 2.1 V. Therefore, another experiment was carried out using the regulator. Two chips were compared in their performance. The same experimental setup as *5.3.2* was prepared. The results are shown in Figure 5.9 (a-c). The differences between two chips were very minimal.

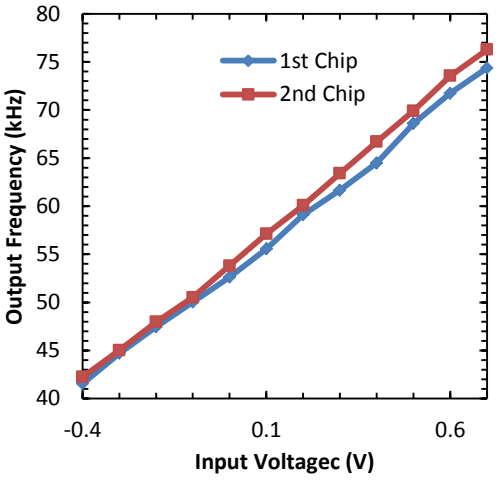

(a)

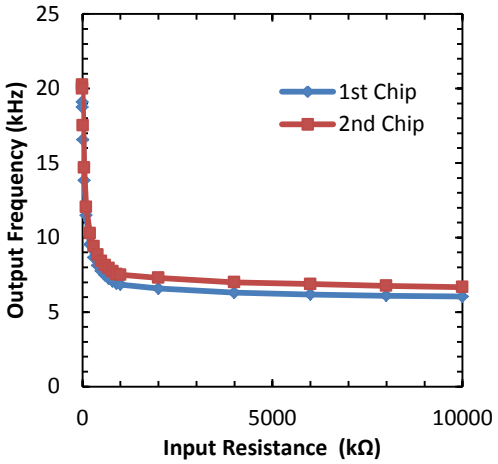

(b)

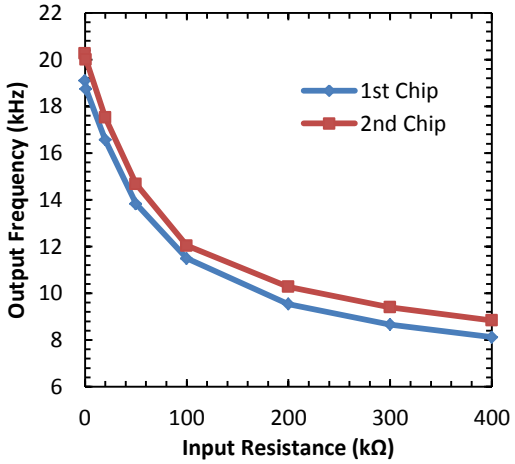

(c)

Figure 5.9 The comparison of performance by chips. The results of VCO (a), relaxation oscillator (b), and a close look of (b) (c).

5.3.6 Capacitance Input

The next experiment was performed to measure the output of the relaxation oscillator for capacitive inputs. Most capacitive sensor has its own initial capacitance. The initial capacitance varies depending on shape, dimensions, material, and more. It is hard to judge what initial value we needed to use for the benchtop test.

Our group has fabricated a few different types of capacitive sensors including an IDC sensor. An average initial capacitance for the IDC sensors is around 10 pF. Therefore, a capacitor of 10 pF was connected to the inputs of the relaxation oscillator. For a capacitive increment, a capacitor of 0.25 pF was added in paralle to the initial capacitor. The increment was carried out until total variation of 1 pF was made. The Figure 5.10 shows the results for total of 1 pF increment.

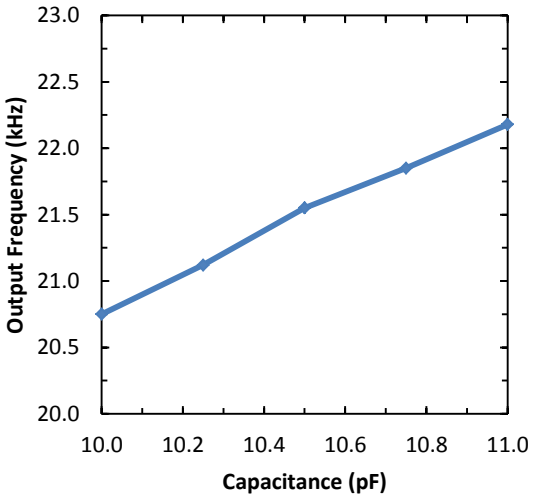

Figure 5.10 The output frequency span versus capacitive inputs.

Total of 1.43 kHz was varied for the input variation of 1 pF. The output resolution for different inputs was clear. Hence, our universal platform has been proved for capacitive inputs as well.

CHAPTER 6

WIRELESS POWER TRANSFER & WIRELESS COMMUNICATION METHOD

A wireless system plays an important role in clinical diagnosis and treatment application because it increases comfort and mobility of patients. A batteryless implant is an attractive option as it eliminates the needs for repeated surgeries to replace the battery after implantation. For example, the currently available GERD detector is large in size due to the battery, which needs to be replaced every 2 days via a 2–4 hour long surgery. It is agonizing for patients with GERD to undergo such procedures. Thus a miniature implant , without the need for battery, that can be implanted through endoscopy, is preferred for the welfare of the patients.

Compared to the different methodologies of energy harvesting mechanisms used to power up implants such as piezoelectric, thermoelectric, or ultrasound; inductive coupling provides merits of higher power transfer and reliable control. The power received could be in the milli-watt ranges with a reasonable distance while the transmission could be electronically controlled. Inductive coupling for medical devices has long been studied [65][66][67]. However, most of them are for uses at sub-centimeter distances, such as in subcutaneous applications or at centimeter scale for low power sensor applications. The focus was on the power transfer efficiency while constraining the antenna sizes, for clinical practicality to perform endoscopic implantation through the oral tract and for patient's comfort to wear a small electronic module for RF power transmission through tissues without tissue heating. In order to provide sufficient wireless power to the implant, we studied the energy scavenging efficiency in air targeting a distance of 4 to 9cm, from previous experience that the loss through similar tissue thickness was about 50%. The system also included a class-E amplifier and resistive load. The constraining factors included the small sizes of coil antennas and limited transmission RF power. The goal is to achieve optimal power transfer efficiency.

6.1 The System Configuration

The circuit diagram of the inductive coupling system is illustrated in Figure 6.1. The input signal was a square wave with 6 V_{pp} amplified by a class-E amplifier at 1.3 MHz.

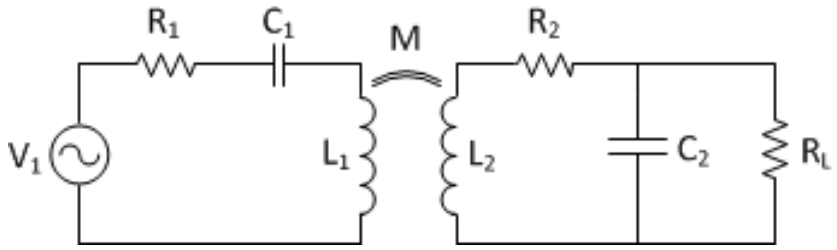

Figure 6.1 Circuit diagram of the wireless power transmission system

The primary coil of transmitter and the secondary coil of implant antennas were center aligned and faced each other. Thus they could be modeled with an equivalent transformer. The antenna coils were represented by L_1 and L_2 while C_1 and C_2 tuned the resonance at 1.3 MHz. Coil resistances were R_1 and R_2. The load R_L was assumed to be resistive.

The power transfer efficiency of the system could be expressed as P_{out} / P_{in}, where P_{out} is the power at the load resistor, and the P_{in} is the supplied power on the transmitter side. The efficiency for the system could be derived according to Eq.6.1-2 [68].

$$\text{eff} = \frac{A}{\frac{R_1}{\omega^2 M^2}[(R_2+A)^2+(\omega L_2 - A R_L \omega C_2)^2]+R_2+A} \tag{6.1}$$

where

$$A = \frac{R_L}{R_L^2 \omega^2 C_2^2 + 1} \tag{6.2}$$

6.2 Antenna Design

In our animal experiments[69], the implant cross section determined the coil antenna dimensions as 1×3.5 cm^2 as shown in Figure 6.2 since the metal wire was wrapped around the rectangular-shape printed circuit board to maximize its aperture size. The coil wire connected to a tuning capacitor, followed by a voltage multiplier and voltage regulator. It should be noted that the turn number of the coil antenna and the metal wire gauge were limited in order to limit the thickness of the package so that the implant could be delivered through an endoscope. We chose AGW-26 wire with a tradeoff between unit-length resistance and wire thickness. 13 turns of wire were wrapped around the circuit board making it 2 mm in thickness and producing an inductance of 10 μH. The transmitter antenna was made of AWG-26 copper wires with various radii from 4 cm to 6 cm and various coil turn numbers. Previous experiments [70] showed that the 5-cm radius antenna, in general consumed a lower input current, had a smaller physical size so it would be more comfortable to wear, and had a lower inductance so the matching capacitance would be sufficiently large to tolerate parasitic capacitance in the environment preventing the resonance frequency from shifting. The antennas were made with a consistent tensile strength applied to the wires when wrapping the coil.

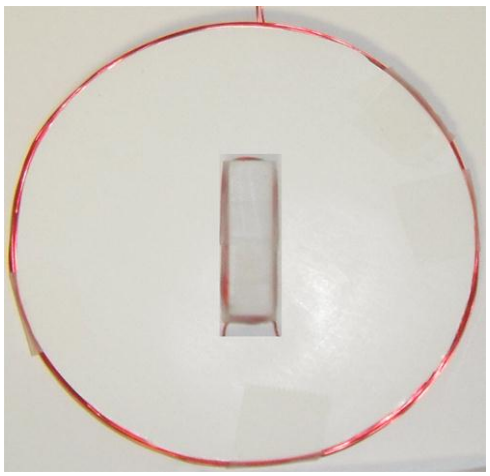

Figure 6.2 An actual photo image of a reader antenna and the tag antenna. The reader antenna is in 5-cm radius with 17-turns, and the tag antenna is in 1×3.5 cm^2 with 13-turns.

To keep the tuning capacitance small in order to maintain the small size of the implant circuit board, L_2 was chosen to be 11.05 μH with C_2 of 1356 pF for the resonant frequency at 1.3 MHz. This resulted in an implant coil of 13 turns and coil resistance of 3.5 Ω. With fixed parameters in the implant, the primary coil resistance R_1 and mutual inductance M thus determined the transfer efficiency. The mutual inductance was determined by

$$M = k\sqrt{L_1 L_2} \tag{6.3}$$

and the coupling coefficient *k* was determined by the coil antenna shapes, sizes, and distances between the coils.

With a fixed implant coil antenna, L_2 is fixed and *M* would vary with L_1. Hence, we investigated transfer efficiency by changing the dimension and turn numbers of the primary coil.

Since the electronic circuitry and Li-ion battery packs are fairly small, the transmitter antenna dimension determines the size of the wearable module. We limited the dimension of the primary coil within 6 cm in radius for comfort of patients with chronic issues. In addition, the resonant capacitance C_1 fell below 100 pF when the total length of the primary coil was beyond 700 cm, which represented a coil turn of 18 with a radius of 6 cm. As the resonant capacitance grew smaller, it became difficult to fine-tune the circuit to reach a maximum efficiency due to the increased effects of parasitic capacitances. The maximum number of coil turns was thus set at 18 due to this constraint. Preliminary results also indicated that the coupling coefficient, *k*, dropped below 0.02 when the radius was 3 cm or smaller due to the large divergence of magnetic field lines between the primary and secondary coil antennas. Thus, the minimum radius was set at 4 cm.

6.3 Experimental Setup

The coils were wound identically on frames with various radii to minimize the parasitic effects of capacitances between the metal wires. The coils were wound around a center with parallel windings along a vertical plane with precise spacing. Figure 6.3 illustrates the configuration of the coils.

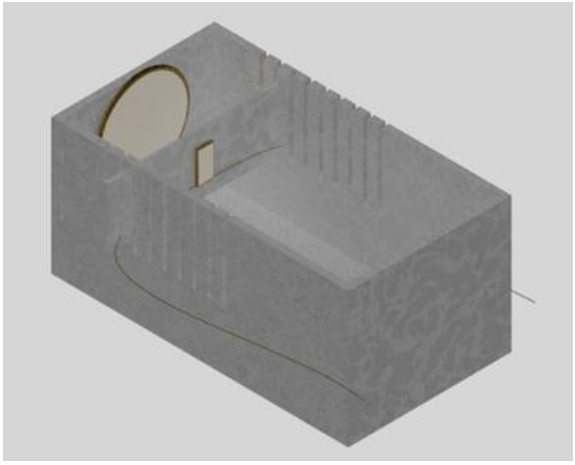

Figure 6.3 Illustrated experimental setup for the antenna separation. A primary coil is attached on the fixed target board. The tag coil is residing on the slot-board that will be moved into each slot. The distance between the two antennas can be controlled precisely in the setup.

The mutual inductance was measured with the open-short method for each transmitter and implant coil pairs [71]. An n-channel power MOSFET (Fairchild, IRF510) was used in the class-E amplifier to amplify the 1.3 MHz carrier signal fed by a function generator with 6 V_{pp} pulse signal with a 50% duty cycle. Output voltage was measured on the load resistor for output power while input voltage and current were measured to obtain input power. The overall power transfer efficiency obtained from the experiments included the class-E amplifier efficiency. A method of measuring LO to HI gate drive transition was used to obtain the efficiency of the class-E amplifier. The transition time for the drain current in the linear region from zero to saturation was measured and compared to the carrier frequency of 1.3 MHz. Phase delay was calculated and converted to the efficiency of the amplifier. The efficiency was measured to be approximately 90% for all the experiments.

6.4 Experimental Results

6.4.1 Input & Output Power and Efficiency

The Voltages on the load resistor of 500 Ω in the implant module and the input DC currents drawn by the class-E amplifier are shown in Figure 6.4. They were measured from three primary antennas with different radii of 4, 5, and 6 cm. The distance between the primary and implant modules was fixed at 4 cm. For a transmitter coil radius of 4 cm, a maximum power of 218 mW was achieved at 10 turns. Similarly, for coils of 5 cm and 6 cm, maximum powers of 215 mW and 172 mW were obtained at 11 and 10 turns, respectively. Taking the input power into account, maximum power transfer efficiencies of 6.57 %, 6.83 % and 6.18 % occurred at 17, 15, and 18 turns for coil radii of 4, 5, and 6 cm, respectively. Similar measurements were also conducted for various combinations of transmitter coil radii and distances between coils.

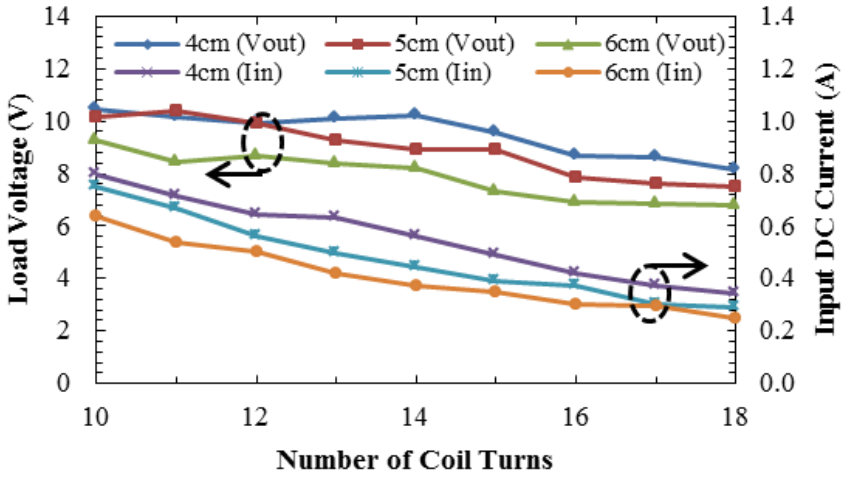

Figure 6.4 The load voltages and input currents versus the number of coil turns. The experiments were performed with R_L = 500 Ω on the implant module and 4-cm distance between two antennas.

The experimental results were compared to theoretical values calculated from measured component values. Figure 6.5 demonstrates the efficiency when the load resistance was varied. Figure 6.6 shows the efficiency variation as a function of the distance. These

measurements were conducted with a transmitter coil of 17 turns, because of the relatively low power consumption and higher efficiency, to demonstrate the results.

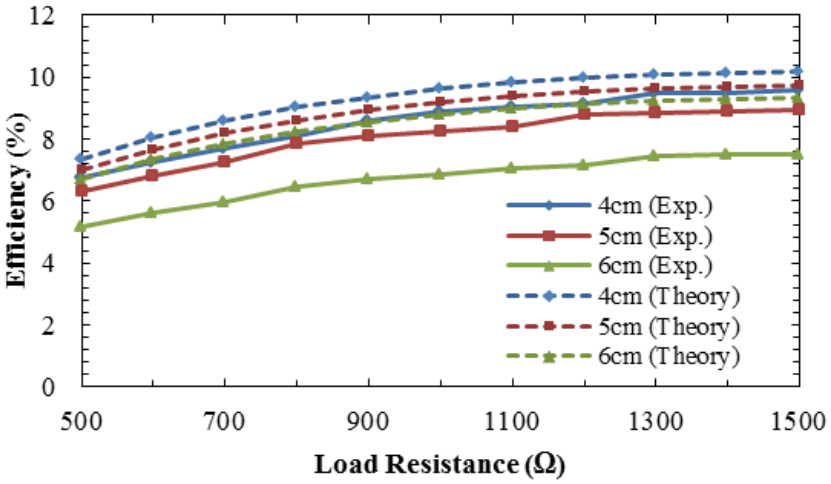

Figure 6.5 The efficiencies of power transfer versus the load resistances. The 17-turns transmitter coil antennas in the radii of 4, 5, and 6 cm were used. The experimental results were compared with theory.

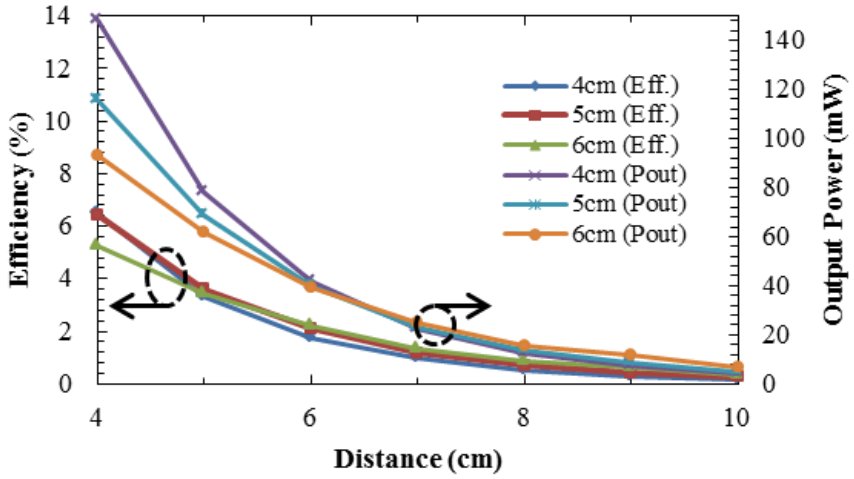

Figure 6.6 Transferred power and power efficiencies versus distance. The antenna separation was varied from 4 cm to 10 cm. The 17-turns antennas in the radii of 4, 5, and 6 cm were used. The load resistance was set at 500 Ω.

In Figure 6.5, the experimental results generally match the trends of the theory. Between 500 to 1500 Ω, which is the impedance range of the stomach tissues, the lowest measured efficiency was 5.16 % for the case of the antenna radius of 6 cm and a load of R_L=500 Ω. The highest efficiency was measured at 9.59 % for the case of a 4-cm radius antenna with a load of 1500 Ω. With coil radii of 4, 5, and 6 cm, the measured efficiencies were in the ranges of 6.74–9.59 %, 6.30–8.94 %, 5.16–7.52 % for tissue impedance changes between 500 to 1500 Ω.

In Figure 6.6, the distance between two antennas at 10 cm, the received power was at least 3 mW for all three transmitter radii of 4, 5, and 6 cm. The measured powers on the 500-Ω load at 10 cm were 4.15, 5.12, and 6.70 mW for coil radii of 4, 5, and 6 cm, respectively.

6.4.2 Matching Capacitance

In comparison among the higher turn numbers of coils, another practical parameter we considered was the parasitic effect. As the turn number of coil increased, the self-inductance increased resulting in a smaller matching capacitance (226 pF and 121 pF for 14 and 18 turns), as shown in Figure 6.7

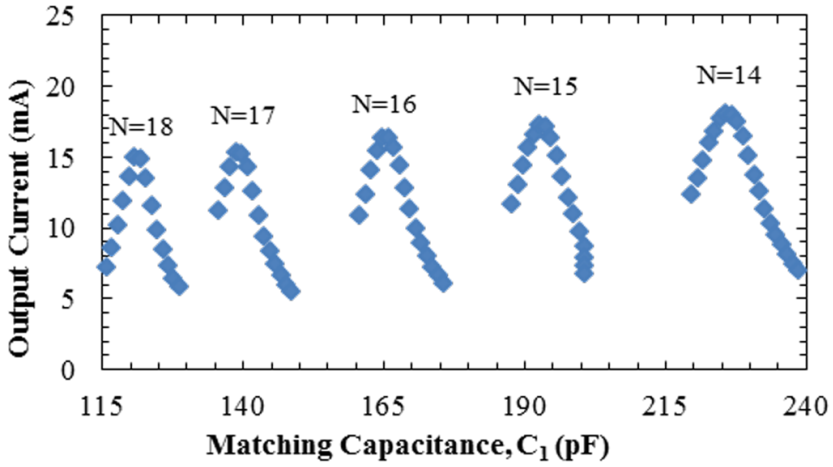

Figure 6.7 Output current at R_L=500 Ω. The matching capacitance decreases due to the increasing self-inductance as the number of turns increases. Less matching capacitance meaning the system is more vulnerable to parasitic effects from the surrounding environment

It makes the circuit more susceptible to parasitic effects from environmental changes. For example, the effective dielectric constant near the coil wires varied when the transmitter coil antenna was firmly conformed on the pig abdomen skin indicated by the resonant frequency shift and the consequential change of efficiency. Therefore, since the 17 and 18-turn coils generated similar efficiency and transferred power, a coil with fewer turns was preferred.

6.4.3 Tissue Effects

In accordance to feasibility test with GERD, our previous work during the in vivo animal experiments [72] showed that the pig abdominal wall was estimated to be 3 cm in thickness. By comparing the received current at a distance of 3 cm in air, the attenuation of RF energy in the 3-cm thick tissue reduced the amount of stimulation current to 77 %, from 2.93 mA to 2.26 mA, and to 76 %, from 6.56 mA to 5 mA, for two different input power settings. In this work, we used saline to mimic the tissue attenuation effect. The 17-turn coil was placed at a 4-cm distance from the implant coil. A bag of 0.4 % solution of NaCl was placed between the coils. The transferred power and efficiency were compared between air and saline as shown in Figure 6.8

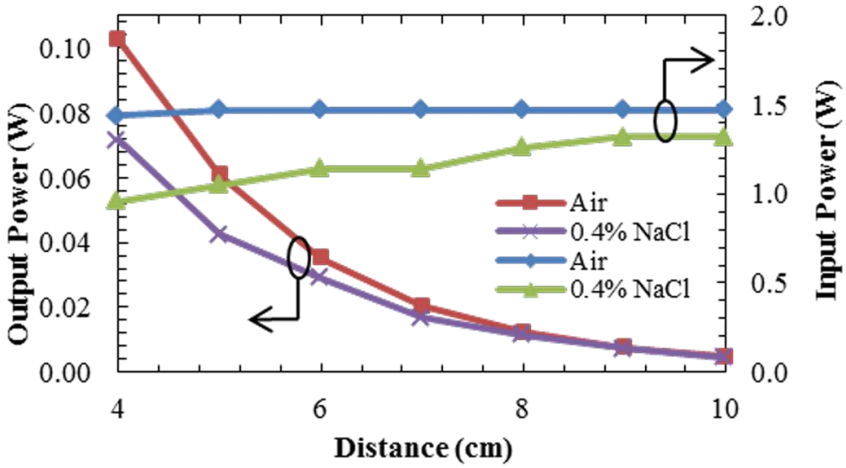

Figure 6.8 Input and output powers for different media, air and 0.4 % NaCl solution, at various distances between two antennas. The radius of 5 cm and 17-turn coil antenna was used.

At 4 cm, the loss of transferred power in the saline solution was about 30 % of the power transferred through the free space. The differences became smaller as the distance increased as expected since the transferred power decayed with distance in magnetic field coupling. It should be noted that the input power gradually increased with the distance. This is due to the effective dielectric constant variation from the water that changed the parasitic capacitance in the coil.

Nonetheless, the output currents obtained at the 10 cm distance were 3.05 mA through the free space, and 3.02 mA through the saline solution, which was above the required minimal electrical current of 1mA for another application; gastrostimulation.

6.5 Power & Efficiency Mapping

An apparatus was made as Figure 6.9 to perform accurate 3-D measurements for power and efficiency maps.

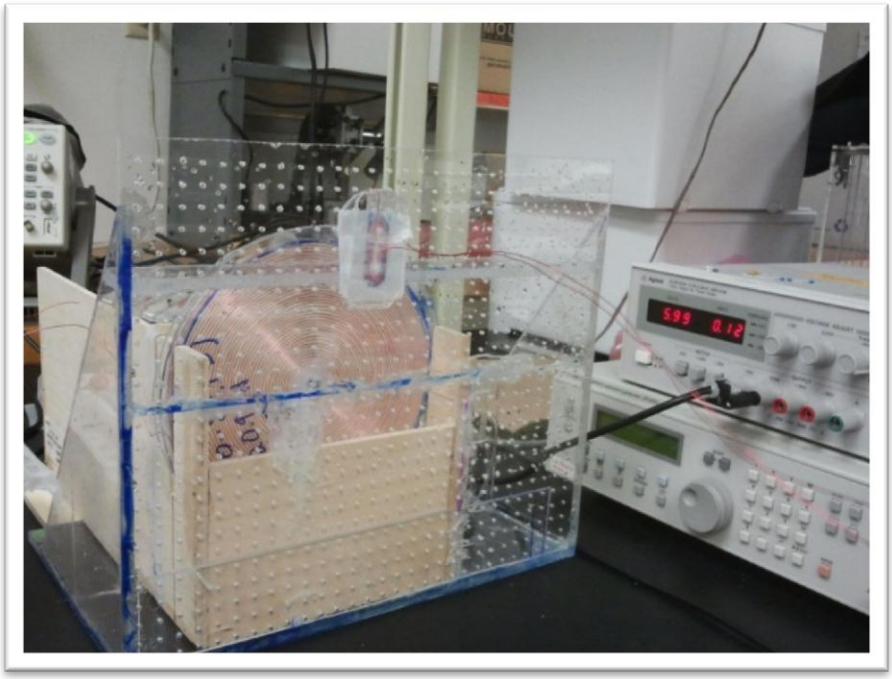

Figure 6.9 The apparatus for the mapping experiment. tag antenna can be attached in holes that are grids in 1 cm apart to horizontal and vertical lines. The distance apparatus can be used together to make a precise separation between the primary and tag antennas.

Various separation distances between the primary and tag antennas were assigned as (z), and horizontal and vertical alignments were (x and y respectively). From z=4 to 10 cm, slots were made 1 cm apart along a wooden rail to hold the transmitter antenna vertically, facing the implant antenna which was mounted on a large acrylic plate with alignment grids.

The centers of the transmitter and implant coils were aligned as (x=0, y=0) and the implant coil was allowed to move ±8 cm in both x and y directions. To avoid interferences, metal objects and equipment were kept at a sufficient distance from the measurement setup.

To map the voltage and efficiency distribution at different distances, the implant antenna was moved in x-, y- and z-direction. The results are shown in Figure 6.10 and 6.11. Both voltage and efficiency distributions were illustrated in absolute and normalized values. The normalized values were the data normalized to the maximum value at that antenna separation distance which occurred at the centers.

In both figures, it was clear that the output power and efficiency reached the maximum when two coil antennas were centered. However, these maps were to provide us information about the effects of antenna misalignment due to body and stomach motions. The average 3-dB (50%) power radii in each x-y plane were 3.7, 3.6, 3.75, 3.83, 4.15, 4.4 and 4.56 cm at the distances of 4, 5, 6, 7, 8, 9, 10 cm, respectively, for a transmitter antenna size of 5 cm and 17 turns. Because the 3-dB points did not follow a perfectly circular shape in the x-y plane, the radius was averaged over the distances from all 3-dB points to the center. Similarly, the efficiency maps also provided the average 50% efficiency drop points at 3.46, 3.42, 3.67, 3.85, 4.09, 4.43 and 4.57 cm from the centers at the distances of 4, 5, 6, 7, 8, 9, 10 cm, respectively. The 50% efficiency contours in each plane are shown in Fig. 8. At a 4-cm distance, the produced current at the center was 14.78 mA while it became 9.32 mA at a radius of 4cm. At a 10-cm distance, the produced current at the center was 3.34 mA while it became 2.52 mA at a radius of 4 cm. Although the measurements were conducted in air, the estimated load current and efficiency values could be extrapolated from the saline experiment.

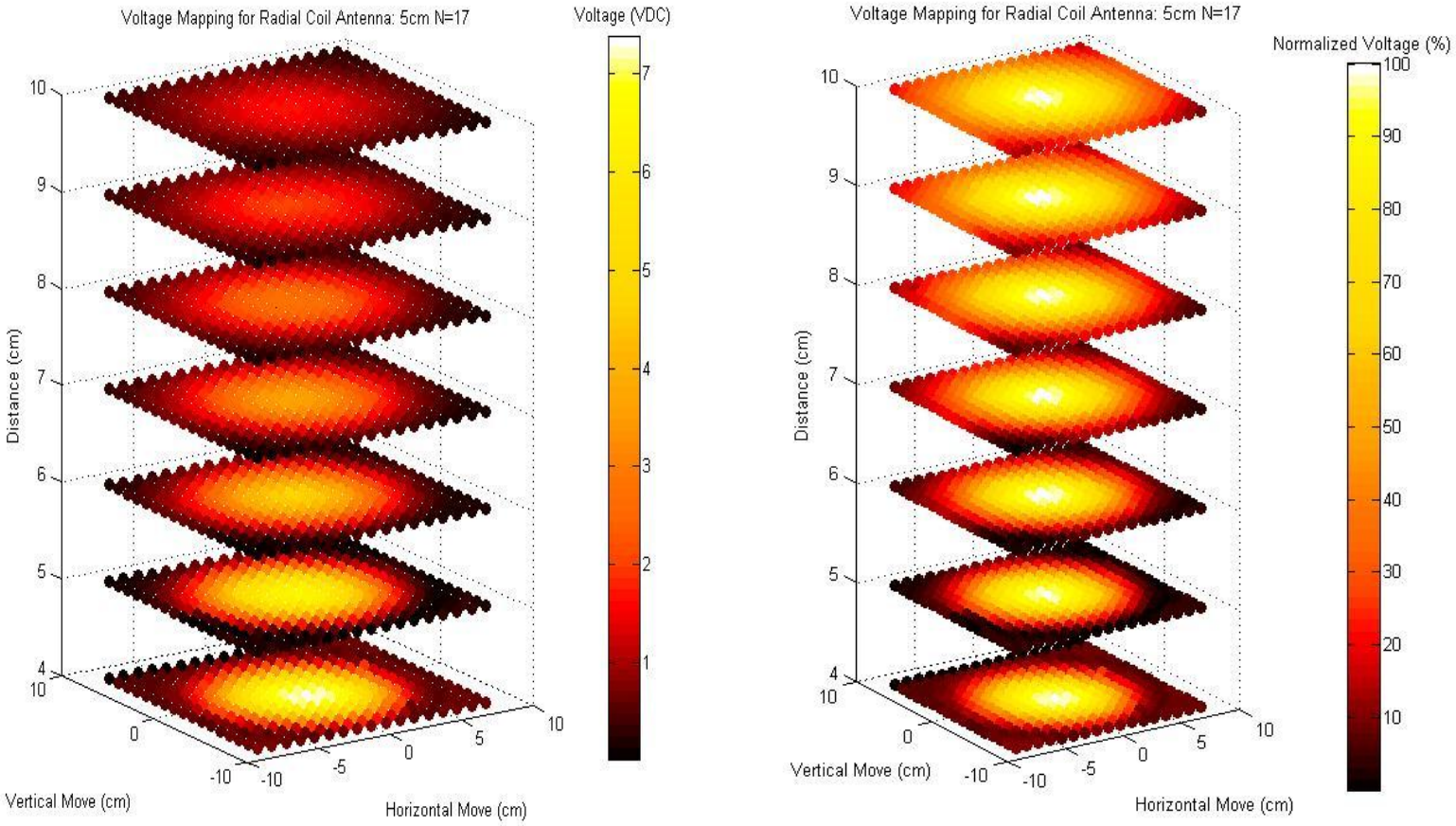

(a) (b)

Figure 6.10 The maps for the receiving voltage at the tag. The absolute values (a) describes how the intense of magnetic fields changes in z direction. The normalized values (b) depicts the divergence of the magnetic fields as z increases.

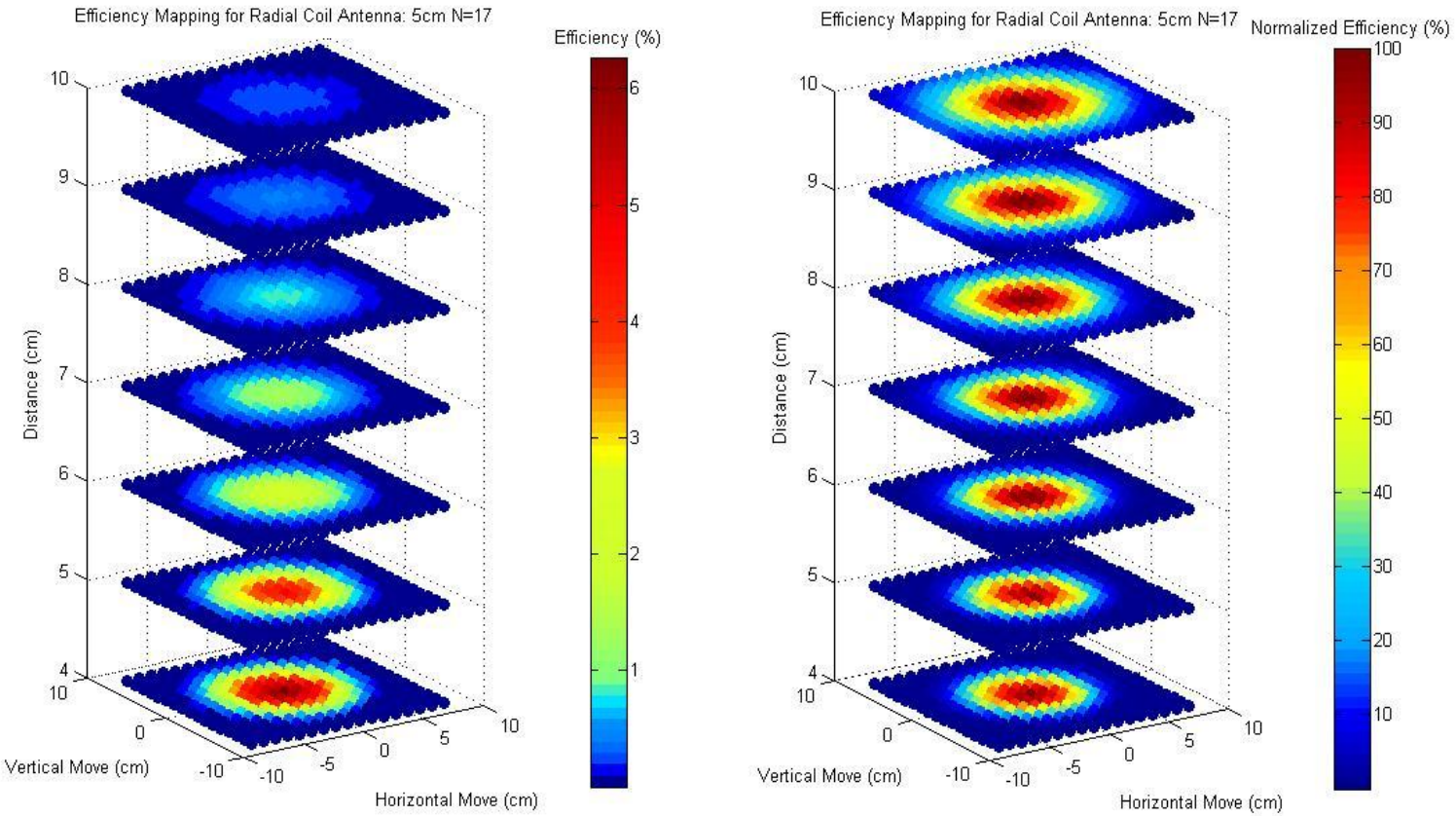

(a) (b)

Figure 6.11 The maps for the power efficiency in absolute values (a) and normalized values (b)

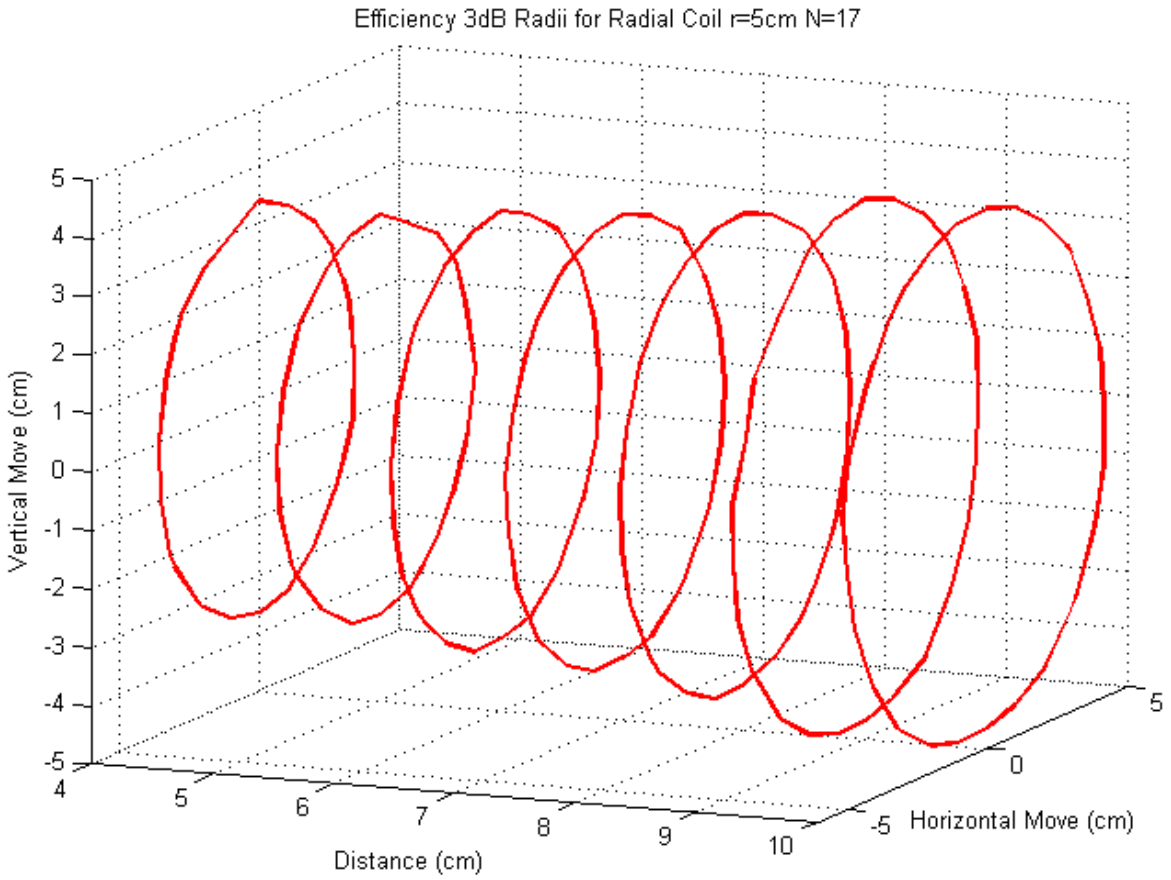

Figure 6.12 The contours of 50 % efficiency at different antenna separation distances.

6.6 Discussions

The feasibility of wireless power transfer via inductive coupling for implantable devices has been demonstrated by examining parameters such as number of coil turns, dimension of antenna, load variation and distance. It targeted to investigate the wireless power transfer issues in terms of output power and input power consumption as well as the transfer efficiency. A system with low power consumption and high efficiency can achieve endoscopically-implantable miniature batteryless/rechargeable wireless devices such as GERD detector and gastro stimulator operated by a wearable and portable reader. The transfer powers and efficiencies were examined at various distances between the antennas and with the effects of tissue attenuation mimicked by that of saline. The output voltage and efficiency maps were generated to examine the effects of the antenna misalignment. The acquired information will be used to guide the final system design for miniature batteryless wireless implantable devices.

The overall transfer efficiencies, which included the efficiencies of a class-E amplifier under different loading, were obtained experimentally. From a range of 500 to 1500 Ω as the impedance of stomach tissue varies, the minimal 3 mW of power were received via air at the antenna separation of 10 cm. This is three times higher than the minimally required power for gastro stimulators.

A small radius antenna drew more current than a large radius antenna did. For a portable transmitter, an antenna could draw less current and should be more suitable. However, a large size of antenna experienced less immunity against parasitic effects due to its high inductance. Under the two significant results, the radius of 5 cm was considered the most optimal size.

Among different number of coil turns, the 16 through 18 provided relatively high power transfer and low current consumption in contrast to the other turns. Therefore, we chose the 17-turn coil antenna for our next experiment in the next chapter.

CHAPTER 7

EXPERIMENTAL SETUP AND RESULTS FOR GERD APPLICATION VIA WIRELESS BATTERYLESS METHOD

7.1 PCB Design and Finalized Device

7.1.1 PCB Design and Layout

To implement a complete implant for GERD detection, discrete and passive components were needed including a charge pump. A PCB was designed to hold all of the components including the chip. The design was optimized to also integrate an impedance sensor, a pH sensor, and the tag coil antenna. The schematic of the PCB design is shown in Figure 7.1. A two-stage charge pump was implemented using Central Semiconductor's CMXSH2-4LS, a discrete component with embedded quad Schottky diodes. It provided forward voltage drop as low as 240 mV. The C_1, C_8, and C_{12} were employed for the voltage multiplier. The C_5 was needed for the matching circuit, and C_6 was for suppressing ripples. The C_7 was used with U_1 to compose the load modulator. Fairchild's FDV301N was used for the U_1. The gate of U_1 was connected to and switched by the output of the chip. This transmitted the output of the chip back to the reader by means of load modulation. This switching transistor modulated the impedance of the chip seen by the matching reader circuit. The corresponding change in the reader antenna voltage amplitude was interpreted as a frequency signal representing the modulated sensing signal.

The impedance sensor P_2 was connected to the capacitors of C_2 and C_3 on each electrode side due to the pH sensor's DC voltage flow. If the DC component of the voltage is fed into the feedback of the relaxation oscillator, it will immediately terminate the oscillation. Therefore, C_2 and C_3 are used to filter out the DC input from the pH sensor.

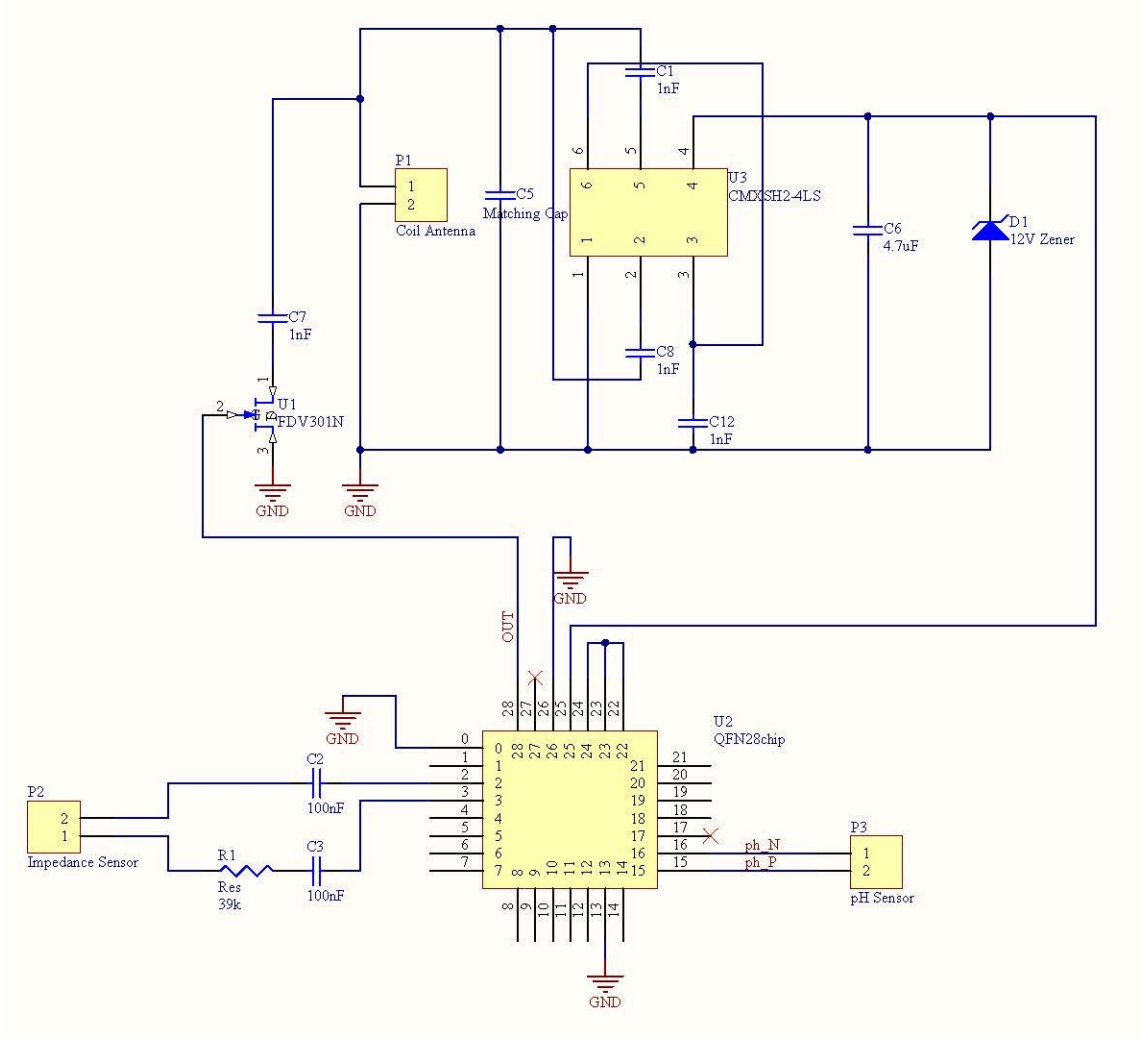

Figure 7.1 Schematic of the PCB design for GERD detector

A corresponding PCB layout is displayed in Figure 7.2. Two pins for the coil antenna are located on the middle top in (a). In the same figure, pads for the impedance sensor are laid on the bottom left, and the pH sensor is on the bottom right. A two-layer PCB design was applied. The outer dimension of the PCB was measured at 0.9 × 1.6 cm^2.

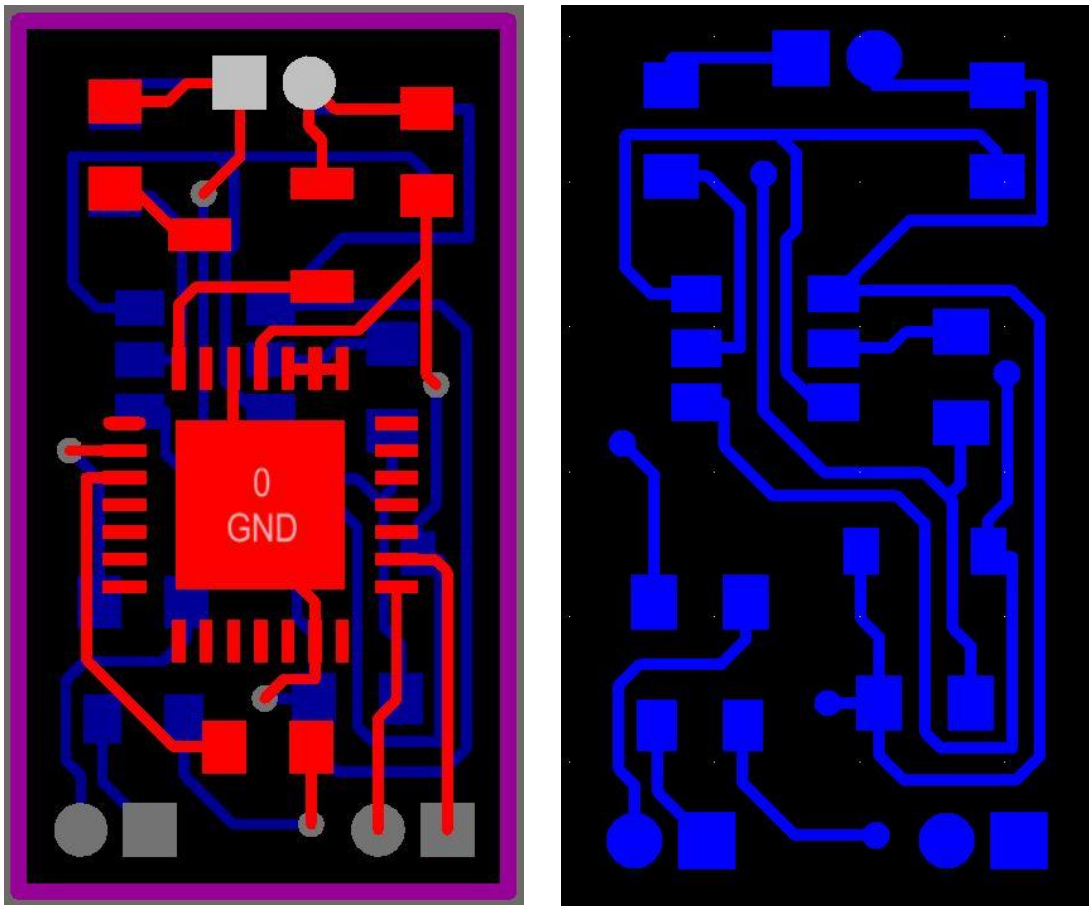

(a) (b)

Figure 7.2 PCB layout for the schematic in Figure 7.1. A view of the top layer (a) and the bottom layer (b) seen from the top.

7.1.2 Finalizing the Device

After all components including the chip were soldered on the PCB, a thin layer of polydimethylsiloxane (PDMS) was coated onto both sides of the PCB to protect the components from shorts and interference. The PDMS is a biocompatible material and is proven to be safe for implantable biomedical applications. After the thin coating was applied, the two sensors were attached to one side of the PCB, then the coil antenna was soldered to the other side. With this layout, the coil antenna could face the outer stomach while the two sensors face the inside. This configuration is beneficial to the power transfer and efficiency as it positions the antenna close to the skin and allows the two sensors to face the stomach reflux more naturally and freely than

they would when facing the wall of the esophagus. To finalize the implant, another layer of PDMS was applied to protect the circuit from fluids. The PDMS was then carefully scraped away to expose the sensing electrodes of the two sensors.

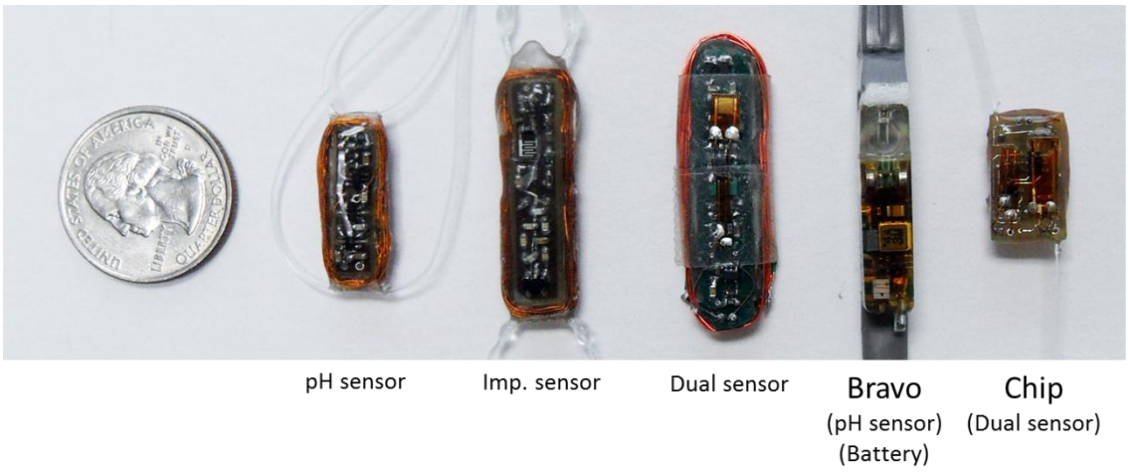

Figure 7.3 The compelete implant for GERD detector (right most) compared to other previous modes. The Bravo is the only wireless GERD detector available in the market. The size of our GERD detector is very compatible despite of the inductive coil and the dual sensors.

The outer dimension of the finalized device was measured at 1 × 1.8 cm with a thickness of 0.5 cm (Figure 7.3). The size was compared to the Bravo (single sensor) and to our previous models. The IC-based miniature device has a very compatible size. Furthermore, an inductive coil antenna provides a batteryless operation. The dual sensors can detect not only the pH level, but also the number of reflux episodes.

The new GERD detector based IC-design has been significantly reduced in size. This device can provide true long term monitoring for GERD detection.

7.2 Experimental Setup and Results

7.2.1 Experimental Setup

A tag antenna was set at 4 cm from a reader antenna in the separation stage illustrated in Figure 6.3. The dimension of the tag antennas was measured at 1 × 1.5 cm^2. The reader antenna was chosen from a group of antennas that provided good power transfer with relatively high efficiency and low current consumption. The chosen reader antenna had a radius of 5 cm and 17 coil turns.

The implant was then tested with the direct parameter inputs instead of using sensors. For this experiment, extensions were used to prolong the input terminals for the sensing circuitries. The carrier frequency on the reader side was set at 1.3 MHz from a function generator.

7.2.2 Benchtop Test and Results

The results for the benchtop experiment were plotted in Figure 7.4. Unlike the results from Chapter 5, the output frequency tends to saturate as the input voltage is increased. This is due to the floating voltage added into the input of the VCO. The experiments in Chapter 5 were direct measurements for the outputs on the chip, which it did not face a virtual ground problem. This caused saturation and reduced the output span due to the interference from the floating voltage. However, the variation of the output frequency varied from 68.3 kHz to 81.1 kHz for the input ranging from -0.4 V to 0.7 V. This output span is still considered appropriate for distinguishing and properly interpreting the data.

The results from the impedance test were very similar to those described in Chapter 5. The virtual ground issue from the pH sensor test did not occur for the relaxation oscillator as the floating VDC did not affect the impedance change to the relaxation oscillator. The frequency span measured ranged from 16.29 kHz to 6.993 kHz for the input impedance varying from short to 1 MΩ. The output frequency for infinite impedance was measured at 5.882 kHz implying that the total variation of the output is 10.408 kHz.

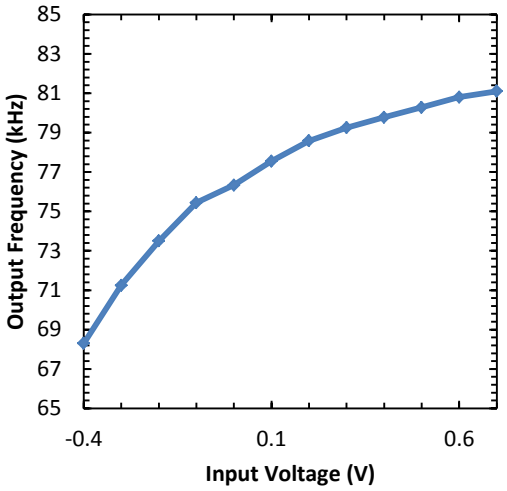

(a)

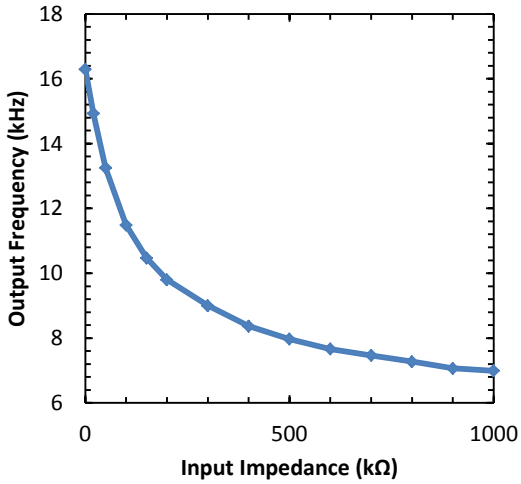

(b)

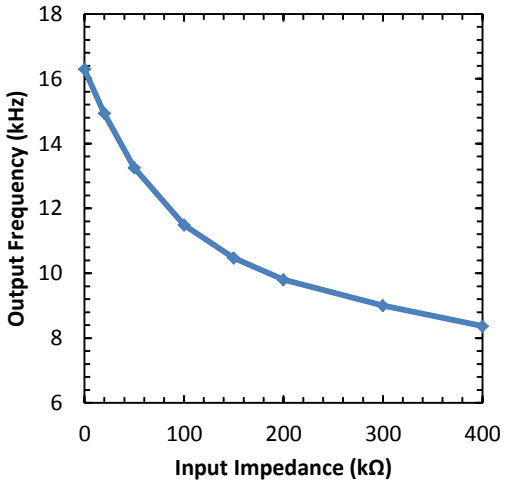

(c)

Figure 7.4 Results from the benchtop tests via wireless. The output of VCO is quantitatively distinguished despite of the saturation trend (a). The frequency span for the relaxation oscillator (b) was similar to the wired data acquisition done in Chapter 5. A close look for the input impedance from zero to 400 kΩ is shown in (c).

7.3 Experimental Setup and Results for GERD Application

The pH sensor measured the pH level of the pH buffer solutions from pH 4 to pH 10 as shown in Figure 7.5 (a). Hydrochloride (HCl) was used to produce a pH of 1.8, mimicking stomach acid. The acid solutions generated higher voltage in the sensor meaning that the plot should have been reversed as the pH 10 (alkaline) was supposed to provide the lowest frequency in the figure. This discrepancy was caused by a reversal of the electrodes of the pH sensor. This was done in order to avoid the saturation effects seen in Figure 7.4 (a),

Furthermore, the impedance test was carried out using the impedance sensor that was explained in Chapter 2.4.1. The main role of the impedance sensor was to detect the presence of fluid by measuring its impedance. When the fluid appeared on the sensor, it lowered the impedance level. As the reflux was not presented, the impedance became infinite. Using this mechanism, the number of flux episode could be counted. Figure 7.5 (b) displays the concept we predicted. The hydrochloride that had the most ion concentration provided very low impedance, almost shorting the sensor and producing a frequency as high as 16.03 kHz. In contrast, the DI water, having a very low ion concentration, drove impedance very low. The presence of fluid was successfully distinguished using our sensing system.

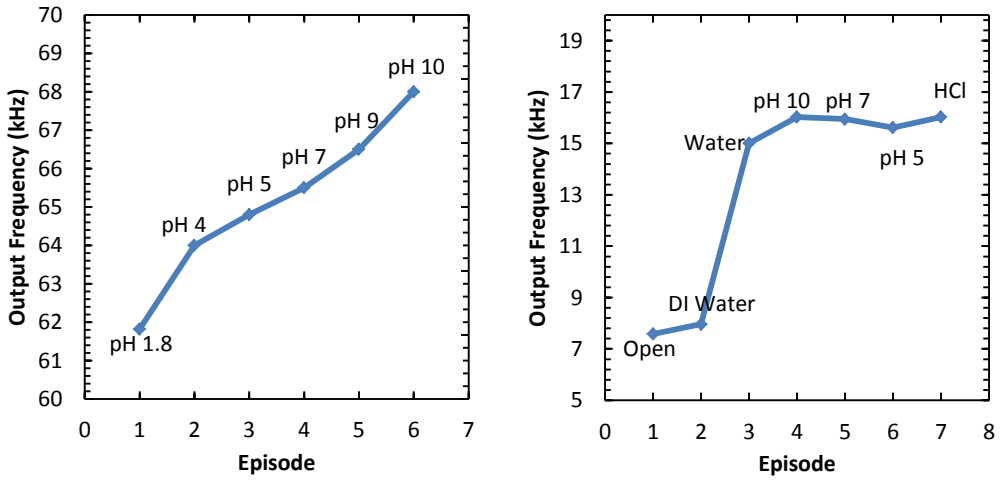

(a) (b)

Figure 7.5 The pH level (a) and Impedance level (b) test.

The reversed electrodes of the pH sensor connected to the GERD system reversed the output frequency range, as the pH 10 (alkaline) provided the highest frequency despite delivering the lowest voltage to the VCO. The difference between open circuit (no presence of fluid) and HCl (very low impedance) was measured at 8.45 kHz, which is considered a very high resolution to detect the number of flux episodes.

The reaction to a fluid for the impedance sensor depends on ion concentration in the fluid. The pH levels of the pH buffer solutions are not based on ion concentration. Due to this reason, pH buffer solutions were not suitable for the impedance sensor to be tested for detailed performance. Therefore, different solutions were provided for the next experiment.

Potassium choloride (KCl), hydrochloric acid (HCl) and sodium chloride (NaCl) were separately diluted in DI water, mimicking stomach fluids. The concentration of the KCl, HCl and NaCl were increased by double for each test. These highly ion concentrated solutions were tested with the impedance sensor for the detailed performance. The results are shown in Figure 7.6.

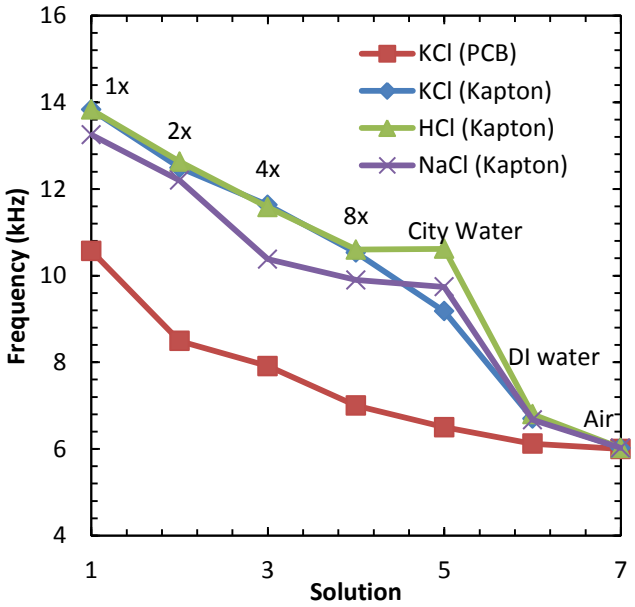

Figure 7.6 Increment of ion concentration yields decrement of the output frequency of the relaxation oscillator.

City water, Di water and air were used to compare the results. The increment of the ion concentration yielded a decrement of the output frequency of the relaxation oscillator. To verify the versatile operation of the relaxation oscillator, two different types of impedance sensors were used. The PCB based impedance sensor yielded a smaller frequency span. However, the frequency resolution was still suitable for measuring the impedance level.

The last experiment was carried out for the two sensors in the same solutions. The results are shown in Figure 7.7.

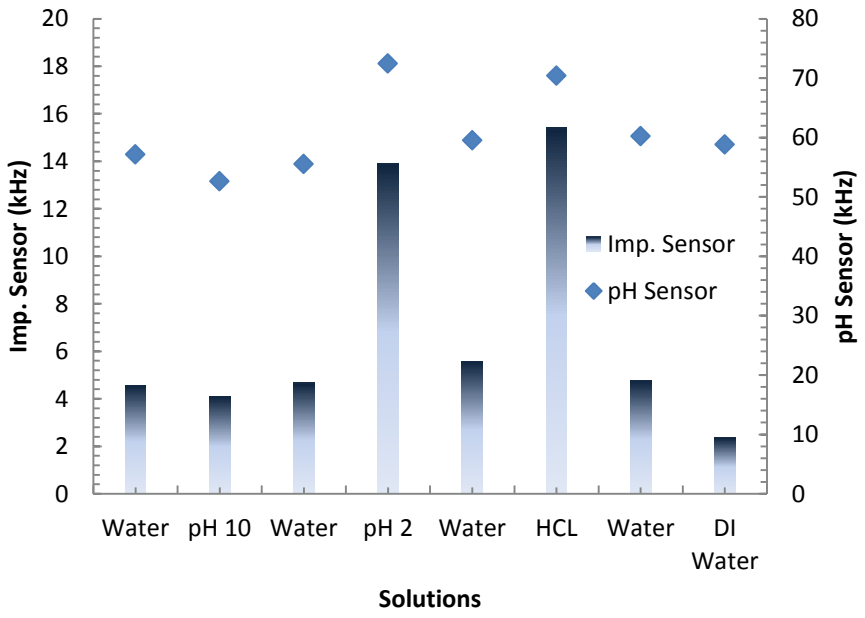

Figure 7.7 The sensing performance for the two sensors in the same solutions

Both sensors operated without mutual interference. The results we measured were very similar to the previous data.

Hence, the GERD detector has been successfully implemented and tested using the IC based on chip. The total dimension has been reduced to one third of the dimensions of the previous dual-sensing module. The minimum and maximum current consumptions of the chip including the ESD circuit were measured at 28.33 μA and 49.583 μA, respectively.

CHAPTER 8

CONCLUSIONS, OTHER APPLICATIONS, AND FUTURE WORK

8.1 Conclusions

Optimizing the oscillator design is the key to utilizing the sensing system in a universal platform. Multi-band frequency modulation encodes the multi-modal signals onto a single carrier frequency for transduction. This research work has demonstrated the integrated circuit design by using a standard CMOS technology. On Semiconductor 0.5-μm technology was used for chip implementation while the charge pump was off-chip due to the capacitor values and Schottky diode implementation. ESD protection circuits were used to prevent permanent damage of the chip from high voltages such as electrostatic discharges. This work also implemented the wireless operation of two sensors integrated in one batteryless – wireless implantable capsule. The system was powered from an external transmitter by inductive coupling. This universal platform can be also used for other types of sensors as long as they generate voltage, capacitance, or amperometric analog signals. The versatility of the system was demonstrated by transduction of the different parameters from the benchtop tests.

The maximum current consumption was as low as 49.58 μA at an operating voltage of 2.1 V. Ergo, this low power consumption of the complete chip can enable a variety of applications not only in biomedical fields, but also in industrial and scientific areas. If required, the sensing module can work with the aid of a battery to provide stable sensing operations over long periods owing to the small power consumption.

This work also investigated methods to increase the transferred power and efficiency by selecting the proper antenna designs. The best optimum reader antennas were obtained with radius of 5 cm in terms of power transfer, efficiency, and parasitic effects. Furthermore, the size of 5 cm in radius is a very comfortable size for portable power transmitter

and reader that is operated by a rechargeable battery. The tradeoff between high power transfer and high efficiency can be adjusted by winding different number of coil turns for the antenna. In the course of this research, intensity, divergence, boundaries, and 3dB lines of transferred power and efficiency were also mapped. These maps can serve as a guideline to decide tolerances for antenna separation and mis-alignment for future sensing system designs.

The IC design has miniaturized the sensing circuitries down to 1.95 × 1.95 mm^2 making it suitable for implant applications. With the inductive coupling method for wireless power harvesting, a batteryless and wireless operation was implemented and successfully demonstrated. This complete system provides a true long term monitoring for patients. The batteryless system can minimize the number of invasive surgeries generally required to replace batteries and maximize patients' comfort.

8.2 Other Applications

8.2.1 Bladder Volume Monitoring

Urinary incontinence is lack of controlling the bladder. The nerve endings of the urinary system are damaged and in extreme cases are unable to signal bladder voiding leading to involuntary loss of urine [73].

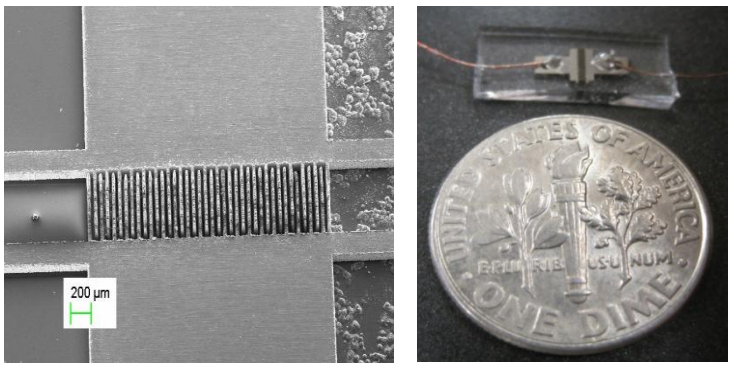

(a) (b)

Figure 8.1 The fabricated IDC sensor (a) is compared for size (b) [74]

Using our chip, an implantable system for monitoring bladder volume can be implemented with an IDC (interdigitated capacitance) sensor (Figure 8.1 (b)). The capacitance on the interdigitated structure varies as the fingers are stretched in and out. The stretching can be mapped to the expansion of the bladder. In this mechanism, the bladder volume can be measured in terms of the capacitance value on the sensor. The fabricated IDC sensors have initial capacitance varying from 10 to 15 pF. Depending on the stretching, the capacitance changes up 1 pF. To maximized resolution of output for this small variation, an additional connection was made to the RO to improve resolution, as in the Figure 8.2.

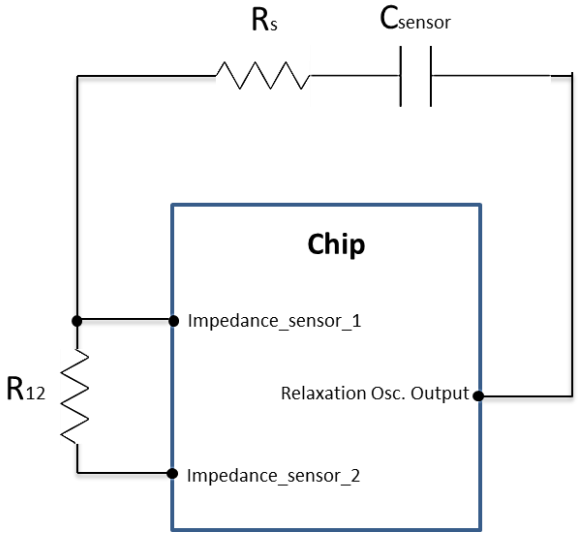

Figure 8.2 Block diagram of connection to maximize output variation for a small capacitive input variation as 1 pF.

By using the Figure 8.2, the variation of the outputs from the relaxation oscillator was measured in in the range of 22.12 – 23.7 kHz. The Δf was measured as 1.45 kHz. This result can help translate information about the bladder volume. For better resolution, an operational or instrumental amplifier can be used with the chip.

8.2.2 Cataracts

Cataracts affect nearly 20.5 million Americans age 40 and older. By age 80, more than half of all Americans have cataracts. It is estimated that the federal government spends more than $3.4 billion each year treating cataracts through the Medicare program [75]. One of the most common methods to treat cataract is surgery, which involves removing the clouded lens and replacing it with a plastic lens implant called Intraocular lens (IOL) as Figure 8.3. The replacement lens sits in the same place as your natural lens and becomes part of your eye [76].

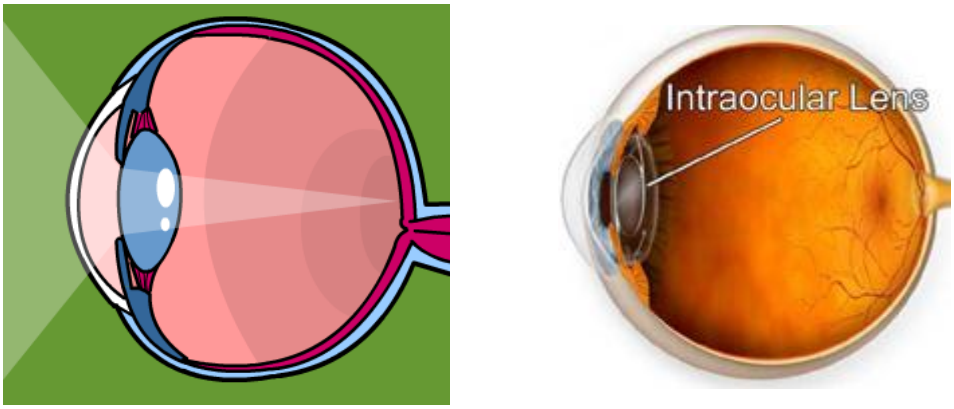

(a) (b)

Figure 8.3 Crystal lens (a) and implanted intraocular lens (b)

Intraocular lens (IOL)

A Monofocal Lens Implant in Figure 8.4 (a) is the most basic type of Lens Implant used to correct vision after Cataract Surgery. A Monofocal Lens Implant can provide very good vision after Cataract Surgery, but only at one set distance. Usually the lens is fabricated for farsightedness. A Monofocal Lens Implant does not correct intermediate or arm's length vision and near field vision. Thus patients electing to have Monofocal Lens Implants will be dependent on glasses either some or most of the time in about 70% of cases [77].

In order to prevent the use of glasses, a multifocal IOL has been developed. A multifocal lens implant focuses light from distance and near simultaneously. This feature addresses both distant and near vision and makes the recipient less dependent on glasses or

contact lenses [77]. The trade-off for simultaneous distance and near vision with multifocal lenses is a higher amount of optical aberrations produced by the lenses multifocal optics. Typically, these aberrations are perceived as glare in certain low lighting situations and halos around light sources at night. Most people with multifocal lenses find these aberrations to be only mildly annoying. In fact, the brain tends to adapt to them with time. However, full adaptation may take several months.

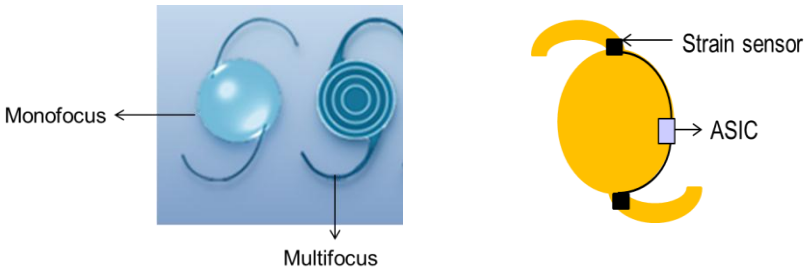

(a) (b)

Figure 8.4 Mono- and multi-focus IOS (a) and integrated strain sensor and driving circuitry (b)

So as an extension of this research, the small footprint of the ASIC ship would allow integration with the multifocal lens to sense the movement of the cilary muscle the eye during accommodation to focus on far and near objects as in Figure 8.4 (b).

8.3 Future Work

- Multiple Channels

  A dual channel sensing system may not be enough for some applications. Increasing channels will widen applicable fields. The MUX and DEMUX will be redesigned to provide proper functionalities in controlling more than two sensing circuitries and their outputs.

- Differential Amplifier for VCO

  The floating voltage affected the input parameter, and it altered the output frequency of the VCO as seen the results in section 7.2.2. Instead of using a single input to the VCO, outputs of a differential amplifier can be used to minimize the interference from the floating voltage.

- On-Chip Charge Pump

  The off-chip charge pump occupied the most space on the PCB for the GERD application. For further size reduction, the charge pump should be considered for on-chip design. Since the C5N process does not provide an official fabrication for Schottky diodes, different methods should be researched to reduce V_{th} effects for MOSFET diodes.

- Stimulator

  The energy harvesting via the inductive coupling collects relatively high power compared to other harvesting methods. This power is enough to operate stimulators that require intensive power in milliwatts for a gastro stimulator. With a pre-programmed microcontroller and stimulation module, our chip can be used as a gastro stimulator

APPENDIX A

MOSIS MODEL FILES FOR CORNER ANALYSIS FOR AMI06(C5N)

AMI_T22Y_TT (TYPICAL)

```
* Tech: AMI_C5N
* LOT: T22Y_TT (typical)                WAF: 3104
* Temperature_parameters=Optimized
.MODEL ami06N NMOS (                          LEVEL   = 11
+VERSION = 3.1          TNOM    = 27          TOX     = 1.39E-8
+XJ      = 1.5E-7       NCH     = 1.7E17      VTH0    = 0.6696061
+K1      = 0.8351612    K2      = -0.0839158  K3      = 23.1023856
+K3B     = -7.6841108   W0      = 1E-8        NLX     = 1E-9
+DVT0W   = 0            DVT1W   = 0           DVT2W   = 0
+DVT0    = 2.9047241    DVT1    = 0.4302695   DVT2    = -0.134857
+U0      = 458.439679   UA      = 1E-13       UB      = 1.485499E-18
+UC      = 1.629939E-11 VSAT    = 1.643993E5  A0      = 0.6103537
+AGS     = 0.1194608    B0      = 2.674756E-6 B1      = 5E-6
+KETA    = -2.640681E-3 A1      = 8.219585E-5 A2      = 0.3564792
+RDSW    = 1.387108E3   PRWG    = 0.0299916   PRWB    = 0.0363981
+WR      = 1            WINT    = 2.472348E-7 LINT    = 3.597605E-8
+XL      = 0            XW      = 0           DWG     = -1.287163E-8
+DWB     = 5.306586E-8  VOFF    = 0           NFACTOR = 0.8365585
+CIT     = 0            CDSC    = 2.4E-4      CDSCD   = 0
+CDSCB   = 0            ETA0    = 0.0246738   ETAB    = -1.406123E-3
+DSUB    = 0.2543458    PCLM    = 2.5945188   PDIBLC1 = -0.4282336
+PDIBLC2 = 2.311743E-3  PDIBLCB = -0.0272914  DROUT   = 0.7283566
+PSCBE1  = 5.598623E8   PSCBE2  = 5.461645E-5 PVAG    = 0
+DELTA   = 0.01         RSH     = 81.8        MOBMOD  = 1
+PRT     = 8.621        UTE     = -1          KT1     = -0.2501
+KT1L    = -2.58E-9     KT2     = 0           UA1     = 5.4E-10
+UB1     = -4.8E-19     UC1     = -7.5E-11    AT      = 1E5
+WL      = 0            WLN     = 1           WW      = 0
+WWN     = 1            WWL     = 0           LL      = 0
+LLN     = 1            LW      = 0           LWN     = 1
+LWL     = 0            CAPMOD  = 2           XPART   = 0.5
+CGDO    = 2E-10        CGSO    = 2E-10       CGBO    = 1E-9
+CJ      = 4.197772E-4  PB      = 0.99        MJ      = 0.4515044
+CJSW    = 3.242724E-10 PBSW    = 0.1         MJSW    = 0.1153991
+CJSWG   = 1.64E-10     PBSWG   = 0.1         MJSWG   = 0.1153991
+CF      = 0            PVTH0   = 0.0585501   PRDSW   = 133.285505
+PK2     = -0.0299638   WKETA   = -0.0248758  LKETA   = 1.173187E-3
+AF      = 1            KF      = 0)
*
.MODEL ami06P PMOS (                          LEVEL   = 11
+VERSION = 3.1          TNOM    = 27          TOX     = 1.39E-8
+XJ      = 1.5E-7       NCH     = 1.7E17      VTH0    = -0.9214347
+K1      = 0.5553722    K2      = 8.763328E-3 K3      = 6.3063558
+K3B     = -0.6487362   W0      = 1.280703E-8 NLX     = 2.593997E-8
+DVT0W   = 0            DVT1W   = 0           DVT2W   = 0
+DVT0    = 2.5131165    DVT1    = 0.5480536   DVT2    = -0.1186489
+U0      = 212.0166131  UA      = 2.807115E-9 UB      = 1E-21
+UC      = -5.82128E-11 VSAT    = 1.713601E5  A0      = 0.8430019
+AGS     = 0.1328608    B0      = 7.117912E-7 B1      = 5E-6
```

```
+KETA    = -3.674859E-3   A1      = 4.77502E-5     A2      = 0.3
+RDSW    = 2.837206E3     PRWG    = -0.0363908     PRWB    = -1.016722E-5
+WR      = 1              WINT    = 2.838038E-7    LINT    = 5.528807E-8
+XL      = 0              XW      = 0              DWG     = -1.606385E-8
+DWB     = 2.266386E-8    VOFF    = -0.0558512     NFACTOR = 0.9342488
+CIT     = 0              CDSC    = 2.4E-4         CDSCD   = 0
+CDSCB   = 0              ETA0    = 0.3251882      ETAB    = -0.0580325
+DSUB    = 1              PCLM    = 2.2409567      PDIBLC1 = 0.0411445
+PDIBLC2 = 3.355575E-3    PDIBLCB = -0.0551797     DROUT   = 0.2036901
+PSCBE1  = 6.44809E9      PSCBE2  = 6.300848E-10   PVAG    = 0
+DELTA   = 0.01           RSH     = 101.6          MOBMOD  = 1
+PRT     = 59.494         UTE     = -1             KT1     = -0.2942
+KT1L    = 1.68E-9        KT2     = 0              UA1     = 4.5E-9
+UB1     = -6.3E-18       UC1     = -1E-10         AT      = 1E3
+WL      = 0              WLN     = 1              WW      = 0
+WWN     = 1              WWL     = 0              LL      = 0
+LLN     = 1              LW      = 0              LWN     = 1
+LWL     = 0              CAPMOD  = 2              XPART   = 0.5
+CGDO    = 2.9E-10        CGSO    = 2.9E-10        CGBO    = 1E-9
+CJ      = 7.235528E-4    PB      = 0.9527355      MJ      = 0.4955293
+CJSW    = 2.692786E-10   PBSW    = 0.99           MJSW    = 0.2958392
+CJSWG   = 6.4E-11        PBSWG   = 0.99           MJSWG   = 0.2958392
+CF      = 0              PVTH0   = 5.98016E-3     PRDSW   = 14.8598424
+PK2     = 3.73981E-3     WKETA   = 5.292165E-3    LKETA   = -4.205905E-3
+AF      = 1              KF      = 0)
*
```

```
* LOT: T22Y_FF (fast-fast)                WAF: 3110
* Temperature_parameters=Optimized
.MODEL ami06n NMOS (                          LEVEL   = 11
+VERSION = 3.1          TNOM    = 27          TOX     = 1.39E-8
+XJ      = 1.5E-7       NCH     = 1.7E17      VTH0    = 0.6252608
+K1      = 0.8530381    K2      = -0.0937042  K3      = 25.5736581
+K3B     = -7.2969383   W0      = 1E-8        NLX     = 1E-9
+DVT0W   = 0            DVT1W   = 0           DVT2W   = 0
+DVT0    = 3.4153341    DVT1    = 0.4318353   DVT2    = -0.1001188
+U0      = 461.2276323  UA      = 1E-13       UB      = 1.46812E-18
+UC      = 1.421961E-11 VSAT    = 1.555424E5  A0      = 0.7155223
+AGS     = 0.1483817    B0      = 2.54418E-6  B1      = 5E-6
+KETA    = 1.388284E-5  A1      = 7.294903E-5 A2      = 0.3921052
+RDSW    = 1.305357E3   PRWG    = 0.0488517   PRWB    = 0.0366783
+WR      = 1            WINT    = 2.274256E-7 LINT    = 3.776271E-8
+XL      = 0            XW      = 0           DWG     = -8.845179E-9
+DWB     = 6.105959E-8  VOFF    = 0           NFACTOR = 0.5636274
+CIT     = 0            CDSC    = 2.4E-4      CDSCD   = 0
+CDSCB   = 0            ETA0    = 0.0345642   ETAB    = -1.428288E-3
+DSUB    = 0.3127341    PCLM    = 2.6236271   PDIBLC1 = -0.3319738
+PDIBLC2 = 2.390366E-3  PDIBLCB = -0.0300257  DROUT   = 0.6600306
+PSCBE1  = 5.488078E8   PSCBE2  = 4.431797E-5 PVAG    = 0
+DELTA   = 0.01         RSH     = 81.8        MOBMOD  = 1
+PRT     = 8.621        UTE     = -1          KT1     = -0.2501
+KT1L    = -2.58E-9     KT2     = 0           UA1     = 5.4E-10
+UB1     = -4.8E-19     UC1     = -7.5E-11    AT      = 1E5
+WL      = 0            WLN     = 1           WW      = 0
+WWN     = 1            WWL     = 0           LL      = 0
+LLN     = 1            LW      = 0           LWN     = 1
+LWL     = 0            CAPMOD  = 2           XPART   = 0.5
+CGDO    = 1.98E-10     CGSO    = 1.98E-10    CGBO    = 1E-9
+CJ      = 4.198358E-4  PB      = 0.99        MJ      = 0.4516115
+CJSW    = 3.241716E-10 PBSW    = 0.1000811   MJSW    = 0.1152935
+CJSWG   = 1.64E-10     PBSWG   = 0.1000811   MJSWG   = 0.1152935
+CF      = 0            PVTH0   = 0.1033668   PRDSW   = 59.9594347
+PK2     = -0.0304166   WKETA   = -0.0144288  LKETA   = 3.115505E-3
+AF      = 1            KF      = 0)
*
.MODEL ami06p PMOS (                          LEVEL   = 11
+VERSION = 3.1          TNOM    = 27          TOX     = 1.39E-8
+XJ      = 1.5E-7       NCH     = 1.7E17      VTH0    = -0.8880096
+K1      = 0.533922     K2      = 3.259424E-3 K3      = 4.9517158
+K3B     = -0.6918832   W0      = 1.515912E-8 NLX     = 3.554945E-9
+DVT0W   = 0            DVT1W   = 0           DVT2W   = 0
+DVT0    = 2.4926947    DVT1    = 0.530833    DVT2    = -0.1185572
+U0      = 211.6791804  UA      = 2.785001E-9 UB      = 1E-21
+UC      = -5.76365E-11 VSAT    = 1.732495E5  A0      = 0.9378784
+AGS     = 0.1630399    B0      = 7.147395E-7 B1      = 5E-6
+KETA    = 1.410441E-4  A1      = 0           A2      = 0.3
```

```
+RDSW    = 3E3          PRWG    = -0.0490272     PRWB    = 8.254155E-5
+WR      = 1            WINT    = 2.696991E-7    LINT    = 6.103973E-8
+XL      = 0            XW      = 0              DWG     = -1.293462E-8
+DWB     = 2.202201E-8  VOFF    = -0.0500647     NFACTOR = 0.8235545
+CIT     = 0            CDSC    = 2.4E-4         CDSCD   = 0
+CDSCB   = 0            ETA0    = 0.4342722      ETAB    = -6.780063E-3
+DSUB    = 1            PCLM    = 2.3221049      PDIBLC1 = 0.036845
+PDIBLC2 = 3.86901E-3   PDIBLCB = -0.0457025     DROUT   = 0.1909189
+PSCBE1  = 1.678442E10  PSCBE2  = 1.640115E-9    PVAG    = 0.0133488
+DELTA   = 0.01         RSH     = 101.7          MOBMOD  = 1
+PRT     = 59.494       UTE     = -1             KT1     = -0.2942
+KT1L    = 1.68E-9      KT2     = 0              UA1     = 4.5E-9
+UB1     = -6.3E-18     UC1     = -1E-10         AT      = 1E3
+WL      = 0            WLN     = 1              WW      = 0
+WWN     = 1            WWL     = 0              LL      = 0
+LLN     = 1            LW      = 0              LWN     = 1
+LWL     = 0            CAPMOD  = 2              XPART   = 0.5
+CGDO    = 2.75E-10     CGSO    = 2.75E-10       CGBO    = 1E-9
+CJ      = 7.235521E-4  PB      = 0.9527404      MJ      = 0.4955303
+CJSW    = 2.692736E-10 PBSW    = 0.99           MJSW    = 0.295843
+CJSWG   = 6.4E-11      PBSWG   = 0.99           MJSWG   = 0.295843
+CF      = 0            PVTH0   = 5.98016E-3     PRDSW   = 14.8598424
+PK2     = 3.73981E-3   WKETA   = 5.10041E-3     LKETA   = -1.725699E-3
+AF      = 1            KF      = 0)
*
```

AMI_T22Y_FS (FAST SLOW)

```
* DATE: May 24/02
* Tech: AMI_C5N
* LOT: T22Y_FS (fast-slow)              WAF: 3103
* Temperature_parameters=Optimized
.MODEL ami06n NMOS (                    LEVEL   = 11
+VERSION = 3.1          TNOM    = 27          TOX     = 1.39E-8
+XJ      = 1.5E-7       NCH     = 1.7E17      VTH0    = 0.6406873
+K1      = 0.8993265    K2      = -0.1056377  K3      = 21.3163919
+K3B     = -7.1608652   W0      = 1E-8        NLX     = 1E-9
+DVT0W   = 0            DVT1W   = 0           DVT2W   = 0
+DVT0    = 3.5203013    DVT1    = 0.4082348   DVT2    = -0.0884394
+U0      = 459.8817656  UA      = 1E-13       UB      = 1.519768E-18
+UC      = 1.390305E-11 VSAT    = 1.618085E5  A0      = 0.6561988
+AGS     = 0.1483929    B0      = 2.633747E-6 B1      = 5E-6
+KETA    = 1.06352E-3   A1      = 7.568286E-5 A2      = 0.3677153
+RDSW    = 1.235008E3   PRWG    = 0.0513137   PRWB    = 0.0510984
+WR      = 1            WINT    = 2.396297E-7 LINT    = 3.585449E-8
+XL      = 0            XW      = 0           DWG     = -1.245253E-8
+DWB     = 5.532278E-8  VOFF    = 0           NFACTOR = 0.6559298
+CIT     = 0            CDSC    = 2.4E-4      CDSCD   = 0
+CDSCB   = 0            ETA0    = 0.0330898   ETAB    = -1.406156E-3
+DSUB    = 0.2997589    PCLM    = 2.6313228   PDIBLC1 = -0.40275
+PDIBLC2 = 2.205592E-3  PDIBLCB = -0.0272899  DROUT   = 0.7201569
+PSCBE1  = 5.601647E8   PSCBE2  = 5.450628E-5 PVAG    = 7.40725E-3
+DELTA   = 0.01         RSH     = 81.2        MOBMOD  = 1
+PRT     = 8.621        UTE     = -1          KT1     = -0.2501
+KT1L    = -2.58E-9     KT2     = 0           UA1     = 5.4E-10
+UB1     = -4.8E-19     UC1     = -7.5E-11    AT      = 1E5
+WL      = 0            WLN     = 1           WW      = 0
+WWN     = 1            WWL     = 0           LL      = 0
+LLN     = 1            LW      = 0           LWN     = 1
+LWL     = 0            CAPMOD  = 2           XPART   = 0.5
+CGDO    = 2.03E-10     CGSO    = 2.03E-10    CGBO    = 1E-9
+CJ      = 4.198358E-4  PB      = 0.99        MJ      = 0.4516115
+CJSW    = 3.241716E-10 PBSW    = 0.1000811   MJSW    = 0.1152935
+CJSWG   = 1.64E-10     PBSWG   = 0.1000811   MJSWG   = 0.1152935
+CF      = 0            PVTH0   = 0.0766435   PRDSW   = 163.0361088
+PK2     = -0.0297388   WKETA   = -0.0214699  LKETA   = -2.14921E-5
+AF      = 1            KF      = 0)
*
.MODEL ami06p PMOS (                    LEVEL   = 11
+VERSION = 3.1          TNOM    = 27          TOX     = 1.39E-8
+XJ      = 1.5E-7       NCH     = 1.7E17      VTH0    = -1.0173478
+K1      = 0.5658287    K2      = 0.0116517   K3      = 10.5698978
+K3B     = -0.7608774   W0      = 1E-8        NLX     = 9.01509E-8
+DVT0W   = 0            DVT1W   = 0           DVT2W   = 0
+DVT0    = 3.3035484    DVT1    = 0.5614757   DVT2    = -0.0733879
+U0      = 213.2201651  UA      = 2.872001E-9 UB      = 1.05947E-21
+UC      = -5.43332E-11 VSAT    = 1.545629E5  A0      = 0.4566597
```

```
+AGS     = 0            B0      = 6.789661E-7    B1      = 5E-6
+KETA    = -8.389653E-3   A1      = 4.693067E-8    A2      = 0.3
+RDSW    = 3E3          PRWG    = -0.046965      PRWB    = -6.108168E-5
+WR      = 1            WINT    = 2.938786E-7    LINT    = 5.685662E-8
+XL      = 0            XW      = 0              DWG     = -1.995328E-8
+DWB     = 2.020066E-8    VOFF    = -0.0719834     NFACTOR = 0.7501867
+CIT     = 0            CDSC    = 2.4E-4         CDSCD   = 0
+CDSCB   = 0            ETA0    = 0.1503769      ETAB    = -0.0623126
+DSUB    = 0.8623589      PCLM    = 2.2059151      PDIBLC1 = 0.0239419
+PDIBLC2 = 3.052934E-3    PDIBLCB = -0.0972847     DROUT   = 0.1509141
+PSCBE1  = 5.116843E9     PSCBE2  = 5E-10          PVAG    = 0
+DELTA   = 0.01           RSH     = 101.5          MOBMOD  = 1
+PRT     = 59.494         UTE     = -1             KT1     = -0.2942
+KT1L    = 1.68E-9        KT2     = 0              UA1     = 4.5E-9
+UB1     = -6.3E-18       UC1     = -1E-10         AT      = 1E3
+WL      = 0            WLN     = 1              WW      = 0
+WWN     = 1            WWL     = 0              LL      = 0
+LLN     = 1            LW      = 0              LWN     = 1
+LWL     = 0            CAPMOD  = 2              XPART   = 0.5
+CGDO    = 3.18E-10       CGSO    = 3.18E-10       CGBO    = 1E-9
+CJ      = 7.235521E-4    PB      = 0.9527404      MJ      = 0.4955303
+CJSW    = 2.692736E-10   PBSW    = 0.99           MJSW    = 0.295843
+CJSWG   = 6.4E-11        PBSWG   = 0.99           MJSWG   = 0.295843
+CF      = 0            PVTH0   = 5.98016E-3     PRDSW   = 14.8598424
+PK2     = 3.73981E-3     WKETA   = 2.574681E-3    LKETA   = -7.296621E-3
+AF      = 1            KF      = 0)
*
```

AMI_T22Y_SF (SLOW FAST)

```
* DATE: May 28/02
* Tech: AMI_C5N
* LOT: T22Y_SF (slow-fast)              WAF: 3108
* Temperature_parameters=Optimized
.MODEL ami06n NMOS (                          LEVEL   = 11
+VERSION = 3.1          TNOM    = 27          TOX     = 1.39E-8
+XJ      = 1.5E-7       NCH     = 1.7E17      VTH0    = 0.7149035
+K1      = 0.9483936    K2      = -0.1143426  K3      = 22.9362167
+K3B     = -7.5062363   W0      = 1E-8        NLX     = 1E-9
+DVT0W   = 0            DVT1W   = 0           DVT2W   = 0
+DVT0    = 3.3919449    DVT1    = 0.4489453   DVT2    = -0.1041249
+U0      = 457.716722   UA      = 1E-13       UB      = 1.372758E-18
+UC      = 9.187767E-12 VSAT    = 1.587379E5  A0      = 0.4423616
+AGS     = 0.074408     B0      = 2.495758E-6 B1      = 5E-6
+KETA    = -7.852725E-3 A1      = 0           A2      = 0.3722219
+RDSW    = 1.37701E3    PRWG    = 0.0473261   PRWB    = 0.0143246
+WR      = 1            WINT    = 2.276625E-7 LINT    = 3.643153E-8
+XL      = 0            XW      = 0           DWG     = -8.492651E-9
+DWB     = 5.745769E-8  VOFF    = -1.122941E-3 NFACTOR = 0.9488846
+CIT     = 0            CDSC    = 2.4E-4      CDSCD   = 0
+CDSCB   = 0            ETA0    = 0.0194621   ETAB    = -1.316507E-3
+DSUB    = 0.2373912    PCLM    = 2.609637    PDIBLC1 = -0.2869359
+PDIBLC2 = 2.596336E-3  PDIBLCB = -9.96922E-3 DROUT   = 0.6175652
+PSCBE1  = 5.8967E8     PSCBE2  = 8.951955E-5 PVAG    = 0
+DELTA   = 0.01         RSH     = 81.7        MOBMOD  = 1
+PRT     = 8.621        UTE     = -1          KT1     = -0.2501
+KT1L    = -2.58E-9     KT2     = 0           UA1     = 5.4E-10
+UB1     = -4.8E-19     UC1     = -7.5E-11    AT      = 1E5
+WL      = 0            WLN     = 1           WW      = 0
+WWN     = 1            WWL     = 0           LL      = 0
+LLN     = 1            LW      = 0           LWN     = 1
+LWL     = 0            CAPMOD  = 2           XPART   = 0.5
+CGDO    = 2.03E-10     CGSO    = 2.03E-10    CGBO    = 1E-9
+CJ      = 4.198358E-4  PB      = 0.99        MJ      = 0.4516115
+CJSW    = 3.241716E-10 PBSW    = 0.1000811   MJSW    = 0.1152935
+CJSWG   = 1.64E-10     PBSWG   = 0.1000811   MJSWG   = 0.1152935
+CF      = 0            PVTH0   = 0.0690695   PRDSW   = 181.3444668
+PK2     = -0.0304429   WKETA   = 0.0420944   LKETA   = -3.044755E-3
+AF      = 1            KF      = 0)
*
.MODEL ami06p PMOS (                          LEVEL   = 11
+VERSION = 3.1          TNOM    = 27          TOX     = 1.39E-8
+XJ      = 1.5E-7       NCH     = 1.7E17      VTH0    = -0.8558405
+K1      = 0.5644444    K2      = 6.387376E-3 K3      = 6.0462612
+K3B     = -0.5998096   W0      = 1E-8        NLX     = 3.340021E-8
+DVT0W   = 0            DVT1W   = 0           DVT2W   = 0
+DVT0    = 2.4979627    DVT1    = 0.5476217   DVT2    = -0.1143472
+U0      = 211.0603347  UA      = 2.770099E-9 UB      = 1.044234E-21
+UC      = -5.9315E-11  VSAT    = 1.779657E5  A0      = 1.1297757
+AGS     = 0.172519     B0      = 6.127953E-7 B1      = 5E-6
```

```
+KETA    = -1.991554E-3   A1      = 0            A2      = 0.3
+RDSW    = 3E3            PRWG    = -0.0477698     PRWB    = -1.197112E-4
+WR      = 1              WINT    = 2.778374E-7    LINT    = 5.81705E-8
+XL      = 0              XW      = 0              DWG     = -1.563705E-8
+DWB     = 2.218513E-8    VOFF    = -0.0660365     NFACTOR = 0.9061795
+CIT     = 0              CDSC    = 2.4E-4         CDSCD   = 0
+CDSCB   = 0              ETA0    = 0.1521419      ETAB    = -0.0473117
+DSUB    = 1              PCLM    = 2.3170883      PDIBLC1 = 0.0640318
+PDIBLC2 = 4.224165E-3    PDIBLCB = -0.0417139     DROUT   = 0.2703555
+PSCBE1  = 5.427801E9     PSCBE2  = 5.303858E-10   PVAG    = 0
+DELTA   = 0.01           RSH     = 102.2          MOBMOD  = 1
+PRT     = 59.494         UTE     = -1             KT1     = -0.2942
+KT1L    = 1.68E-9        KT2     = 0              UA1     = 4.5E-9
+UB1     = -6.3E-18       UC1     = -1E-10         AT      = 1E3
+WL      = 0              WLN     = 1              WW      = 0
+WWN     = 1              WWL     = 0              LL      = 0
+LLN     = 1              LW      = 0              LWN     = 1
+LWL     = 0              CAPMOD  = 2              XPART   = 0.5
+CGDO    = 2.64E-10       CGSO    = 2.64E-10       CGBO    = 1E-9
+CJ      = 7.235521E-4    PB      = 0.9527404      MJ      = 0.4955303
+CJSW    = 2.692736E-10   PBSW    = 0.99           MJSW    = 0.295843
+CJSWG   = 6.4E-11        PBSWG   = 0.99           MJSWG   = 0.295843
+CF      = 0              PVTH0   = 5.98016E-3     PRDSW   = 14.8598424
+PK2     = 3.73981E-3     WKETA   = 3.730632E-3    LKETA   = -4.016397E-3
+AF      = 1              KF      = 0)
*
```

AMI_T22Y_SS (SLOW SLOW)

```
* Tech: AMI_C5N
* LOT: T22Y_SS (slow-slow)                WAF: 3102
* Temperature_parameters=Optimized
.MODEL ami06N NMOS (                          LEVEL   = 11
+VERSION = 3.1          TNOM    = 27          TOX     = 1.39E-8
+XJ      = 1.5E-7       NCH     = 1.7E17      VTH0    = 0.7087481
+K1      = 0.9382905    K2      = -0.1120562  K3      = 23.0789213
+K3B     = -7.3398981   W0      = 1E-8        NLX     = 1E-9
+DVT0W   = 0            DVT1W   = 0           DVT2W   = 0
+DVT0    = 3.3388333    DVT1    = 0.4283914   DVT2    = -0.0952143
+U0      = 459.674806   UA      = 1E-13       UB      = 1.503507E-18
+UC      = 1.325863E-11 VSAT    = 1.682969E5  A0      = 0.4784067
+AGS     = 0.0995613    B0      = 2.644452E-6 B1      = 5E-6
+KETA    = -5.808373E-3 A1      = 1.027068E-4 A2      = 0.3400289
+RDSW    = 1.329687E3   PRWG    = 0.0432392   PRWB    = 0.0149808
+WR      = 1            WINT    = 2.420178E-7 LINT    = 3.239617E-8
+XL      = 0            XW      = 0           DWG     = -1.396728E-8
+DWB     = 5.6316E-8    VOFF    = -2.57933E-3 NFACTOR = 0.8759425
+CIT     = 0            CDSC    = 2.4E-4      CDSCD   = 0
+CDSCB   = 0            ETA0    = 0.0152264   ETAB    = -1.058244E-3
+DSUB    = 0.2005917    PCLM    = 2.6613926   PDIBLC1 = -0.7606454
+PDIBLC2 = 2.593415E-3  PDIBLCB = -0.0326937  DROUT   = 0.6688818
+PSCBE1  = 5.85807E8    PSCBE2  = 7.988657E-5 PVAG    = 0
+DELTA   = 0.01         RSH     = 81.9        MOBMOD  = 1
+PRT     = 8.621        UTE     = -1          KT1     = -0.2501
+KT1L    = -2.58E-9     KT2     = 0           UA1     = 5.4E-10
+UB1     = -4.8E-19     UC1     = -7.5E-11    AT      = 1E5
+WL      = 0            WLN     = 1           WW      = 0
+WWN     = 1            WWL     = 0           LL      = 0
+LLN     = 1            LW      = 0           LWN     = 1
+LWL     = 0            CAPMOD  = 2           XPART   = 0.5
+CGDO    = 2.02E-10     CGSO    = 2.02E-10    CGBO    = 1E-9
+CJ      = 4.198358E-4  PB      = 0.99        MJ      = 0.4516115
+CJSW    = 3.241716E-10 PBSW    = 0.1000811   MJSW    = 0.1152935
+CJSWG   = 1.64E-10     PBSWG   = 0.1000811   MJSWG   = 0.1152935
+CF      = 0            PVTH0   = 0.0681426   PRDSW   = 188.2442761
+PK2     = -0.0295712   WKETA   = -0.0264969  LKETA   = -2.950307E-5
+AF      = 1            KF      = 0)
*
.MODEL ami06P PMOS (                          LEVEL   = 11
+VERSION = 3.1          TNOM    = 27          TOX     = 1.39E-8
+XJ      = 1.5E-7       NCH     = 1.7E17      VTH0    = -0.9223355
+K1      = 0.5769702    K2      = 9.039555E-3 K3      = 6.34861
+K3B     = -0.6383676   W0      = 1E-8        NLX     = 4.747861E-8
+DVT0W   = 0            DVT1W   = 0           DVT2W   = 0
+DVT0    = 2.4578035    DVT1    = 0.576459    DVT2    = -0.1206691
+U0      = 211.8308394  UA      = 2.824327E-9 UB      = 1E-21
+UC      = -5.66493E-11 VSAT    = 1.622935E5  A0      = 0.8712138
+AGS     = 0.1383793    B0      = 7.726776E-7 B1      = 5E-6
+KETA    = -5.205201E-3 A1      = 2.378013E-5 A2      = 0.3
```

```
+RDSW    = 3E3          PRWG    = -0.0454944     PRWB    = -2.13823E-4
+WR      = 1            WINT    = 2.849786E-7    LINT    = 5.529217E-8
+XL      = 0            XW      = 0              DWG     = -1.840088E-8
+DWB     = 2.185555E-8    VOFF    = -0.0684347     NFACTOR = 0.9119466
+CIT     = 0            CDSC    = 2.4E-4         CDSCD   = 0
+CDSCB   = 0            ETA0    = 0.3751245      ETAB    = -0.0827039
+DSUB    = 1            PCLM    = 2.2966371      PDIBLC1 = 0.0365228
+PDIBLC2 = 3.733251E-3    PDIBLCB = -0.0621219     DROUT   = 0.2123397
+PSCBE1  = 7.499863E9     PSCBE2  = 7.328296E-10   PVAG    = 4.584372E-6
+DELTA   = 0.01           RSH     = 101.9          MOBMOD  = 1
+PRT     = 59.494         UTE     = -1             KT1     = -0.2942
+KT1L    = 1.68E-9        KT2     = 0              UA1     = 4.5E-9
+UB1     = -6.3E-18       UC1     = -1E-10         AT      = 1E3
+WL      = 0            WLN     = 1              WW      = 0
+WWN     = 1            WWL     = 0              LL      = 0
+LLN     = 1            LW      = 0              LWN     = 1
+LWL     = 0            CAPMOD  = 2              XPART   = 0.5
+CGDO    = 2.84E-10       CGSO    = 2.84E-10       CGBO    = 1E-9
+CJ      = 7.235521E-4    PB      = 0.9527404      MJ      = 0.4955303
+CJSW    = 2.692736E-10   PBSW    = 0.99           MJSW    = 0.295843
+CJSWG   = 6.4E-11        PBSWG   = 0.99           MJSWG   = 0.295843
+CF      = 0            PVTH0   = 5.98016E-3     PRDSW   = 14.8598424
+PK2     = 3.73981E-3     WKETA   = 4.75772E-3     LKETA   = -6.715425E-3
+AF      = 1            KF      = 0)
*
```

APPENDIX B

DETAILED DIAGRAM FOR QFN 28 PACKAGE

REVISIONS			
ECN NO.	DATE	DESCRIPTION	APPROVED
10493	10/27/05	PRODUCTION RELEASE	D.BENANDO

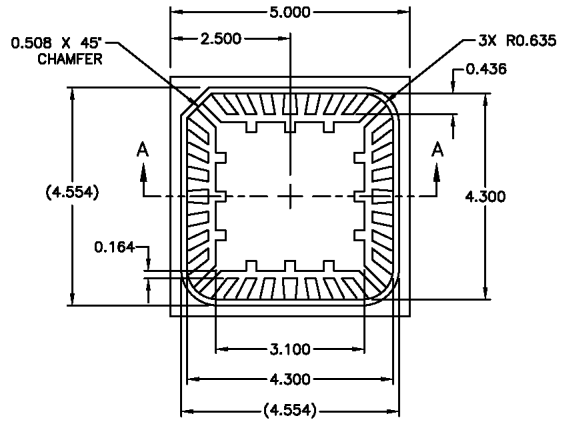

TOP VIEW

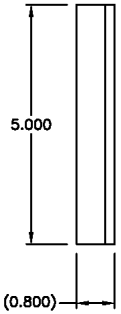

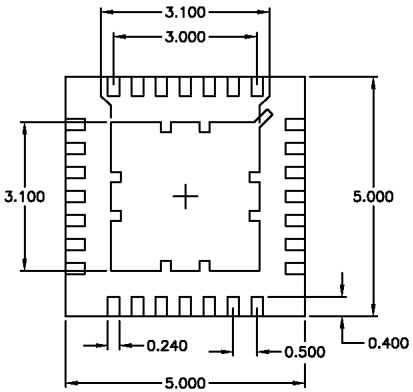

BOTTOM VIEW

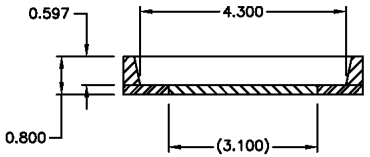

SECTION A–A

NOTES:
1. BODY: PLASTIC, SEMICONDUCTOR GRADE.
2. LEAD FRAME: COPPER, 194 FH.
3. LEAD FINISH: FULL GOLD PLATE.
4. FRAME THICKNESS: 0.2030 ±.0076.
5. DIE PAD: 3.100 X 3.100.
6. JEDEC OUTLINE: MO–220 (VHHD–3).

THIRD ANGLE PROJECTION

UNLESS OTHERWISE SPECIFIED DIMENSIONS ARE IN MILLIMETERS
TOLERANCES ARE:
X.XX ± 0.15 X.XXXX ± ---
X.XXX ± 0.050 ANGLES: ± 1°

DO NOT SCALE DRAWING

DRAWN BY W. GRIFFITTS DATE 07/28/05
APP BY P. FLASKERUD DATE 07/28/05
CUSTOMER ---

SEMPAC, INC.
Open-Pak™ Technologies
www.sempac.com
558 E. WEDDELL DRIVE, SUITE 5
SUNNYVALE, CALIFORNIA 94089
PHONE: (408) 400-9002 FAX: (408) 400-9006

28 Lead 5.00mm x 5.00mm
MLP Open–Pak

SIZE A | PART NO. MLP5X5–28–OP–01 | REV 1
SCALE NONE | CAD FILE MLP5X5–28–OP–01–R1.DWG | SHEET 1 OF 1

BORDER–ANM–1.DWG
REV 1 ECN 10386

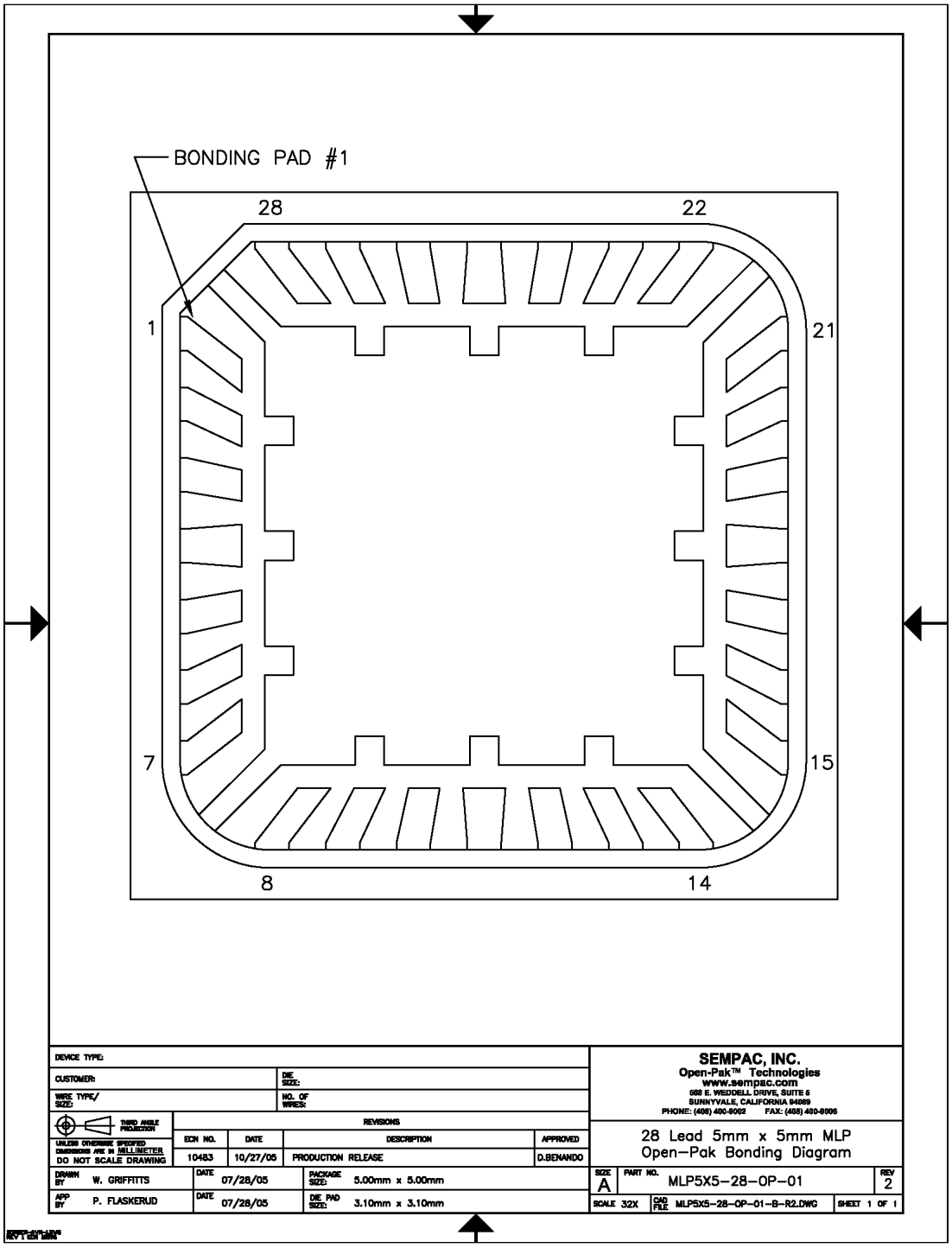
BONDING PAD #1
28
22
1
21
7
15
8
14
DEVICE TYPE:
CUSTOMER:
DIE SIZE:
WIRE TYPE/ SIZE:
NO. OF WIRES:
THIRD ANGLE PROJECTION
UNLESS OTHERWISE SPECIFIED DIMENSIONS ARE IN MILLIMETER
DO NOT SCALE DRAWING
REVISIONS
ECN NO. | DATE | DESCRIPTION | APPROVED
10483 | 10/27/05 | PRODUCTION RELEASE | D.BENANDO
DRAWN BY W. GRIFFITTS | DATE 07/28/05 | PACKAGE SIZE: 5.00mm x 5.00mm
APP BY P. FLASKERUD | DATE 07/28/05 | DIE PAD SIZE: 3.10mm x 3.10mm
SEMPAC, INC.
Open-Pak™ Technologies
WWW.SEMPAC.COM
559 E. WEDDELL DRIVE, SUITE 5
SUNNYVALE, CALIFORNIA 94089
PHONE: (408) 400-9002 FAX: (408) 400-9005
28 Lead 5mm x 5mm MLP
Open-Pak Bonding Diagram
SIZE A | PART NO. MLP5X5-28-OP-01 | REV 2
SCALE 32X | CAD FILE MLP5X5-28-OP-01-B-R2.DWG | SHEET 1 OF 1

APPENDIX C

MATLAB CODES FOR WIRELESS POWER TRANSFER

SIMULATED POWER EFFICIENCY BY RL SWEEP FROM 500Ω TO 1500Ω

```
clear
R2=4;
L2=11.03e-6;
C2=1356e-12;
mu=pi*4e-7*64;
w=2*pi*1.3e6;
Xc2=1/(w*C2);
X2=w*L2;

i=1;
j=1;
k=1;

for RL=500:100:1500
R1=8.7;
L1=60.95e-6;
C1=218e-12;
M=.548e-6;
Xm=w*M;
A1=RL/(RL^2*w^2*C2^2+1);
B1=R1/Xm^2;
B2=RL^2*w*C2/(RL^2*w^2*C2^2+1);
effi=A1/[B1*((R2+A1)^2+(w*L2-B2)^2)+R2+A1];
p(i)=effi*0.9*100;
i=i+1;
end

for RL=500:100:1500
R1=13.2;
L1=86.11e-6;
C1=149e-12;
M=.6568e-6;
Xm=w*M;
A1=RL/(RL^2*w^2*C2^2+1);
B1=R1/Xm^2;
B2=RL^2*w*C2/(RL^2*w^2*C2^2+1);
effi=A1/[B1*((R2+A1)^2+(w*L2-B2)^2)+R2+A1];
q(j)=effi*0.9*100;
j=j+1;
end

for RL=500:100:1500
R1=22.3;
L1=112.38-6;
C1=108e-12;
M=.833e-6;
Xm=w*M;
A1=RL/(RL^2*w^2*C2^2+1);
```

```
B1=R1/Xm^2;
B2=RL^2*w*C2/(RL^2*w^2*C2^2+1);
effi=A1/[B1*((R2+A1)^2+(w*L2-B2)^2)+R2+A1];
r(k)=effi*0.9*100;
k=k+1;
end

RL=[500:100:1500];
plot(RL, p,'b')
hold on
plot(RL, q,'r')
hold on
plot(RL, r,'c')
legend('r = 4cm', 'r = 5cm','r = 6cm')

todos=[p' q' r'];
```

REFERENCES

[1] Andrew D. DeHennisand Kensall D. Wise, "A Wireless Microsystem for the Remote Sensing of Pressure, Temperature, and Relative Humidity," *Journal of Microelectromechanical Systems*, vol. 14, no. 1, Feb., 2005.

[2] Lun-Chen Hsu, "Physiological Telemetric Sensing Systems for Medical Applications," *University of Texas at Arlington*, Dec., 2009.

[3] M. H. Mickle, Minhong Mi, L. Mats, C. Capelli, and H. Swift, "Powering Autonomous Cubic-Millimeter Devices," *, IEEE Antennas and Propagation Magazine*, ISBN 1045-9243, vol. 48, no. 1, pp. 11-21, 2006.

[4] J. L. Gonzalez-Guillaumin, D. C. Sadowski, K. V. I. S. Kaler, and M. P. Mintchev, "Ingestible Capsule for Impedance and pH Monitoring in the Esophagus," *, IEEE Transactions on Biomedical Engineering*, ISBN 0018-9294, vol. 54, no. 12, pp. 2231-6, 2007.

[5] S. Shay, R. Tutuian, D. Sifrim, M. Vela, J. Wise, N. Balaji, X. Zhang, T. Adhami, J. Murray, J. Peters, and D. Castell, "Twenty-Four Hour Ambulatory Simultaneous Impedance and pH Monitoring: A Multicenter Report of Normal Values from 60 Healthy Volunteers " , United States, ISBN 0002-9270; 0002-9270, vol. 99, no. 6, pp. 1037-43, Jun, 2004.

[6] M. Deterre, B. Boutaud, R. Dalmolin, S. Boisseau, J. -J Chaillout, E. Lefeuvre, and E. Dufour-Gergam, "Energy Harvesting System for Cardiac Implant Applications," pp. 387-91, 2011.

[7] W. Turner, Chun-Ming Tang, B. Beck, T. H. Mareci, and R. Bashirullah, "Nuclear Magnetic Resonance Energy Harvesting for Ultra-Low Power Biomedical Implants," *IEEE 12th Anuual Wireless and Microwave Technology Conference (WAMICON)*, pp. 1-4, 2011.

[8] E. O. Torres and G. A. Rincon-Mora, "A 0.7- m BiCMOS Electrostatic Energy-Harvesting System IC," *IEEE Journal of Solid-State Circuits*, ISBN 0018-9200, vol. 45, no. 2, pp. 483-96, 2010.

[9] Y. K. Tan, K. Y. Hoe, and S. K. Panda, "Energy Harvesting using Piezoelectric Igniter for Self-Powered Radio Frequency (RF) Wireless Sensors," *IEEE International Conference on Industrial Technology (ICIT)*, pp. 1711-6, 2006.

[10] P. Scholz, C. Reinhold, W. John, and U. Hilleringmann, "Analysis of Energy Transmission for Inductive Coupled RFID Tags," *IEEE International Conference on RFID*, pp. 183-190, 2007.

[11] Qiuting Huangand M. Oberle, "A 0.5mW Passive Telemetry IC for Biomedical Applications," *ESSCIRC '97. Proceedings of the 23rd European Solid-State Circuits Conference*, pp. 172-175, 1997.

[12] IEEE Standard, "IEEE Standard for Safety Levels with Respect to Human Exposure to Radio Frequency Electromagnetic Fields, 2 kHz to 300 GHz," *, IEEE Std C95.1-2005*, 2006.

[13] Catherine Dehollain, Michel De Clercq, and Norbert Joehl, "Design and Optimization of Passive UHF RFID Systems," *Springer Verlag*, ISBN 0387352740, 2006.

[14] WebMD, "WebMD Heartburn Health Center - Find GERD, Acid Reflux, and Heartburn Information," <http://www.webmd.com/heartburn-gerd>.

[15] Peter J. Kahriasand John E. Pandolifino, "The Epidemiology and Pathophysiology of Gastroesophageal Refulx Disease," *Managing Failed Anti-Reflux Therapy*, pp. 1-14, 2006.

[16] Kenneth R. DeVault and Donald O. Castell, "Updated Guideline for the Diagnosis and Treatment of Gastroesophageal Reflux Disease," *American Journal of Gastroenterology*, vol. 100, pp. 190-200, 2005.

[17] D. Sifrim, R. Holloway, J. Silny, Z. Xin, J. Tack, A. Lerut, and J. Janssens, "Acid, Nonacid, and Gas Reflux in Patients with Gastroesophageal Reflux Disease during Ambulatory 24-Hour pH-Impedance Recordings, " United States, ISBN 0016-5085; 0016-5085, vol. 120, no. 7, pp. 1588-98, Jun, 2001.

[18] I. Mainie, R. Tutuian, S. Shay, M. Vela, X. Zhang, D. Sifrim, and D. O. Castell, "Acid and Non-Acid Reflux in Patients with Persistent Symptoms Despite Acid Suppressive Therapy: A Multicentre Study using Combined Ambulatory Impedance-pH Monitoring, " England, ISBN 1468-3288; 0017-5749, vol. 55, no. 10, pp. 1398-402, Oct, 2006.

[19] Thermpon Ativanichayaphong, Shou Jiang Tang, Jianqun Wang, Wen-Ding Huang, Harry F. Tibbals, Stuart J. Spechler, and J. -C Chiao, "An Implantable, Wireless and Batteryless Impedance Sensor Capsule for Detecting Acidic and Non-Acidic Reflux," *Gastroenterology*, vol. 134, no. 4, pp. A-63, 2008.

[20] Lun-Chen Hsu, Wen-Ding Huang, Hung Cao, Sanchali Deb, and J. -C Chiao, "Integrated Dual Sensors in a Batteryless Wireless Capsule," *BMES Biomedical Engineering Society Annual Fall Scientific Meeting*, Oct., 2009.

[21] MOSIS, , www.mosis.com

[22] T. Ativanichayaphong, J. Wang, W. Huang, S. Rao, and J. -C Chiao, "A Simple Wireless Batteryless Sensing Platform for Resistive and Capacitive Sensors," *IEEE Sensors*, ISBN 1930-0395, pp. 139-42, 2007.

[23] Thermpon Ativanichayaphong, "Wireless Devices for Medical Applications," *University of Texas at Arlington*, Ph.D., 2007.

[24] Wen-Ding Huang, Jianqun Wang, Thermpon Ativanichayaphong, Lun-Chen Hsu, Sanchali Deb, Mu Chiao, and J. -C Chiao, "Investigation of Repeatability of Sol-Gel Iridium Oxide pH Sensor on Flexible Substrate," *Smart Materials, Nano+Micro-Smart Systems Symposium, Micro- and Nanotechnology: Materials, Processes, Packaging, and Systems Conference*, vol. 7269, Dec., 2008.

[25] Shiho Kim, Jung-Hyun Cho, and Suk-Kyung Hong, "A Fullwave Voltage Multiplier for RFID Transponders," *IEICE Trans. Commun.*, vol. E91-B, Jan., 2008.

[26] Fan Jiang, Donghui Guo, and L. L. Cheng, "Analysis and Design of Power Generator on Passive RFID Transponders," *Progress In Electromagnetics Research Symposium*, Hangzhou, China, Mar., 2008.

[27] Stephen O'Driscoll, Ada S. Y. Poon, and Teresa H. Meng, "A mm-Sized Implantable Power Receiver with Adaptive Link Compensation," *Session 17.5 of IEEE ISSCC*, pp. 294-296, Feb, 2009.

[28] Alexaner Vaz, Ariz Ubarretxena, Daniel Pardo, Inaki Sancho, and Roc Berenguer, "Design Methodology of a Voltage Multiplier for Full Passive Long Range UHF RFID," *3rd European Workshop on RFID Systems and Technologies*, Jun., 2007.

[29] Giuseppe De Vitaand Giuseppe Iannaccone, "Design Criteria for the RF Section of UHF and Microwave Passive RFID Transponders," *IEEE Transactions on Microwave Theory and Techniques*, vol. 53, no. 9, Sep., 2005.

[30] Fatih Kocerand Michael P. Flynn, "A New Transponder Architecture with on-Chip ADC for Long-Range Telemetry Application," *IEEE Journal of Solid-State Circuits*, vol. 41, no. 5, May, 2006.

[31] Kenneth Kuhn A, "Diode Applications," Sep., 2008, <http://www.kennethkuhn.com/students/ee351/text>.

[32] Changming Ma, Chun Zhang, and Zhihua Wang, "A Low-Power AC/DC Rectifier for Passive UHF RFID Transponders," *IEEE International Symposium on Microwave, Antenna, Propagation, and EMC Technologies for Wireless Communications*, 2007.

[33] Yuan Yao, Yin Shi, and Foster F. Dai, "A Novel Low-Power Input-Independent MOS AC/DC Charge Pump," *IEEE International Symposium on Circuits and Systems*, vol. 1, pp. 380-383, May, 2005.

[34] Alanson P. Sample, Daniel J. Yeager, Pauline S. Powledge, and Joshua R. Smith, "Design of a Aassively-Powered, Programmable Sensing Platform for UHF RFID Systems," *IEEE International Conference on RFID*, 2007.

[35] Yao-Huang Kao, Chia-Chuan Liu, and Hung-Chang Kuo, "Study of Front End of CMOS RFID Tag with Inductively-Coupled Broadband Antenna," *Chung Hua Journal of Science and Engineering*, vol. 5, no. 4, pp. 15-19, 2007.

[36] Chih-Wen Chuang, E. Go Chua, Yu-Sheng Lai, and Wai-Chi Fang, "RF-Powered Li-Ion Battery Charger for Biomedical Applications," *LiSSA 2009. IEEE/NIH Life Science Systems and Applications Workshop*, pp. 187-9, 2009.

[37] Kin Keung Lee, M. Z. Dooghabadi, H. A. Hjortland, O. Næss, and T. S. Lande, "A 5.2 pJ/pulse Impulse Radio Pulse Generator in 90 Nm CMOS," *IEEE International Symposium on Circuits and Systems (ISCAS),* ISBN 0271-4302, pp. 1299-302, 2011.

[38] Y. -Y Lin, D. J. Gundlach, S. F. Nelson, and T. N. Jackson, "Stacked Pentacene Layer Organic Thin-Film Transistors with Improved Characteristics," *IEEE Electron Device Letters*, ISBN 0741-3106, vol. 18, no. 12, pp. 606-8, 1997.

[39] F. Kocer, P. M. Walsh, and M. P. Flynn, "An RF Powered, Wireless Temperature Sensor in Quarter Micron CMOS," *ISCAS '04. Proceedings of the 2004 International Symposium on Circuits and Systems*, vol. 4, pp. IV,876-9 Vol.4, 2004.

[40] Xi-Ning Wang, Li-Wu Yang, Ting-Huang Lee, Jian-Kun Su, Bin Zhu, and Xiao-Fang Yao, "RF Modeling of Integrated RF CMOS Schottky Diodes for Rectifier Designs," *ICSICT. 9th International Conference on Solid-State and Integrated-Circuit Technology*, pp. 305-8, 2008.

[41] U. Karthaus and M. Fischer, "Fully Integrated Passive UHF RFID Transponder IC with 16.7-μW Minimum RF Input Power," *IEEE Journal of Solid-State Circuits*, ISBN 0018-9200, vol. 38, no. 10, pp. 1602-8, 2003.

[42] Curtis Wayne Cahoon, "Low_Voltage CMOS Temperature Sensor Design using Schottky Diode-Based References," *Boise State University*, Jun., 2008.

[43] Bo Hu and C. -J R. Shi, "Simulation of Closely Related Dynamic Nonlinear Systems with Application to Process–Voltage–Temperature Corner Analysis," *, IEEE Transactions on Computer-Aided Design of Integrated Circuits and Systems*, ISBN 0278-0070, vol. 27, no. 5, pp. 883-92, 2008.

[44] S. Onaissi and F. N. Najm, "A Linear-Time Approach for Static Timing Analysis Covering all Process Corners," *, IEEE Transactions on Computer-Aided Design of Integrated Circuits and Systems*, ISBN 0278-0070, vol. 27, no. 7, pp. 1291-304, 2008.

[45] S. Natarajan, M. A. Breuer, and S. K. Gupta, "Process Variations and their Impact on Circuit Operation," *IEEE International Symposium*, pp. 73-81, 1998.

[46] A. Aryanpourand G. E. R. Cowan, "A Circuit Design and Fabrication Approach to Address Global Process Variation," *Circuits and Systems, 2009. MWSCAS '09. 52nd IEEE International Midwest Symposium*, ISBN 1548-3746, pp. 455-458, 2009.

[47] R. W. Dutton, D. A. Divekar, A. G. Gonzalez, S. E. Hansen, and D. A. Antoniadis, "Correlation of Fabrication Process and Electrical Device Parameter Variations," *, IEEE Journal of Solid-State Circuits*, ISBN 0018-9200, vol. 12, no. 4, pp. 349-355, 1977.

[48] Napong Panitantum, Aperadee Yordthein, Watcharakon Noothong, Apisak Worapishet, and Manop Thamsirianunt, "A CMOS RFID Transponder," *ISCIT*, Pattaya, Thailand, Oct., 2002.

[49] Mi and Minhong, "RFID Radio Circuit Design in CMOS," *, Ansoft Corp.*, 2011, <http://uqu.edu.sa/files2/tiny_mce/plugins/filemanager/files/4220086/RFID%20Radio%20Circuit%20Design%20in%20CMOS.pdf>.

[50] R. Jacob Baker, "CMOS Circuit Design, Layout, and Simulation," *Wiley-IEEE*, Revised Second Edition, ISBN 978-0-470-22941-5, pp. 564-565, 2008.

[51] Uming Ko and P. T. Balsara, "High-Performance Energy-Efficient D-Flip-Flop Circuits," *, IEEE Transactions on Very Large Scale Integration (VLSI) Systems,* ISBN 1063-8210, vol. 8, no. 1, pp. 94-8, 2000.

[52] D. Markovic, B. Nikolic, and R. W. Brodersen, "Analysis and Design of Low-Energy Flip-Flops," *International Symposium on Low Power Electronics and Design*, pp. 52-5, 2001.

[53] Baker RJ. CMOS circuit design, layout, and simulation: Wiley-IEEE, 2008.

[54] Neil Weste DH. CMOS VLSI Design: A Circuits and Systems Perspective : Addison-Wesley, 2011.

[55] N. Ohkubo, M. Suzuki, T. Shinbo, T. Yamanaka, A. Shimizu, K. Sasaki, and Y. Nakagome, "A 4.4 Ns CMOS 54×54-b Multiplier using Pass-Transistor Multiplexer," *, IEEE Journal of Solid-State Circuits*, ISBN 0018-9200, vol. 30, no. 3, pp. 251, 1995.

[56] B. G. Song, O. J. Kwon, I. K. Chang, H. J. Song, and K. D. Kwack, "A 1.8 V Self-Biased Complementary Folded Cascode Amplifier," *IEEE Asia Pacific Conference on ASICs*, ISBN 0-7803-5705-1, pp. 63-65, 1999, <http://dx.doi.org/10.1109/apasic.1999.824030>.

[57] R. Jacob Baker, "CMOS Circuit Design, Layout, and Simulation," *Wiley-IEEE*, Revised Second Edition, ISBN 978-0-470-22941-5, pp. 733-737, 2008.

[58] R. Jacob Baker, "CMOS Circuit Design, Layout, and Simulation," *Wiley-IEEE*, Revised Second Edition, ISBN 978-0-470-22941-5, pp. 570-571, 2008.

[59] R. Want, "An Introduction to RFID Technology," *, IEEE Pervasive Computing*, ISBN 1536-1268, vol. 5, no. 1, pp. 25-33, 2006.

[60] Yunlei Liand Jin Liu, "A 13.56 MHz RFID Transponder Front-End with Merged Load Modulation and Voltage Doubler-Clamping Rectifier Circuits," *IEEE International Symposium on Circuits and Systems. ISCAS*, pp. 5095-5098 Vol. 5, 2005.

[61] Brunvand E., "Digital VLSI Chip Design with Cadence and Synopsys CAD Tools," Addison-Wesley, 2010.

[62] MOSIS, "Packaging," , www.mosis.com

[63] Sempac, "QFN28," , www.sempac.com

[64] Waveshare Electronics, "GP-QFN28-0.5," http://www.wvshare.com/product/GP-QFN28-0.5.htm

[65] Maysam Ghovanloo and Suresh Atluri, "A Wide-Band Power-Efficient Inductive Wireless Link for Implantable Microelectronic Devices using Multiple Carriers," ISBN 1057-7122, vol. 54, no. 10, pp. 2211-2221, 2007, <http://dx.doi.org/10.1109/tcsi.2007.905187>.

[66] Yong-Xin Guo, Duan Zhu, and R. Jegadeesan, "Inductive Wireless Power Transmission for Implantable Devices," pp. 445-8, 2011.

[67] Michael W. Baker and Rahul Sarpeshkar, "Feedback Analysis and Design of RF Power Links for Low-Power Bionic Systems," ISBN 1932-4545, vol. 1, no. 1, pp. 28-38, 2007, <http://dx.doi.org/10.1109/tbcas.2007.893180>.

[68] K. M. Silay, C. Dehollain, and M. Declercq, "Improvement of Power Efficiency of Inductive Links for Implantable Devices," pp. 229-32, 2008.

[69] S. Deb, SJ Tang, TL Abell, S. Rao, WD Huang, SD TO, C. Lahr, and JC Chiao, "An Endoscopic Wireless Gastrostimulator (with Video)," *Gastrointestinal Endoscopy*, http://www.ncbi.nlm.nih.gov/pubmed/22248609, vol. 2012, no. 3/14/2012, 2012.

[70] Young-Sik Seo, Minh Quoc Nguyen, Zachariah Hughes, Smitha Rao, and J. -C Chiao, "Wireless Power Transfer by Inductive Coupling for Implantable Batteryless Stimulators," *IEEE International Microwave Symposium*, Montreal, Canada Edition, June, accepted 2012.

[71] S. Hackl, C. Lanschutzer, P. Raggam, and W. L. Randeu, "A Novel Method for Determining the Mutual Inductance for 13.56MHz RFID Systems," pp. 297-300, 2008.

[72] S. Deb and et. al., "Miniature Wireless Gastro-Stimulators for Gastric Mobility," *Medical Engineering & Physics*, 2012, in review.

[73] Hung Cao, Shreyas K. Thakar, Timothy Fu, Manthan Sheth, Matthew L. Oseng, Vaibhav Landge, Young-sik Seo, and J. -C Chiao, "A Wireless Strain Sensor System for Bladder Volume Monitoring," *International Microwave Symposium (IEEE)*, Baltimore, 2011.

[74] Seo, Cao Y.-S., Thakar H. , Oseng S.K. , Sheth M.L. , Nguyen M.D. , Chiao C.M , and J-C., "A Wireless Platform for Wound Condition Monitoring," *Annual Meeting of Biomedical Engineering Society*, Austin, TX, 2010.

[75] http://www.aao.org/newsroom/upload/Eye-Health-Statistics-April-2011.pdf

[76] http://www.mayoclinic.com/health/cataracts/DS00050/DSECTION=treatments-and-drugs

[77] http://www.improveyourvision.com/cataract-center/monofocal-vs-multifocal-implants.html

BIOGRAPHICAL INFORMATION

Young-Sik Seo received the B.S. and M.S. degrees in electrical engineering from the University of Texas at Arlington, Arlington, TX, in 2003 and 2005, respectively. His main interests are analog circuit design & analysis, integrated circuit design & layout, and energy harvesting & RF communications. His research topic is “An IC Design for Wireless Batteryless Multi-Sensing Platform for Biomedical Applications”. He has been a Ph.D. instructor for number of undergraduate courses including Introduction to Electrical Engineering and Circuit Analysis in electrical engineering at the University of Texas at Arlington. He is the winner of Graduate Dean’s Award of 2012 Annual Celebration of Excellence in Students (ACES) in the same school. The winning title was “A Design of Integrated Circuit for Batteryless Wireless Platform for Biomedical Applications”.